POLITECNICO DI MILANO

Scuola di Ingegneria Industriale e dell'Informazione

Corso di Laurea Magistrale in Ingegneria Elettrica

The Research of Valve Reactor's Controllable Technology and Large DC Current Detection Based on Magnetic Saturation

Relatore: Prof. Sergio.Pignari

Prof. Flavia.Grassi

Tesi di Laurea Magistrale di:

SHUAI CHENG
Matr. 854617

Anno Accademico 2018-2019

INDICE DELLE FIGURE

INDICE DELLE TABELLE

ABSTRACT

Come caratteristica dei materiali magnetici, la tecnologia di saturazione magnetica può offrire prestazioni eccellenti in molte applicazioni ingegneristiche. Quando il nucleo è insaturo, la permeabilità del materiale non è generalmente un valore costante, la curva di magnetizzazione presenta una grande non-linearità, la magnetizzazione e la smagnetizzazione sono caratterizzate dal ciclo di isteresi. Ma dopo la saturazione magnetica, le differenze di isteresi non sono evidenti e la permeabilità magnetica è vicina alla permeabilità all'aria, mentre si raggiunge à un'eccellente linearità. Queste caratteristiche sono spesso utilizzate nelle apparecchiature elettriche basate sulla saturazione magnetica.

This thesis first briefly introduced the main basic application of magnetic saturation technology - the development of valve reactors and the research status of large DC current detection solutions. Several models commonly used to describe magnetic saturation and their advantages and disadvantages were analyzed, and then proposes an improved structure of valve reactor and a novel sensor for large DC current detection. This thesis analyzed the problems existing in converter valve reactors, and proposes a control technology for valve reactors based on magnetic saturation. By controlling the saturation of the reactor core, the hysteresis loss and the magnetostrictive is reduced, thus the reactor noise, vibration and over-heating are supressed. Based on the Jiles-Atherton model of magnetic saturation, the valve reactor improvement scheme is demonstrated in principle, simulation and experiment. By designing the prototype experiment and measuring the practical work B-H curve of the core, the feasibility of the technology was verified. In addition, based on the magnetic saturation characteristics, this paper also proposed a new self-oscillating fluxgate scheme and deduced its linear relationship in detail. Through experimental verification, this scheme can be used for low-cost and high-precision detection of large DC currents. For large DC current measurement, the current sensor prototype is also developed based on the new scheme. The sensitivity, linearity, measurement range, resolution, temperature characteristics and repeatability have been detailed discussed.

In this thesis, the working flux of converter valve reactor is limited to the saturation region, which achieves the goal of reducing noise, reducing vibration and heat and increasing the switching speed from the source; A compact self-oscillating current sensor for large DC current measurement with a new feedback strategy is proposed. In this novel fluxgate transducer, the excitation, compensation and demodulation are realized by only one winding and one core. Compared with the published feedback approaches, this novel strategy has a more compact structure and can suppress the modulation ripples without additional signal conditioning circuit. The experimental results show that the new sensor achieves 0.5% linearity, mA resolution, and 125 ppm / °C drift within the ±50 A and ±100 A measurement ranges. Although the performance of the proposed sensor is inferior to the latest high-performance products on the market, however, it has reached an advanced level with

only one core and one winding configuration.

KEY WORDS: Magnetic saturation; Valve reactor; Self-oscillating fluxgate; Large DC current detection

ASTRATTO

La saturazione magnetica è una caratteristica dei materiali magnetici e la tecnologia di saturazione magnetica può offrire prestazioni eccellenti in molte applicazioni di ingegneria. Quando il nucleo è insaturo, la permeabilità del materiale non è generalmente un valore costante, la curva di magnetizzazione presenta una grande non-linearità, la magnetizzazione e la smagnetizzazione sono caratterizzate dal ciclo di isteresi; Ma dopo la saturazione magnetica, le differenze di isteresi non sono evidenti e la permeabilità magnetica è vicina alla permeabilità all'aria, mentre si raggiunge à un'eccellente linearità. Queste caratteristiche sono spesso utilizzate nelle apparecchiature elettriche basate sulla saturazione magnetica.

Questa tesi ha brevemente introdotto la principale applicazione di base della tecnologia di saturazione magnetica - lo sviluppo di reattori a valvole e lo stato della ricerca di grandi soluzioni di rilevamento di corrente continua. Sono stati analizzati diversi modelli comunemente usati per descrivere la saturazione magnetica e i loro vantaggi e svantaggi, e quindi propone una struttura migliorata del reattore a valvole e un nuovo sensore per il rilevamento di grandi correnti CC. Questa tesi ha analizzato i problemi esistenti nei reattori delle valvole di conversione e propone una tecnologia di controllo per i reattori delle valvole basata sulla saturazione magnetica. Controllando la saturazione del nocciolo del reattore, la perdita di isteresi e la magnetostrittiva si riducono, quindi il rumore del reattore, la vibrazione e il surriscaldamento vengono soppressi. Basato sul modello di saturazione magnetica di Jiles-Atherton, lo schema di miglioramento del reattore della valvola è dimostrato in linea di principio, simulazione ed esperimento. Progettando l'esperimento prototipo e misurando il lavoro pratico curva B-H del nucleo, è stata verificata la fattibilità della tecnologia. Inoltre, sulla base delle caratteristiche di saturazione magnetica, questo documento propone anche un nuovo schema fluxgate auto-oscillante e deduce la sua relazione lineare in dettaglio. Attraverso la verifica sperimentale, questo schema può essere utilizzato per il rilevamento a basso costo e ad alta precisione di grandi correnti CC. Per la misura della corrente continua di grandi dimensioni, il prototipo del sensore corrente viene sviluppato anche in base al nuovo schema. La sensibilità, la linearità, la gamma di misurazione, la risoluzione, le caratteristiche della temperatura e la ripetibilità sono state discusse dettagliatamente.

In questo documento, il flusso di lavoro del reattore della valvola del convertitore è limitato alla regione di saturazione, che raggiunge l'obiettivo di ridurre il rumore, ridurre le vibrazioni e il calore e aumentare la velocità di commutazione dalla sorgente; Viene proposto un sensore di corrente auto-oscillante compatto per grandi misure di corrente continua con una nuova strategia di retroazione. In questo romanzo trasduttore fluxgate, l'eccitazione, compensazione e demodulazione sono realizzati da un solo avvolgimento e un nucleo. Rispetto agli approcci di feedback pubblicati, questa nuova strategia ha una struttura più compatta e può sopprimere le ondulazioni di modulazione senza un ulteriore circuito di condizionamento del segnale. I risultati sperimentali mostrano che il nuovo sensore raggiunge linearità dello 0,5%, risoluzione mA e deriva 125 ppm / ° C entro i range di misurazione ± 50 A e ± 100 A. Sebbene le prestazioni del sensore proposto siano inferiori ai più recenti prodotti ad alte prestazioni sul mercato, tuttavia, ha raggiunto un livello avanzato con una sola configurazione di nucleo e una di avvolgimento.

PAROLE CHIAVE: saturazione magnetica; Reattore della valvola; Fluxgate auto-oscillante; Rilevamento corrente CC di grandi dimensioni

INDICE

1 Introduction

1.1 Research Background of Magnetic Saturation

Magnetic saturation is a characteristic of magnetic materials. Before magnetic saturation is reached, the magnetic flux density *B* in the material increases as the applied magnetic field strength *H* increases. However, when the magnetic field strength *H* increases to a certain extent, the magnetic flux density *B* will only increase slowly with vacuum permeability, this phenomenon is considered as magnetic saturation[1]. Magnetic saturation will limit the maximum magnetic flux the core can reach. In high-power motors or power transformers, the large volume is usually owing to magnetic saturation's restriction to the magnetic flux. In addition, magnetic saturation can cause nonlinearity such as first harmonic distortion in linear circuits. In many cases, magnetic saturation are harmful. For instance, when the current exceeds the rated current of a power transformer, the magnetic core saturates and over-heating may jeoperdize the safety operation. Thus, air gaps is frequently added to the core to prevent saturation. In fact, the unique nonlinear characteristics of magnetic saturation can also be utilized, and can exhibit unique advantages. For example, compared with traditional reactive power compensation devices, the most widely used controllable reactor at present has lower loss, wider application, easy installation and other advantages[2].

Magnetically saturated electrical devices, such as magnetic saturation regulators and saturated controllable reactors, mostly utilize the magnetic saturation nonlinearity. When the magnetic saturation regulator is operating, as the applied power voltage increases, the magnetic flux in the core increases accordingly. When the magnetic flux in the secondary core reaches the saturation point, even if the power supply voltage increases again, the increased magnetic flux can only leak into the air, and the magnetic flux in the secondary core does not increase linearly any more, so the resulting output voltage of the secondary coil remains essentially unchanged at this time to achieve the voltage stabilizing; Controlled saturable reactor is original a kind of reactive power compensation device. The principle is to adjust the saturation depth to change the inductance value so as to adjust the reactive power. In addition, the most extensive application of magnetic saturation technology is fluxgate technology, which utilizes the deep saturation of soft magnetic materials to achieve high sensitivity detection of DC or low frequency magnetic fields and currents.

The converter valve is the core equipment of HVDC power grid, which functions as the facilities connecting the three-phase AC voltage to the DC terminal to obtain the desired DC voltage and realize the control of the power[3]. The core device of the converter valve is the power semiconductor components such as thyristors. The power semiconductor branch attenuates oscillations when the thyristor is turned on, limits the rate of current rise, and protects the system against overvoltage during lightning and steep wave surges through

cascading saturated valve reactors[4]. However, according to the prious data, with the large number of HVDC transmission projects being put into use, there have been many overheating and vibration accidents in the operation of valve reactors. Some of the highest temperatures even reached above 110℃. The valve reactors in abnormal operation not only lost the protection for thyristor, but also threaten the safe operation of the converter station as overheating can seriously burden the water cooling system due to overheating[5]. At present, research on the ferromagnetic saturation characteristics of valve saturable reactors is still rarely blank. Using magnetic saturation technology, through the rational use of the saturated depth range of valve reactor operation, the design of valve reactors can be further improved.

In addition, with the increase in the use of large DC currents, the demand for DC high-current measuring devices has also increased. For instance, with the increase of transmission current levels and transmission capacity in HVDC, the research on accurate measurement techniques for large DC currents has become gradually vital. Accurate measurement of transmission currents provides a reliable basis for calculating line losses and technical indicators for transmission. At the same time, by on-line detection of currents, the operating status of HVDC transmission systems can be surveillant in real time, abnormalities can be detected in time, thus the primary transmission lines and valuable sedondary devices can be protected. There are two main ways to measure the large DC current: one is to convert the current into a voltage through a resistor, the biggest difficulty is heat and power consumption; and the second is to measure the surrounding magnetic field created by large DC current, the most commonly used Hall sensor are somewhat inadequate on stability and thermal drift. The high sensitivity of fluxgate technology provides a promising solution for the accuracy DC current measurement.

Concerning the above background, this paper first studies the magnetic saturation model, and studies the application of magnetic saturation technology in valve reactor improvement and DC high current detection, respectively, in order to explore possible innovative applications of magnetic saturation technology. The research results of this paper have some conclusions about the magnetic saturation technology and have a certain significance for the improvement of magnetic saturation technology theory.

1.2 Research Status

The magnetic saturation phenomenon was initially studied as a harmful phenomenon. Saturation of transformers will cause sudden rising of the input current and burn the primary side. Saturation in the switching power supply can cause the transformer to overheat and breakdown, resulting in damage to the switching power supply. Thus, the initial study of the magnetic saturation mechanism was mainly to avoid magnetic saturation. With the rapid development of material technology, various high-performance soft magnetic materials have been successfully developed. The heat caused by magnetic saturation has been greatly reduced, and the magnetic saturation phenomenon has been re-emphasized. The magnetic

saturation technology has been gradually applied to various power industries. In particular, with the rise of amorphous and nanocrystalline materials with high magnetic permeability and low loss, even if the magnetic material goes in and out of saturation frequently, the coil will not be burned due to the overheating.

The study of magnetic saturation are based on the magnetization theory and the corresponding mathematical model that fully describe the magnetization. The model study of magnetization theory is divided into macroscopic and microscopic. At the macro level, the focus is on the study of macroscopic magnetization characteristics such as magnetic hysteresis curves and magnetic permeability based on macrophysical quantities such as magnetic field strength *H* and magnetic flux density *B*. Engineering applications exist mainly on power equipment with iron cores such as power transformers, etc[7]. The representative of the macroscopic magnetization theory is the Preisach model and various related improved models[8]. To a certain extent, the derivation and lack of a clear physical basis limit the application of the model[9]. For the anisotropy of magnetic media, the publications[10,11] proposed a vector magnetization model; in many practical applications, the magnetization of the material is performed in an alternating magnetic field, even if ferromagnetic material is isotropic, the magnetization process in the variable magnetic field also demonstrates a very difference from the static magnetic field, so the complex permeability is often defined in the high frequency field[12], and the commonly used complex permeability measurement method is summarized in publications[13,14]. Publications[15,16] proposed a comprehensive method of simulated fitting of the dynamic magnetic properties of transformer core materials and structural steels; the magnetization process model has a high degree of complexity, and sometimes for simplification, a simple piecewise linear model is often used, i.e. the hysteresis loops are neglected, the magnetization curve is segmented into linear parts according to the saturation and unsaturation, and the piecewise linear model is widely used in the field of electrical engineering[17].

The microscopic study of the magnetization theory is mainly focused on the magnetic domain scale. The magnetic domain theory provides a theoretical basis for the magnetization mechanism of magnetic materials [18]. Starting from the domain theory of Landau-Liftshitz, magnetic domains are considered to be the basic components of ferromagnetic materials[19]. The magnetic domain theory gives the hysteresis loopback a well explaination, and the magnetic saturation phenomenon is also explained as that the external magnetic field is strengthened to a certain degree and the magnetic moment directions of all magnetic domains are consistent, thus the magnetic flux density will nearly stop increase when saturated. The literature[20] summarizes the current commonly used methods for observation of more than 10 types of ferromagnetic domains. Based on the magnetic domain theory, there are several popular magnetization models,i.e. Globus model, S-W model and J-A model. Among them, the J-A model is mathematically convenient to describe and has clear physical concepts, thus, it is now a hot spot for the study of modeling and simulation of ferromagnetic materials[9]. On the microscopic scale, there are also researches deep into the

atomic state, such as the spins of atoms and electrons on the crystal lattice, and a series of computational engineering of quantum mechanics, those are more polular in the fields of physics and materials science.

Regarding the magnetization theory, no matter macroscopic or microcosmic, the current models commonly use various functions and their combination, matrix and other fitting methods to describe the magnetization curve of the core. Due to the simultaneous existence of problems such as hysteresis loop and saturation nonlinearity[21, 22], the mathematical expressions are generally complicated and obscure. The definition of magnetic saturation technology has not yet been unified at home and abroad. However, magnetic saturation has been widely used in engineering applications such as saturation reactors and fluxgate technologies.

In the aspects of magnetic saturation's applications, in the 1950s, Russia first applied the magnetic amplification theory to the power system and conducted deep researches on the saturated controlled reactors[23]. In 1955, the world's first controllable reactor was successfully manufactured in the United Kingdom. In power systems, controllable reactors can adjust the saturation depth of the cores to achieve voltage regulation and reactive power compensation. Compared with traditional reactive power compensators, they have the advantages of low cost and high reliability, and they can play an important role in the improvement in the stability and power supply quality of power systems. In China, the investment in magnetic saturation reactors is also considerable. China's self-developed 500kV magnetron reactor in September 2007 has been operated in the grid, marking that China has reached an advanced level in the field of magnetic saturation controllable reactors [24].

There are 4 to 8 series reactors in each thyristor valve unit of the HVDC converter station. The reactor generally uses the above-mentioned nonlinear magnetic saturation reactor, also called the converter valve reactor. The function of the valve reactor is to limit excessive surge current , regulate the voltage level, and protect thyristors and other crucial components. With the continuous increase of voltage and current levels, the role of converter valve reactor in the thyristor valve unit is particularly important[25]. However, frequent entering and leaving the saturation zone causes serious heat and noise problems in the reactor. To avoid noise interference, the converter station is currently mainly distributed in remote suburbs away from residents, which increases the cost of maintenance and operation. In order to cope with the heating problem, converter stations are currently taking additional water cycle cooling system, which has increased the volume and cost. The literature[4, 26, 27] made a thermal analysis of the phenomenon of valve reactor heating and proposed a corresponding cooling system fault diagnosis method. For the vibration of the iron core caused by magnetostriction, various clamping measures are currently used to suppress vibrations and noises[28]. The literature[29,30] proposed two-dimensional magnetostrictive characteristics measurement model and influence factor of silicon steel sheet, but did not study the vibration

and noise of valve reactor. Although the literature[31] analyzed the mechanism of reactor noise and points out that magnetostriction is one of the main causes of noise, no effective suppression scheme is given. The literature[32] analyzed the influence of different core structures on the magnetostriction, and gave the idea of reducing the magnetostriction from changing the design structure and characteristics of the iron core material, nevertheless, the redesign of the structure of the saturable reactor is difficult and costly. .

Another typical application of magnetic saturation technology is fluxgates. The principle of the fluxgate sensor is to use the non-linear relationship between the magnetic flux intensity and the magnetic field strength of the soft magnetic material in the measured magnetic field under the saturation excitation of the alternating magnetic field[33]. Fluxgate technology was first used to measure weak magnetic fields. Because fluxgate probes have a saturated iron core, they are often called ferromagnetic probes in the former Soviet Union. Because the iron core works in saturation, it is also called magnetic saturation probes in the United States[34]. Fluxgate technology seems to be a "gate" to the measured ambient magnetic field. Through this "gate", the corresponding magnetic flux is modulated and an induced electromotive force is generated.

Fluxgate current sensor utilizes the fluxgate principle to measure the magnetic field generated by the current, so as to achieve the purpose of indirect measurement of the current. As shown in Fig. 1-1(a), the simplest single-core fluxgate current sensor works as follows: alternating excitation source u_{ex} excites high permeability nonlinear core C to symmetrical saturation, when detection the voltage in winding W_D there will only be odd harmonics in the signal spectrum. When the measured DC current is applied to the W_2 signal winding, the symmetry is destroyed. In the detection winding W_D, even-harmonic waves proportional to the DC current are generated. Thus, by detection and demodulation of the even-harmonics, the DC current can be measured. In practice, the odd-harmonic components in the detection winding W_D are much larger than the even-harmonics. In order to avoid the submergence of even harmonics, the dual iron core structure shown in Fig. 1-1(b) is used, the identical nonlinear cores C_1 and C_2 are excited by the same high-frequency transformer T. The excitation amplitudes are equal and the phases are reversed. Ultimately, in the output signal u_{ab}, the odd-harmonics cancel each other out, only the even-harmonics remain.

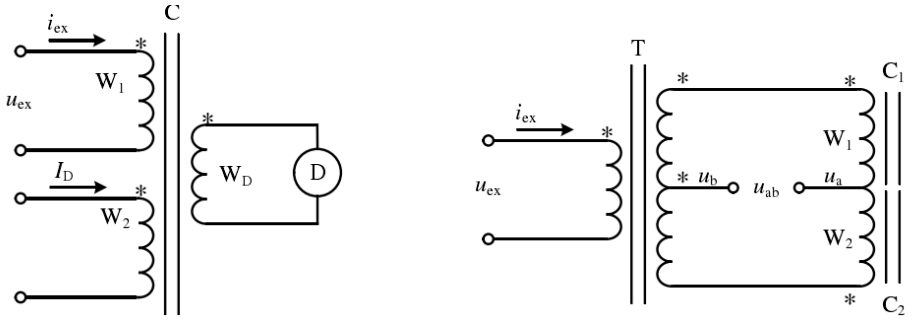

Fig. 1-1 Basic principle of fluxgate current sensor:(a) Single core structure(b) Double core

structure[35]

The crital technology of traditional fluxgate current sensors is the modulation and demodulation. The modulation method is divided into constant current source excitation and constant voltage source excitation. In practice, the constant voltage voltage source is more popular as it is less complicated in realisation than the constant current source. Voltage excitation source waveforms generally have square wave, triangular wave and sine wave, etc. Different waveforms have different effects on the sensitivity and stability of the magnetic modulation. Among different excitation waveforms, the square wave of constant voltage is stable and has the highest sensitivity. When modulating, the frequency of the excitation source needs to be strictly stable, and the excitation source frequency required is much higher than the measured current frequency. Traditional fluxgate demodulation methods commonly uses two strategies: phase-sensitive demodulation and peak-difference demodulation. Phase-sensitivity demodulation focus on the second-harmonic of the fluxgate sensor output voltage, the basic principle is to multiply the output signal with the double-frequency voltgage of the excitation, and then filtering to obtain the output result. However, the disadvantage is that the circuit structure is fairly complex, and the requirment of the performance and frequency stability of the filter are very strict and the cost is high; the peak-difference demodulation magnetic modulator outputs all even-order harmonics caused by the measured magnetic field, and is also called even-order harmonics demodulator. The advantage of peak-to-peak demodulation is that the circuit structure is relatively simple and the cost is low; the disadvantage is that the output results are with a large modulation ripple.

In the research of precision measurements of large DC current, although the current measurement metrology is very accurate, the measurement standard is usually expensive and bulky, so it is often used only for laboratory calibration and metering. In the field of industrial instrumentation, accurate measurement of DC high current is still at a relatively backward level. According to different application occasions and performance requirements, the main principles of industrial field DC high-current detection solutions are the following: shunt method, Hall effect method, magnetoresistance effect method, magneto-optical effect method, DC transformer method, fluxgate method. The main DC high-current detection technologies performance comparisons are shown in Table. 1-1[36,37]. In addition there are some other detection principles such as magnetostrictive, magneto-sensitive diodes, Short pulse discharge method, etc. However, these principles are limited due to various reasons and have not been practically applied. In the above commonly used detection technologies, the shunt method has gradually been replaced by non-contact magnetic field strength measurement methods. Hall effect-based measurement methods have been used extensively in various application scenarios[38]. In HVDC applications, the DC transformer method is frequently adopted. The complex modulation and demodulation methods of traditional fluxgates limits the use of HVDC in a certain degree. However, in recent years, self-oscillating fluxgate technology has greatly simplified the fluxgate modulation and

demodulation method.

Table. 1-1 Large DC current detection technology performance comparison

Detection principle	Measurement Range	Accuracy(ppm)	Linearty	Thermal drift(ppm/℃)	Isolation	Volume
Shunt resistor approach	A~ kA	100	medium	3	No	Bulky
Hall effect	A~ kA	5000	low	⩾50	Yes	tiny
magnetoresistive effect	A~ kA	5000	medium	100~500	Yes	medium
magneto-optic effect	kA~ MA	5000	medium	⩾100	Yes	medium
DC transformer	kA~ MA	—	high	—	Yes	bulky
Fluxgate	A~ kA	2	high	0.2	Yes	small

Self-oscillating fluxgate method is an improved method for measuring DC current using RL multivibrator based on fluxgate. This method greatly simplifies the modulation and demodulation circuit, also known as the average current model[39, 40]. The basic principle is to use multi-harmonic self-oscillatior to modulate the measured current of the primary side to the side of the self-excited circuit, and then obtains the measured current according to the linear relationship between the average value of the self-excited magnetic current and the measured current.

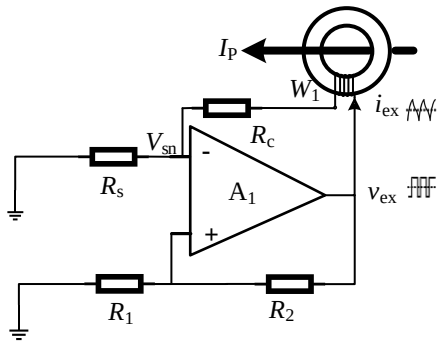

Fig. 1-2 Self-oscillating fluxgate Diagram

As shown in Fig. 1-2, in the schematic diagram of the self-oscillating fluxgate, the deeply-saturated core acts as a nonlinear inductor on the side of the excitation winding W_1, and the current at the inverting input of the comparator A_1 changes slowly due to the nonlinear inductance. After the comparison with the v_{th}, which is the results of output voltage devided by the resistor R_1 and the resistor R_2, the comparator controls the output voltage of the comparator to reverse once the inverting input exceeds v_{th}. The output voltage of the

comparator A_1 is the flux gate excitation voltage v_{ex}. When the measured current I_P is present, a DC component proportional to I_P will be generated in the excitation current branch, and the current measurement can be achieved by measuring the average voltage V_{sn} across the excitation current sampling resistor R_S.

The most remarkable advantage of the self-excited fluxgate is that unlike the traditional fluxgate, it requires no external high-precision excitation source. The modulation and demodulation circuit is greatly simplified, and the current sensitivity of the self-oscillating fluxgate is independent of the excitation frequency and core parameters. For the self-excited fluxgate, scholars have also done a lot of research. After the self-oscillating flux-gate average current model was proposed in 1991, I.M. Filanovsky and V.A. Piskarev further studied and improved the configuration. A mathematical model was established by the piecewise-linear model, and a linear estimation equation and self-oscillation conditions were proposed[41,42]. The literature[43] validated the self-excited oscillating fluxgate mathematical model based on the arctangent function of the magnetization curve and achieved a linearity of 1.2% in the ±250A range with the open-loop structure. At present, this is the highest performance achieved for the open-loop self-excited fluxgate. In 2011, the Spanish scholar G.Velasco-Quesada et al. extended the measurment range to ±700A with an accuracy of 0.2% by a three-core, three-winding configuration[44].

In China, In 2014, the scholar Yang Xiaoguang et al. simplified the three-core three-winding closed-loop measurement scheme proposed by G. Velasco-Quesada et al. and developed a two-core three-winding closed-loop self-oscillating fluxgate current sensor while reducing the number of cores. However, the measurement accuracy within ±20A at full scale is only 0.7% [45]. Yang Xiaoguang and others also improved the magnetic core and winding structure of the scheme, achieving an accuracy of 0.4% within ±25A full-scale[45-47]. In 2015, Wang Fei and his group proposed using the software demodulation method of the all-phase Fourier transform to simplify the traditional filter demodulation circuit, thereby achieving the purpose of reducing costs, but the residual current detector developed based on this method has a very small measurement range of ±2.2A, while the measurement accuracy is only 5%[48].Wang Nong's group from Harbin Institute of Technology discovered that there is an approximately linear relationship between the duty cycle of the excitation voltage of the self-oscillating fluxgate and the measured current, and developed a duty cycle model. In their experiment, the new precision current sensor has achieved a precision of 1.3ppm in the measurement range of 600A. This is so far the highest measurement achieved by closed-loop multi-core multi-winding fluxgate current technology[49,50]. Whereas, this method requires three magnetic cores and four windings, not only the volume and weight is increased, but the consistency of the three coils is difficult to guarantee after the geometric dimension is increased. Therefore, the high precision in the literature [49] cannot be realized in actual HVDC transmission. Although the demodulation circuit is simplified compared to a conventional fluxgate, the modified self-oscillating fluxgate circuit is also complicated.

1.3 Main research goals and structural arrangement

This thesis will mainly focus on the application of magnetic saturation technology. After in-depth theoretical analysis of different magnetic saturation mathematic models, the magnetic saturation technology was used to improve the existing converter valve reactor in HVDC, and a new scheme of self-excited flux gate technology to realize large DC current measurement was proposed. For the two applications above, a series of principle simulations and prototype experiments are performed in this paper. The proposed improvement of the converter valve reactor has certain guiding significance for reducing noise heating, reducing vibration, and improving the switching speed of the switching valve; in addition, a large DC current detections cheme based on magnetic saturation technology innovatively uses a single core to realizes the closed loop structure, which provides a theoretical basis for the subsequent development of a low-cost, small-volume, high-precision DC large current sensor product. The main structure of this paper is as follows:

In the first chapter, the current research status of magnetic saturation technology is reviewed, and two applications: the development scheme of the converter valve reactor in HVDC and the large DC current detection are given. In the second chapter, several main theoretical models of magnetic saturation are briefly introduced, in which the model based on J-A theory is deduced in detail. Based on the theoretical model in Chapter two, the third chapter discusses the validity of the magnetic saturation technology in valve reactor improvement and its simulation and verification. Then the linear relationship of the proposed new DC current measurement scheme is deduced and a simulation of the principle is conducted. In the fourth chapter, experimental verification is carried out, in which the main key performance indexes of the proposed large DC high current detection scheme are carefully tested. Due to the lack of support for research funds and experimental conditions, the experimental part of this paper adopts a small prototype. The fifth chapter summarizes the full-text research work and results, and gives a outlook of more applications of magnetic saturation technology.

2 Magnetic saturation models

Involving magnetic saturation applications, the propoer magnetization curve model selection is the key. For ease of understanding, magnetic saturation phenomenon is firstly discribed below. In the schematic diagram of the magnetization process shown in Fig. 2-1(a), the horizontal axis is the magnetic field strength *H*. It is a auxiliary physical quantity introduced by the Ampere's loop theorem and actually has no physical meaning. The vertical axis is the magnetic induction intensity *B*, also known as the magnetic flux density, represents the magnetic flux per unit area in the magnetic medium, is used to describe the strength of magnetic induction, and it is also a physical quantity to describe the energy of the magnetic field. There exists a constitutive relationship between *H* and *B*: $B=\mu H$.

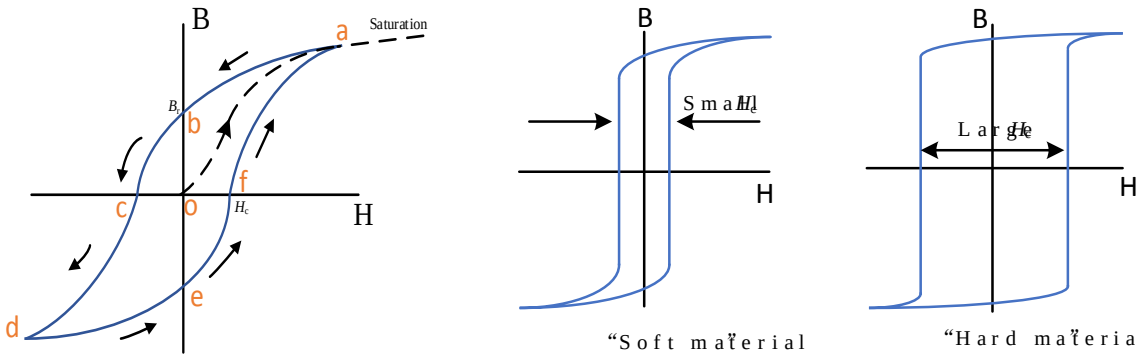

Fig. 2-1 (a) Magnetization process diagram(b) Different shape of magnetization curves

The magnetization process of the ferromagnetic material is as follows. As the external magnetic field *H* gradually increases, the magnetic induction intensity *B* rises along the initial magnetization curve oa; if the external magnetic field increases to H_m, *B* basically remains unchanged and the material reaches magnetic saturation, where H_m is called the saturation magnetic field strength of the material; gradually decreases *H*, due to internal magnetic domain interaction, the magnetic induction *B* at this time does not repeat the increasing track, but decreases along the curve ab. When *H* decreases to zero, *B* does not return to zero, the magnetic induction *B* at this time is denoted as B_r, named as the remanence of the ferromagnetic material. To make the magnetic induction *B* again reduce to zero, it is necessary to add a reversed external magnetic field $-H_c$, H_c is called coercive force ,whose magnitude indicates how hard the material can be magnetized, and in Fig. 2-1(a) it is shown by two points c and f. If the magnetic field in the opposite direction continues to increase, the core will follow the cd to reach the reverse saturation; likewise, after reaching the inverse saturation, the magnetic induction *B* will not follow the original track but will change along de, ef and fa when demagnetization. Therefore, in the process of repetitive magnetization, the change in the magnetic induction *B* always lags behind the change in the magnetic field strength *H*,that is the so-called hysteresis. The hysteresis shapes of different materials are different, for example, the magnetic hysteresis loop area of the soft magnetic

materials and hard magnetic materials are significantly different, as shown in Fig. 2-1(b). At present, there are two mathematical models of hysteresis loop mostly common used: Preisach model and Jiles-Atherton model. In practice, in order to reduce the computational complexity of the project, the magnetization curve of the material generally adopts a reasonable simplification to the hysteresis loopback according to different applications. In this chapter, the Preisach model is briefly introduced firstly, then the Jiles-Atherton model is deduced in detail, and finally the piecewise linear magnetization curve model commonly used in fluxgate research is derived.

2.1 Preisach model

Originally, the Preisach model of hysteresis generalized magnetic hysteresis as relationship between magnetic field and magnetization of a magnetic material as the parallel connection of independent relay hysterons. The Preisach hysteresis model was first proposed by the German physicist Ferenc (Franz) Preisach in 1935 and has been widely accepted as a general mathematical tool for the description of hysteresis phenomena of different kinds[52,53]. In the field of ferromagnetism, the Preisach model is sometimes thought to describe a ferromagnetic material as a network of small independently acting domains, each magnetized to a value of either *h* or *-h*. A sample of iron, for example, may have evenly distributed magnetic domains, resulting in a net magnetic moment of zero.

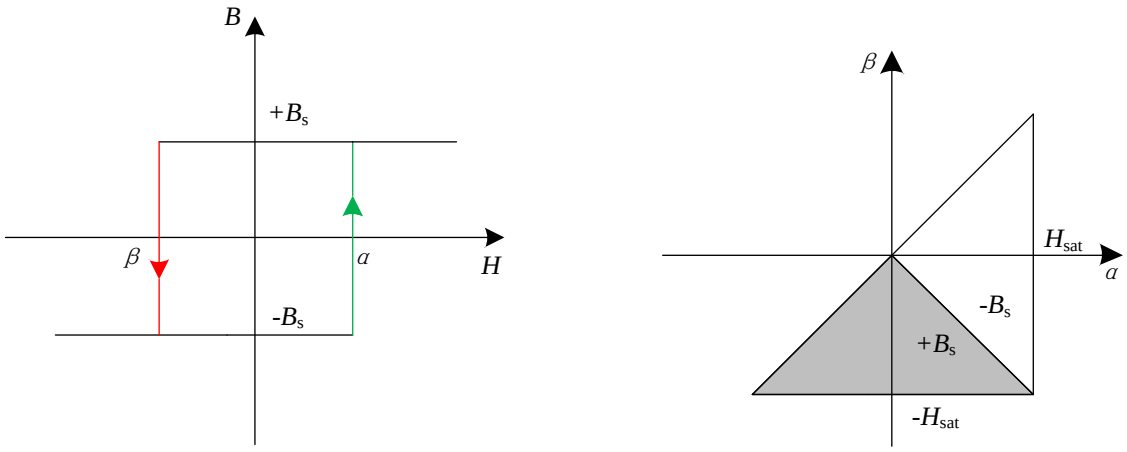

Fig. 2-2 (a) I/O map of the relay hysteron, (b) the Preisach function diagram on the (α, β) plane

The relay hysteron is the fundamental building block of the Preisach model. It is described as a two-valued operator denoted by $R_{\alpha,\beta}$. Its I/O map takes the form of a loop, as shown in Fig. 2-2(a). α defines the "switch-off" threshold, and β defines the "switch-on" threshold. Graphically, if H is less than α, the output is "low" or "off." As we increase H, the output remains low until H reaches β —at which point the output switches "on". Further increasing H has no change. Decreasing H, output does not go low until H reaches α again. It is apparent that the relay operator $R_{\alpha,\beta}$ takes the path of a loop, and its next state depends on its past state. Different relay hysterons have different α and β value, which have certain

distribution rules in the Preisach plane. The distribution is expressed by a non-negative binary function $\mu(\alpha, \beta)$,named the Preisach function. $\mu(\alpha, \beta)$ should have the following properties:

1)If $\alpha<\beta$, $\mu(\alpha, \beta)=0$;

2)If $\alpha>H_{sat}$ or $\beta< -H_{sat}$, $\mu(\alpha, \beta)=0$;

3) $\mu(\alpha, \beta)= \mu(-\beta, -\alpha)$

Consider a plane of coordinates $\alpha\beta$. On this plane, each point is mapped to a specific relay hysteron $R_{\alpha,\beta}$. Considering only the half-plane as any other case does not have a physical equivalent in nature according to the property 3) of $\mu(\alpha, \beta)$, we can present the Preisach density function, denoted $\mu(\alpha, \beta)$. This function describes the amount of relay hysterons of each distinct values of (α, β). As a default we say that outside the right triangle$(\alpha, \beta)=0$, shown in Fig. 2-2 (b). The classical Preisach theory considers the macroscopic magnetic properties of materials as a summation of all relay hysterons multiplied by the weight factor $\mu(\alpha, \beta)$[54], so the magnetic flux density of the iron core can be expressed as：

$$B(H) = \iint_{+B_s} B_s \mu(\alpha, \beta) \mathrm{d}\alpha \mathrm{d}\beta - \iint_{-B_s} B_s \mu(\alpha, \beta) \mathrm{d}\alpha \mathrm{d}\beta \qquad (2\text{-}1)$$

In practical applications, a discrete Preisach model is mostly used. In biref, the Preisach model consists of many relay hysterons connected in parallel, given weights, and summed, as shown in Fig. 2-3 (a), the discrete Preisach model consists of N magnetic dipoles. Fig. 2-3 (b) gives the hysteresis of the normalized discrete preisach model. From Fig. 2-3, it is readily to see that the larger N is, the closer the discrete Preisach model is to the true hysteresis loop, graghically, the smoother the hysteresis loop.

Resorting to the distribution function of relay hysterons, the classical Preisach theory successfully solves the multi-valued problem of hysteresis loops. Based on the classical Preisach theory, several new Preisach models have been developed. For example, the Mobile Preisach Model (MPM) considers the cross-effect of the material's magnetic field and background magnetic field; the dynamic Preisach model (DPM) takes into account the applied magnetic field frequency factor; and the vector Preisach model can be used to deal with the uniaxial anisotropy of the material in which the magnetization and magnetic field strength are not in the same directions[54]. These further-developed models are based on the the classical Preisach theory and are not given detailed explaination.

The main drawbacks of the Preisach Models are as following: it is inadequate to express magnetic saturation and lacks of physical meaning. Due to the use of the relay hysterons's distribution density function $\mu(\alpha,\beta)$, the Preisach theory is only applicable to core unsaturation conditions for $|H|\geq H_{sat}$, thus the Perisach theory is not suitable for expressing saturation. As for the hysteresis loop, the Perisach theory is only expressed by defining a

relay hysteron with hysteresis. For the physical interpretation of hysteresis, this theory is not involved. Moreover, the model lacks the connection with the physical parameters of the magnetization curve ,thus limits the understanding and application of this model.

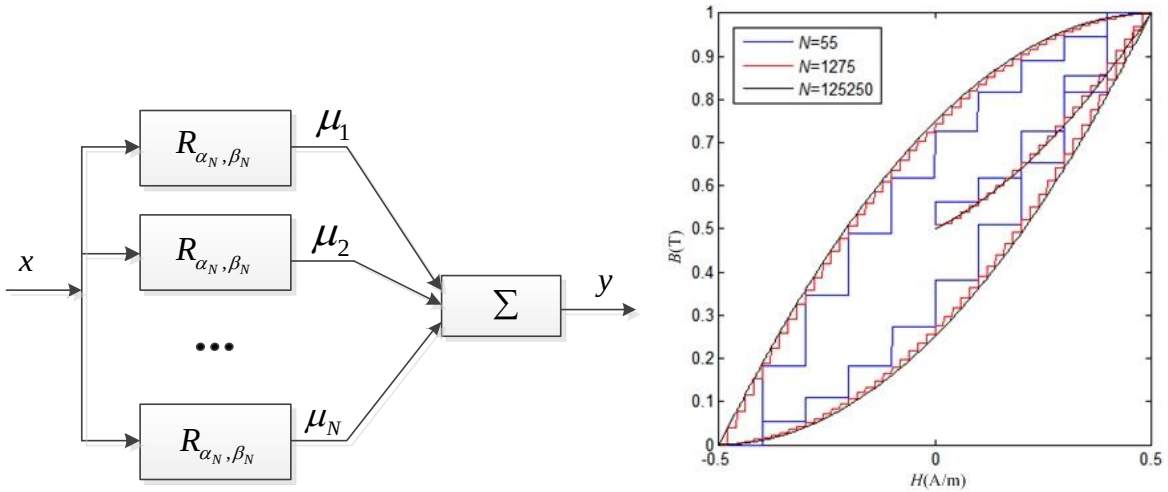

Fig. 2-3(a).the block diagram of the discrete Preisach model (b). Preisach model with different N

2.2 Jiles–Atherton model

The Jiles–Atherton model of magnetic hysteresis was introduced in 1984 by David Jiles and D. L. Atherton[55-57]. This is one of the most popular models of magnetic hysteresis. Its main advantage is the fact that this model enables connection with physical parameters of the magnetic material. Since its introduction in 1984, Jiles–Atherton model was intensively developed. As a result, there also exists some derivation errors. To guarantee the validity, the model is detailed re-derived according to the original version of Jiles and Atherton.

The Jiles–Atherton model decomposes the magnetization into the reversible part M_{rev} and the irreversible part M_{irr}. The reversible part M_{rev} shows the effect of the hysteresis elastic deformation. The irreversible part M_{irr} manifests the influence of the magnetic domain restraining point formed by the discontinuous material structure and is similar to the friction effect. The relationship between reversible magnetization intensity and irreversible magnetization iis as following:

$$M = M_{\mathrm{rev}} + M_{\mathrm{irr}} \tag{2-2}$$

$$M_{\mathrm{rev}} = c(M_{\mathrm{an}} - M_{\mathrm{irr}}) \tag{2-3}$$

In the equation above: c is the magnetization reversibility； anhysteretic magnetization M_{an} is calculated for effective magnetic field H_{e}. J-A theory uses improved Langevin's equation to describe anhysteretic magnetization M_{an}[55],as following：

$$M_{an} = M_s(\coth(\frac{H_e}{a}) - \frac{a}{H_e}) \tag{2-4}$$

Where M_s is the saturation magnetization of material; H_e is effective magnetic field; interdomain coupling coefficient a is a parameter used to modify the shape of anhysteretic hysteresis loop.

Assume M_s=1, the equation(2-4) is shown in Fig. 2-4. The shape of the function is different for different values of a. The larger the value of a is, the smoother the change of function is. It is worth noting that the function is not continuous at the zero effective magnetic field point.

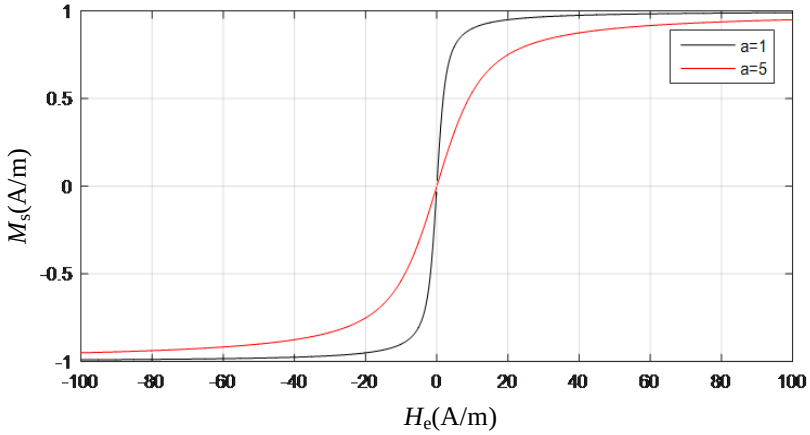

Fig. 2-4 Langgevin function diagram

According to the properties of the Langgevin function, when the effective magnetic field H_e approaches zero, the anhysteretic magnetization M_{an} goes to zero, and when H_e approaches infinity, M_{an} tends to M_s, which is consistent with the magnetic saturation phenomenon. Effective magnetic field H_e directly affects the internal magnetic moment, and its value is equal to the applied magnetic field strength H and the ferromagnetic material magnetization M multiplied by a proportional coefficient used to quantify interdomain coupling in the magnetic material, i.e.:

$$H_e = H + \alpha M \tag{2-5}$$

The energy loss during magnetization is caused by the irreversible magnetization part M_{rev}:

$$\Delta E = k\Delta M_{irr} \tag{2-6}$$

Based on the above equation, literature [56,57] gives the energy conservation expression of hysteresis magnetization process:

$$M_{irr} = M_{an} - \delta k \frac{dM_{irr}}{dH_e} \tag{2-7}$$

Where parameter *k* quantifies interdomain coupling in the magnetic material. Although *k* is a variable in physics and it varies with the change of the magnetic field strength *H*, Jiles has verified in publication[57] that taking *k* as a constant would not deteriorate the accuracy of the model. In order to ensure the simplification of the model, *k* is considered as constant in this paper. The second part on the right side of equation(2-7) represents the hysteresis loss. The function δ represents the characteristic of the repulsiveness to the the change of magnetic field. The output of δ only takes ±1; if *H* increases, δ=1, viceversa, δ = -1. From the expression (2-7), the following equation can be derived:

$$\frac{\mathrm{d}H_{\mathrm{e}}}{\mathrm{d}M_{\mathrm{irr}}}=\frac{\mathrm{d}H_{\mathrm{e}}}{\mathrm{d}H}\frac{\mathrm{d}H}{\mathrm{d}M_{\mathrm{irr}}}=\frac{\delta k}{M_{\mathrm{an}}-M_{\mathrm{irr}}} \tag{2-8}$$

Take derivatives of the equation (2-5) with respect to *H*, the following equation is obtained:

$$\frac{\mathrm{d}H_{\mathrm{e}}}{\mathrm{d}H}=1+\alpha\frac{\mathrm{d}M}{\mathrm{d}H} \tag{2-9}$$

Combine equation (2-8) and equation (2-9):

$$\frac{\mathrm{d}H}{\mathrm{d}M_{\mathrm{irr}}}+\alpha\frac{\mathrm{d}M}{\mathrm{d}M_{\mathrm{irr}}}=\frac{k\delta}{M_{\mathrm{an}}-M_{\mathrm{irr}}} \tag{2-10}$$

Since:

$$\frac{\mathrm{d}M}{\mathrm{d}M_{\mathrm{irr}}}=(1-c)+c\frac{\mathrm{d}M_{\mathrm{an}}}{\mathrm{d}M_{\mathrm{irr}}} \tag{2-11}$$

Combine equation (2-10) and (2-11)：

$$\frac{\mathrm{d}M_{\mathrm{irr}}}{\mathrm{d}H}=\frac{M_{\mathrm{an}}-M_{\mathrm{irr}}}{k\delta-\alpha(1-c)(M_{\mathrm{an}}-M_{\mathrm{irr}})-c\dfrac{\mathrm{d}M_{\mathrm{an}}}{\mathrm{d}M_{\mathrm{irr}}}(M_{\mathrm{an}}-M_{\mathrm{irr}})} \tag{2-12}$$

Because *c* is generally small, equation(2-12) can be simplified as:

$$\frac{\mathrm{d}M_{\mathrm{irr}}}{\mathrm{d}H}=\frac{M_{\mathrm{an}}-M_{\mathrm{irr}}}{k\delta-\alpha(M_{\mathrm{an}}-M_{\mathrm{irr}})} \tag{2-13}$$

Combine the equation (2-13) with (2-11), we can get：

$$\frac{\mathrm{d}M}{\mathrm{d}H}=(1-c)\frac{M_{\mathrm{an}}-M_{\mathrm{irr}}}{k\delta-\alpha(M_{\mathrm{an}}-M_{\mathrm{irr}})}+c\frac{\mathrm{d}M_{\mathrm{an}}}{\mathrm{d}H} \tag{2-14}$$

According to the equation (2-2) and the equation (2-3), M_{irr} can be expressed as a function of M_{an} and M：

$$M_{\mathrm{irr}} = \frac{M - cM_{\mathrm{an}}}{1-c} \tag{2-15}$$

At last, The iterative solution can be obtained by using the differential equation of (2-14), equation (2-4) and equation (2-15). Since:

$$B = \mu_0(M + H) \tag{2-16}$$

By the iteration of the formula (2-14), the classical hysteresis model can be obtained.

Above all, the description of the classical Jiles-Atherton model requires only five parameters: the saturation magnetization M_s, shape parameter α that quantifies interdomain coupling in the magnetic material, parameter a that quantifies domain walls density in the magnetic material, the reversible susceptibility coefficient c and the energy-related parameter k that characterize the hysteresis losses. Each parameter has a different influence on the hysteresis curve. M_s mainly influences the maximum magnetization in the hysteresis loop, the magnetic permeability and the remanence value in the vicinity of the coercive force; parameter k and c determine the coercivity, magnetism, and the area of the hysteresis loop, in fact, they have the opposite effects; α determines the permeability and remanence of the area near the coercive force; parameter a affects the gradient in vicinity to B_r and the remanence value. The influence of the parameters on the hysteresis loop is shown in Table 2-1.

Table 2-1 The impact of the Jiles-Atherton model's parameters on the hysteresis loop

parameters	Remanence(B_r)	Coercivity(H_c)	Permeability at H_c	Loop area	Max-magnetization
M_s↑	↑	−	↑	−	↑
α↑	↑	−	↑	−	−
a↑	↓	−	↓	−	−
k↑	↑	↑	−	↑	−
c↑	↓	↓	−	↓	−

The Jiles-Atherton model is a mathematical hysteresis model based on the internal energy balance principle of ferromagnetic materials. In this model, the magnetostatic energy corresponds to the reversible magnetization M_{rev}, and the hysteresis loss corresponds to the irreversible magnetization M_{irr}; as shown in Table 2-1, The model is described with five parameters, and the parameters are directly related to the physical parameters. The model is close to the physical model; in addition, when the external magnetic field strength increases infinitely, thanks to the properties of the Langgevin function, the anhysteretic magnetization is still convergent, so the model can describe the hysteresis loop and magnetic saturation at the same time. Therefore, this model is adopted later in the application of valve reactors.

2.3 Piecewise linear magnetization curve model

In the engineering application research such as transformer cores, especially when the core enters saturation, the multi-value problem of hysteresis loop greatly increases the complexity and difficulty. In order to simplify the model, hysteresis loops are generally approximated by various single-value curves. For example, an AC magnetic curve commonly used in magnetic field calculation is defined as a curve generated from a set of data consisting of the peak value H_m of the magnetic field strength waveform and the peak value B_m of the magnetic flux density under different magnetization intensity, which is usually measured by experimental test [58]. In deriving the self-oscillating fluxgate average current model, M. M. Ponjavic and R. M. Duric at the University of Belgrade first used the arctangent function model based on the magnetization curve[59]:

$$B(H) = \frac{\mu_0 \mu_m \arctan(kH)}{k} \tag{2-17}$$

Where μ_0 represents the vacuum permeability，and equals to $4\pi \times 10^{-7}$ H/m; μ_m is the maximum magnetic permeability，k is a scale factor. Since when the magnetic field strength H approach infinity, the magnetization intensity B can not increase infinitely and should eventually go to the saturated B_s, as shown in the following:

$$\lim_{H \to \infty} B(H) = \frac{\pi \mu_0 \mu_m}{2k} = B_s \tag{2-18}$$

From equation (2-18) we can express k with μ_0, μ_m, and B_s and substitute it in (2-17):

$$B(H) = \frac{\arctan(\frac{\pi \mu_0 \mu_m H}{2B_s})}{\frac{\pi}{2B_s}} \tag{2-19}$$

As shown in Fig. 2-5(a), the arctangent magnetization curve is closer to the AC magnetization curve of the material and can be expressed in analytical solutions, thus it is widely used in engineering; when the core is saturated, the calculation is often performed in a further simplification. The piecewise linear model shown in Fig. 2-5(b) is a commonly used simplified model. When saturation occurs, the magnetic permeability sharply decreases. At this time, the change of permeability in the unsaturated zone can be neglected and the permeability can be treated as a constant. Therefore, in the piecewise linear magnetization curve, the material magnetization curve is approximated by two straight line in the saturation region and the non-saturation region respectively. After saturation, the magnetic induction B changes slowly with the magnetic field strength H, and the gradient of the straight line is much smaller than that of the non-saturated area.

The risk of the three-segment piecewise linear model comes from the fact that the B-H curve

in the unsaturated zone is approximated by a straight line, i.e. the permeability change in the unsaturated zone is ignored, only when the material is deep saturated, the error of this approximation becomes tolerable. The piecewise linear magnetization curve is more concerned with the saturation characteristics of the material. The three-segment nonlinearity shown inFig. 2-5(b) can not only simplify the nonlinear system into a linear system, but also tightly integrate the physical model of magnetic saturation.

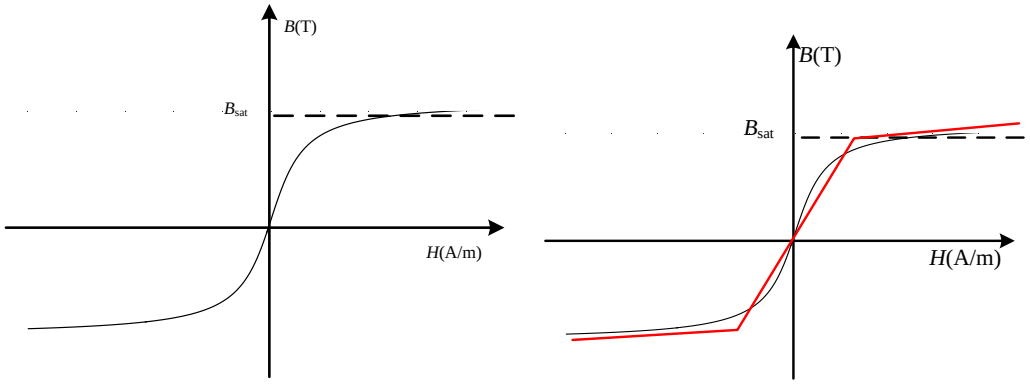

Fig. 2-5 (a) Arc tangent magnetization curve (b) 3-Piecewise linear magnetization curve

2.4 Chapter Summary

There are mainly two widely accepted mathematical models to describe hysteresis loop: Preisach model and Jiles-Atherton model. This chapter first gives a brief introduction to the Preisach model. It points out that the main inadequacy of the Preisach model is that it can not describe the magnetic saturation phenomenon and the less connection with physical parameters. Then, this chapter deduces the Jiles-Atherton model in detail and analysises the influence of the five parameters to the hysteresis loop. At last, the picewise linear magnetization curve model commonly used in fluxgate technology is derived.

3 Controllable valve reactor and self-oscillating fluxgate large DC current detection principle

3.1 Controllable valve reactor based on Jiles-Atherton model

Thyristor valves for AC-DC conversion are essential components of the HVDC transmission system. They usually consist of some modules constructed with basic components such as thyristors and snubber circuit as well as valve reactors.The anode reactor is a complex component that provides wide range of variations in designing such as the inductance, the residual resistance and the stray capacitance between the winding and the core.The role of the converter valve reactor is to limit the impact of "inrush current increase rate" to the converter thyristor. Most existing converter valve reactors use an uncontrollable structure. Even if a saturable reactor is used, the converter valve will frequently switch between the unsaturated zone and the saturated zone due to the frequent zero-crossing of the AC side current. In the alternation of saturated and unsaturated regions, the inductance changes drastically, which eventually leads to noise, heat, and other problems in the operation of the reactor. The magnetic saturation technology is used to optimize the existing valve reactors, and the bias magnetic control windings are added on the basis of the existing valve reactors. As shown in Fig. 3-1, the magnetic saturation depth is controlled by the bias magnetic current I_b to make the core of the reactors is always in controllable saturation state, which avoids problems such as noise, heating, caused by the hysteresis. The permeability of the iron core is inversely proportional to the saturation of the iron core. The inductance of the reactor decreases as the core saturation increases. After the improvement, the valve reactor is always in the saturation region during normal operation, and has good linear control characteristics. The saturation of the core is controlled by the bias current I_b, which achieves a linear control of the valve reactor’s inductance.

In the process of the optimization to the converter valve reactor, a nonlinear inductor and an ideal transformer are used to substitute the improved valve reactor. Concerning the engineering description of nonlinear inductors, most current researches use the current-flux experimental model, which ignores the hysteresis of the core and approximates a single-valued function with B as H. When the magnetic permeability is very high, the B-H curve of the iron core is long and narrow, and the hysteresis loop encloses a small area. This approximation can be accepted. However, there are two problems in this approximation. Firstly, when the air gap exists, the equivalent magnetic permeability decreases, and this approximation becomes very rough. Secondly, it is impossible to describe the iron energy loss of the reactor if power consuming is considered. The model must be further modified by introducing parallel nonlinear resistors. For example, literature[60] uses a non-linear inductor and a non-linear resistor in parallel as the equivalent model of the valve reactor. The nonlinear resistor is mainly used for various power losses of equivalent electromagnetic transients. Therefore, for the nonlinear inductance model, this paper uses the Jiles-Atherton

model deduced in Chapter 2 to model its hysteresis loop characteristics.

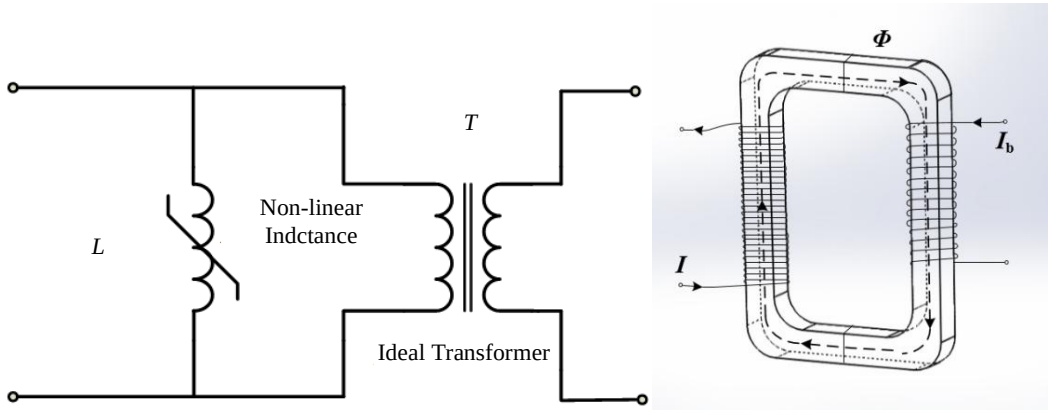

Fig. 3-1 Valve reactor improvement model and schematic

3.1.1 Principle of the controllable valve reactor

In the converter valve, assuming that the current flows through the thyristor is a pulsating current, the core of the traditional saturable reactor is working in the first quadrant during normal operation, i.e. only the forward current passes through the reactor, and the state of the core is shown in Fig. 3-2 .When the power semiconductor in the converter valve is switching according to the current diagram shown in Fig. 3-2, the saturable reactor operates in the area ①. The reactor circles the outline of area① for each rectification cycle, and the magnetic flux density changes ΔB is relatively large. As a result, the shape of the iron core caused by the corresponding magnetostrictive effect changes significantly, i.e. if the magnetic flux density periodically changes in a large range, the core will undergo extension and contraction in geometric dimensions. One causes of vibration and noise of the reactor is from the periodic extension and contraction of the iron core. Unlike the vibration caused by the electromagnetic force, the iron core usually has a relatively large mass, thus the traditional mechanical clamping method for denoising and vibration damping has little effect to the magnetostriction, especially when the iron core has an air-gap, the vibration caused by magnetostriction is more serious.

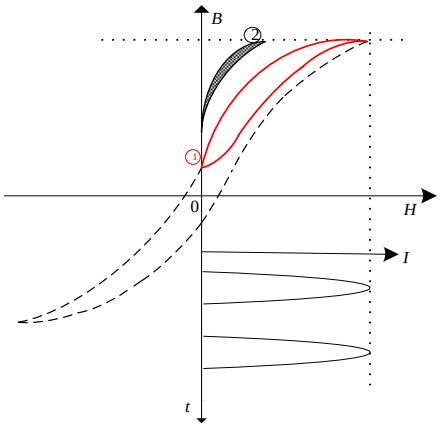

Fig. 3-2 Operational diagram of hysteresis loop for saturable valve reactor

After the controlling bias winding is added, the magnetic field strength H_{total} is a superimposition of the working magnetic field strength H and the controlling bias magnetic intensity H_{b}, that is:

$$H_{\text{total}} = H + mI_{\text{b}} \tag{3-1}$$

Where m is a coefficient related to the number of turns of the controlling bias currents and its effective length of the magnetic circuit. As I_{b} is a DC current whose differential value is zero, we can obtain:

$$\frac{\mathrm{d}M}{\mathrm{d}H} = \frac{\mathrm{d}M}{\mathrm{d}H_{\text{total}}}\frac{\mathrm{d}H_{\text{total}}}{\mathrm{d}H} = \frac{\mathrm{d}M}{\mathrm{d}H_{\text{total}}} = \frac{M_{\text{an}} - M_{\text{irr}}}{k\delta - \alpha(1-c)(M_{\text{an}} - M_{\text{irr}}) - c\dfrac{\mathrm{d}M_{\text{an}}}{\mathrm{d}M_{\text{irr}}}(M_{\text{an}} - M_{\text{irr}})} \tag{3-2}$$

$$M_{\text{an}} = M_{\text{s}}\left(\coth\left(\frac{H_{\text{e}}}{a}\right) - \frac{a}{H_{\text{e}}}\right) = M_{\text{s}}\left(\coth\left(\frac{H_{\text{total}} + \alpha M}{a}\right) - \frac{a}{H_{\text{total}} + \alpha M}\right) \tag{3-3}$$

Comparing the equations(3-2), (3-3) and the iterative equations of the Jiles-Atherton model deduced in Chapter two, we can see that when I_{b} is an independent external DC component, the shape of the hysteresis loop remains unchanged, only a translation in the magnetic field strength H axis. Fig. 3-3 shows the hysteresis loop calculated by the iterative Jiles-Atherton model using Matlab. The blue solid line is the result of I_{b}=0.2A while the red dotted line is I_{b}=0. It can be intuitively seen from the figure that owning to the influence of I_{b}, the forward saturation magnetic field strength decreases, the reverse saturation magnetic field increases, the shape of the magnetic hysterisis loop remains unchanged, except an offeset to the left of the whole shape.

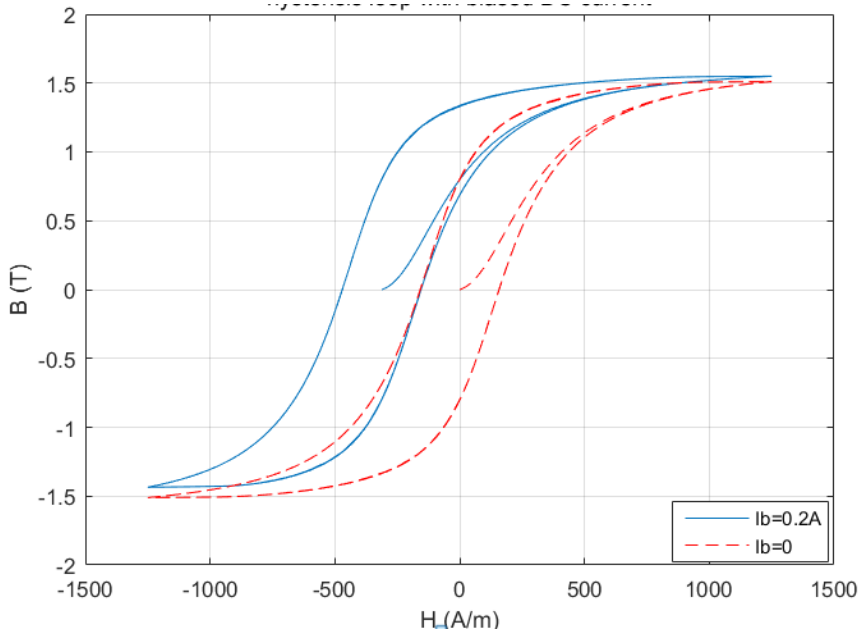

Fig. 3-3 DC bias magnetic hysteresis loop based on Jiles-Atherton model iterative

The iron loss of the saturable reactor is one of the causes of the temperature rise of the

reactor. There are two main reasons for transformer iron loss: eddy current and hysteresis loss. The essence of eddy currents is the Joule heat loss caused by the varing magnetic field; the hysteresis loss is essentially the inconsistency of the magnetization and demagnetization *B-H* curves, i.e, the hysteresis loop. According to the magnetic field energy formula: $\omega=1/2BH$, where ω represents magnetic energy density, in the *B-H* curve, the core loss should be proportional to the area enclosed by the magnetization and demagnetization curves. After controlling the reactor's working curve according to Fig. 3-2, the closed area of the *B-H* curve decreases, and the hysteresis loss also decreases accordingly, thus, the heat generation can be reduced. In addition, when the working curve is moved from area① to area② in Fig. 3-2 , the working magnetic flux density change ΔB becomes significantly smaller, and the noise and vibration caused by magnetostriction also decrease.

Besides, the introduction of conventional saturable reactors will limit the thyristor switching speed. In the DC converter valve, the switching-off time of the thyristor is an important parameter. After the saturable reactor is connected in series to protect the thyristor, the switching-off time is often greatly prolonged and the thyristor performance is reduced. For traditional valve reactors, the valve reactor current gradually decreases toward zero during the shutdown process, and the reactor core exits the saturation region. Because the inductance control during non-saturation is very nonlinear, to effectively protect the thyristor, there is a large amount of margin in the design, which further increases the turn-off time. Moreover, the process for current changing to saturation also reduces the switching speed of the converter valve. In the *R-L* series circuit, for the time constant $\tau = L/R$, when the line equivalent resistance is constant, the time constant changes with the inductance of the reactor, the inductance decreases, the time constant decreases, and the current saturation time decreases. According to reactor calculation equation:

$$L = \frac{\mu N^2 A}{l} \tag{3-4}$$

Where L is the inductance; μ is the permeability; N is the number of turns in the reactor winding; A is the effective cross-sectional area in magnetic circuit; l is the core effective path length.

A schematic diagram of the reactor inductance change is shown in Fig. 3-4. In fact, if the hysteresis loop effect is considered, the inductance value should also be a multi-valued loop, but for ease of understanding, the magnetic permeability on the average magnetization curve is adopted for approximation. Despite a certain errors, the validity of the analysis will not be influenced. In area① of the Fig. 3-2, during the switching-off of the thyristor, the operating current continuously changes from maximum to zero, and the inductance also increases accordingly. However, after controlling the working curve from area① to area②, the iron core is still close to saturation due to the effect of controlling bias magnetic field during the process of the working current being reduced to zero. The inductance can still maintain a

small value during the whole process. Moreover, compared with the unsaturation area which the traditional reactor will inevitably enter, the change of the inductance in the saturation region is smaller, and there is no need to reserve a large margin during the design of the inductance value. Therefore, the current saturation time can be reduced by this controlling winding and the corresponding DC valve switching rate can be improved.

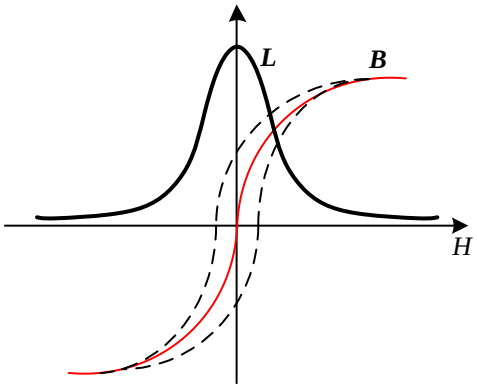

Fig. 3-4 the change diagram of saturable reactor inductance

This paper proposes to use magnetic saturation controllable reactor to replace the traditional valve reactor so that can move the reactor's working curve from area① to area② in Fig. 3-2. By applying a controlling bias winding, the operating magnetic flux density change ΔB becomes smaller, thus the variation of the core is reduced from the source, meanwhile, the switching speed of the thyristor is improved.

3.1.2 Simulation Verification

Simulink, developed by MathWorks, is a graphical programming environment for modeling, simulating and analyzing multidomain dynamical systems. Its primary interface is a graphical block diagramming tool and a customizable set of block libraries. It offers tight integration with the rest of the Matlab environment and can either drive Matlab or be scripted from it. Simulink is widely used in automatic control and digital signal processing for multidomain simulation and model-based design. Matlab 2015 version has added nonlinear inductance module based on J-A model to Simulink. The nonlinear inductor in the elec_lib Passive Devices library provides a variety of non-linear relationships. As shown in Fig. 3-5, 10 parameters are used in Simulink to define the nonlinear inductance based on the Jiles-Atherton model. In this paper, all simulations in Simulink take those parameters.

Firstly, the parameters in Fig. 3-5 is briefly explianed. The nonlinear inductance parameters that define the Jiles-Atherton model can be classified into three categories: geometry parameters, Jiles-Atherton hysterisis parameters, and parasitic parameters. The geometric parameters consist of the number of turns of the coil, the effective magnetic path length, and the effective cross-sectional area, which determine the size of the nonlinear inductor and the winding; the Jiles-Atherton model parameters are slightly different from those derived in the second chapter. The Jile-Atherton model in the second chapter consists of the saturation

magnetization M_s, shape parameter α that quantifies interdomain coupling in the magnetic material, parameter *a* that quantifies domain walls density in the magnetic material, the reversible susceptibility coefficient *c* and the energy-related parameter *k* that characterize the hysteresis losses. However, when determining the anhysteretic magnetization curve, the original function equation is complex and not continuous while H=0, thus, Matlab substitutes the parameters by the gradient at H=0 and a random data point on the anhysteretic magnetization curve (B_x, H_x). For the rest parameters, it is identical with the Jiles-Atherton model; The parasitic conductance of the nonlinear inductor is also given and can be set to zero when not required.

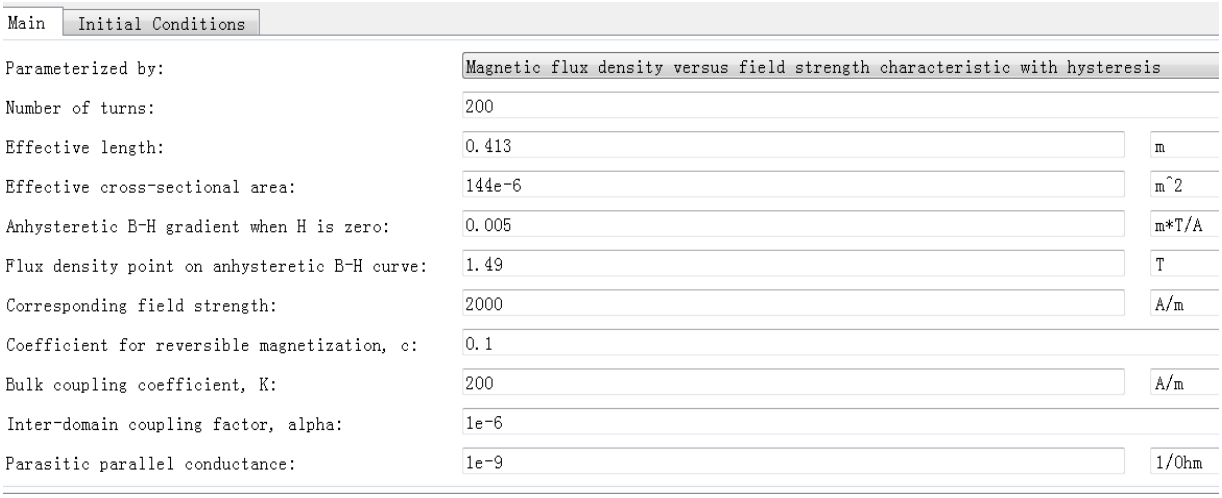

Fig. 3-5 Jiles-Atherton models of Non-linear inductance parameters in Simulink

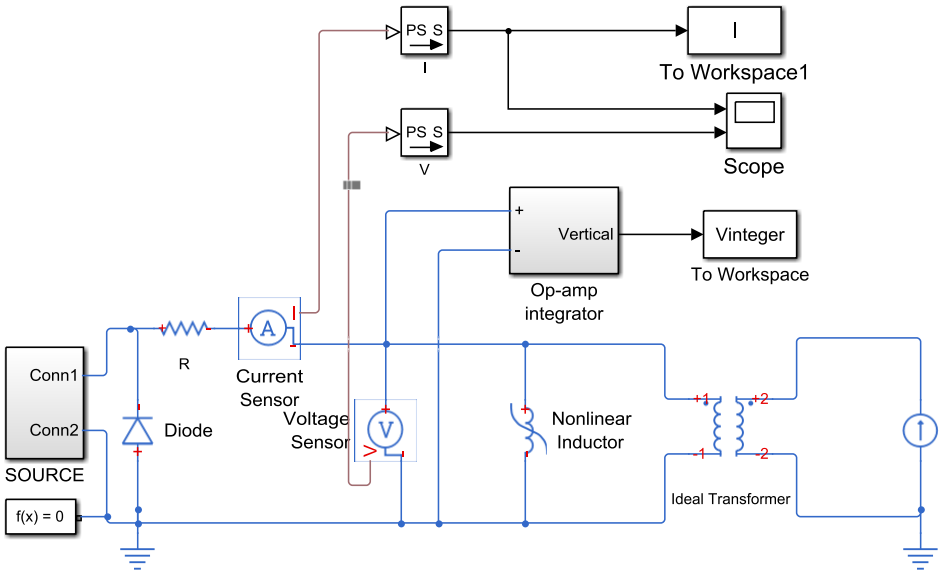

Fig. 3-6 Simulink block diagram

As shown in Fig. 3-6, the simulation model shown in Simulink is accomplished to verify the correlation analysis based on Fig. 3-3. The valve reactor is connected in parallel with the ideal transformer using a nonlinear inductor, the ideal transformer turns ratio is set to 1, and

the bias current I_b is simulated by appling constant current to the secondary winding. During the simulation, the valve reactor is connected in series to the resistor diode circuit. The voltage-controlled voltage source output is controlled by the 60Hz, 10V pulse generator sequence.The current I and terminal voltage V of the valve reactor are measured, and according to the Ampere Circuital Law and the formula of the induced potential, the following equations can be obtained:

$$H = \frac{NI}{l} \tag{3-5}$$

$$B = \int \frac{V}{N} dt \tag{3-6}$$

Where N represents the turns of winding and l represents the length of the magnetic circuit.

After the processing of the current and voltage using the above equations, the simulation B-H curve with different controlling bias current I_b is plotted in Fig. 3-7. The results of the simulation are basically consistent with the predictions in Fig. 3-3. The core works in the first quadrant of the B-H curve: when the DC bias current is not applied, the working magnetic flux density of the inductor core is about 0.95T-1.6T; after applying the controlling bias current I_b, the core barely exits the non-saturation region when the current is zero, and the vary of the working magnetic flux density continuously decreases with the increase of the controlling current I_b. It can be seen from Fig. 3-7 that when I_b =0.4A, Even if the operating current is reduced to zero, due to the control effect of the bias current, the working flux density is basically maintained at 1.5T-1.6T, that is, the core does not basically exit the saturation region. It can also be seen from Fig. 3-7 that the area enclosed by the working curve decreases for the existance of the control bias winding, thus the hysteresis loss decreases.

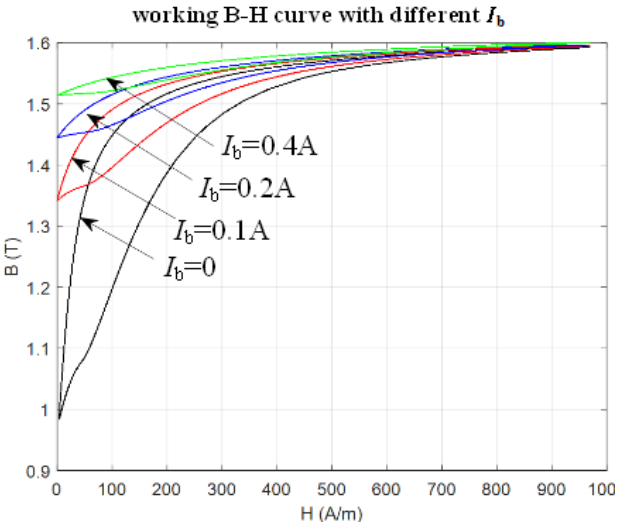

Fig. 3-7 the results of the simulation

The simulation results are consistent with the analysis in Chapter 2, which verifies the effectiveness of the valve reactor improvement proposed in this paper. The simulation results show that in a certain range, as the controlling bias current increases, the varying range of the magnetic flux density decreases, and the magnetostrictive effect of the iron core decreases. The low-frequency vibration and noise should be reduced accordingly. Besides, the enclosed area which is proportional to the iron loss also decreases. In addition, by adding the controlling DC bias current, the core can be prevented from exiting the saturation region frequently, thereby increasing the valves' switching speed.

3.2 Research on piecewise-linear self-oscillating flux gate large current sensor

Another important application of magnetic saturation technology is fluxgate. Fluxgate is a technique that uses a high-frequency magnetic field to modulate low-frequency or even static magnetic fields when the core is saturated. The magnetic permeability of the core is modulated as the core goes into and out of saturation: unsaturated, the core has the high permeability of soft iron; saturated, it suddenly drops to the low permeability of free space. This means that the flux density *B* in the core due to an external field *H* is also modulated; one can think of the flux due to the external field being switched off as the core saturates, and back on as the core desaturates–hence the name "fluxgate". Clever demodulation schemes allow the magnitude of this gated field to be measured by the sense coil. It was first used in fields such as aerospace and other fields of weak-magnetic detection. The demodulator must be carefully designed to optimise noise, offset, bandwidth and the temperature coefficient. According to the excitation sources, it is divided into traditional fluxgate and self-excited fluxgate.

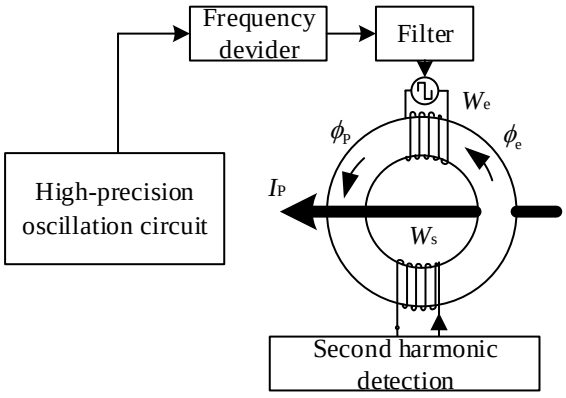

Fig. 3-8 Traditional fluxgate current measurement diagram

The use of traditional fluxgates to achieve highly precise current measurement requires a accurate stable excitation source. As shown in Fig. 3-8, the magnetic flux in the core is superimposed by flux of the measured current Φ_P and the excitation flux Φ_e. When excited with a square-wave signal of a stable frequency $f_1=2\pi/w_1$, the output voltage is detected in the detection winding W_s according to the fluxgate theory [61]:

$$E(t) = 4N_s S\mu_0 w_1 \frac{I_p}{l}\sum_{n=1}^{\infty}\mu_{2n}\sin(2nw_1 t) \tag{3-7}$$

Where μ_0 is the vacuum permeability; N_s is the turns of the detect winding; S is the effective cross-sectional area of the detection winding; I_p is the measuring DC current; l is the effective magnetic circuit length of the core; μ_{2n} is even harmonic amplitude of the spectrum in the Fourier decomposition of the Permeability.

Through spectrum analysis, the amplitude of the second harmonic is much larger than other harmonics. On the other hand, in order to reduce the interference between harmonics, the second harmonic is often detected during the actual detection, so it is also called the second harmonic method. The advantage of this method is its high accuracy and high sensitivity, but its complicated circuit structure and its high-cost limit its use. In this paper, based on the principle of self-oscillating fluxgate, using deep saturation of the core, a novel closed-loop high-current detection scheme is designed, as shown in Fig. 3-9.

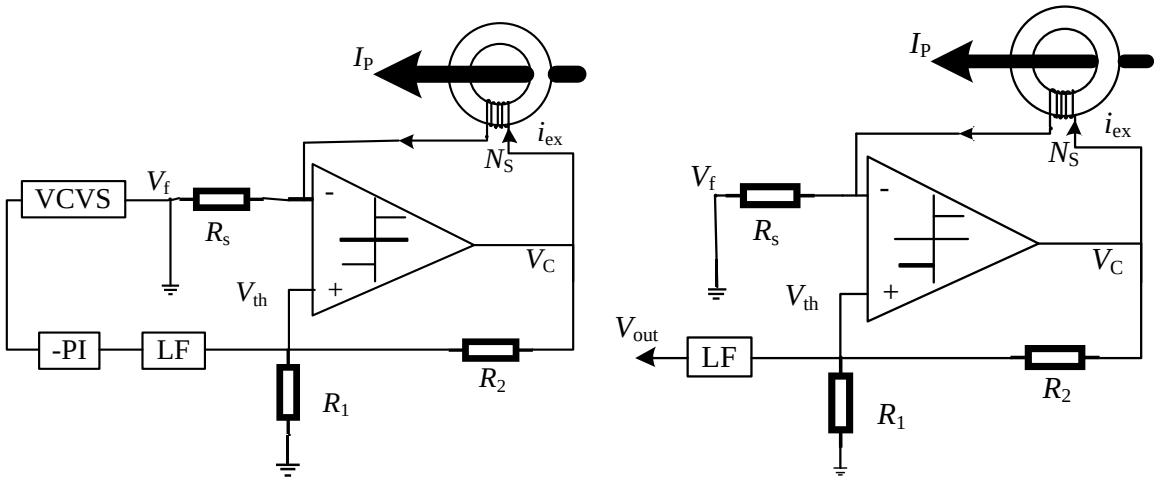

Fig. 3-9 (a)Large DC current close loop detection scheme; (b) open loop detection scheme

3.2.1 Introduction to detection principle

In order to explain the closed-loop principle, this chapter first studies the open-loop structure. If the closed-loop feedback voltage V_f is grounded, as shown in Fig. 3-9(b), the close-loop will become the open-loop structure. In Fig. 3-9(b), the high permeability, low saturation flux core and excitation winding made of amorphous material form a nonlinear inductor. As shown in Fig. 3-10(a), using the piecewise linear model deduced in Chapter 2, the current waveform of self-excited flux gate is shown in Fig. 3-10(b). In Fig. 3-10(b), when the current i_{ex} is in the range of $[I_s^-, I_s^+]$, the nonlinear inductor is unsaturated, the inductance in the non-saturation region is L_0 and is assumed as a constant; I_s is the saturation current, and the corresponding magnetic flux Ψ_s is called saturation flux. When the amplitude of the current i_{ex} exceeds the saturation current I_s, the core gets into saturation, the inductance in the saturation region is L_s, I_{th}^- and I_{th}^+ represent the reverse and the forward maximum excitation current respectively, corresponding to the maximum flux linkage Ψ_s^-, Ψ_s^+; The

maximum excitation current is determined by the threshold voltage V_{th} of the comparator. The comparator outputs a positive and negative square wave. The square wave generates the excitation current i_{ex} in the excitation coil, and the voltage across R_s caused by i_{ex} is the reverse terminal voltage of the comparator. The threshold voltage V_{th}, which is the result of dividing by the comparator output square wave by the resistors R_1 and R_2 , is the non-inverting input of the comparator. In normal operation, there exists: $I_{th}^{+}=-I_{th}^{-}=V_{th}/R_s$, $I_s^{+}=-I_s^{-}=I_s$. In order to ensure deep saturation of the magnetic core is reached, the threshold voltage must satisfy $I_{th}>>I_s$.

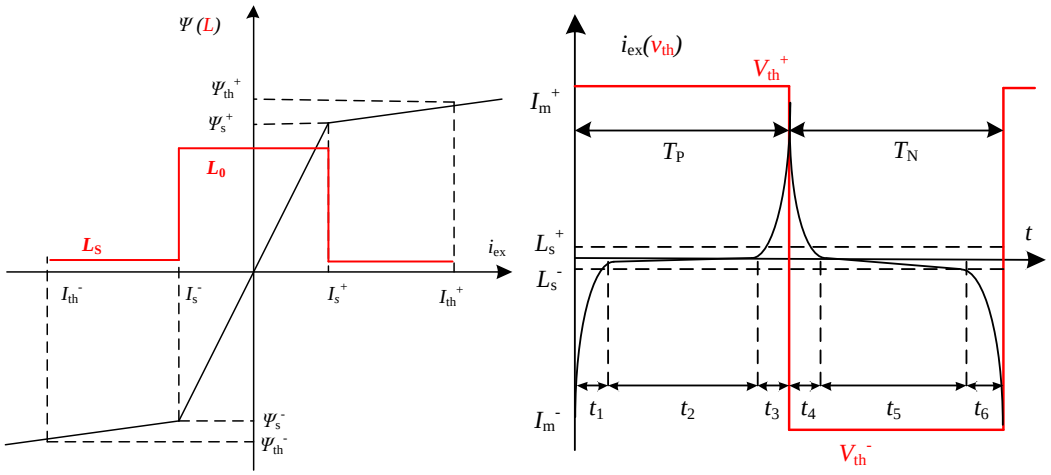

Fig. 3-10 (a)Employed piecewise linear model;(b) voltage and current waveform of the self-excited fluxgate

For ease of understanding of the principle of the self-oscillating fluxgate, we briefly analyzes the oscillation process with reference to Fig. 3-9 and Fig. 3-10. Firstly, assume that the measured current I_p = 0, the comparator output voltage is negative before zero time, i_{ex} just reached the reverse threshold I_{th}^{-}, once i_{ex} continues to increase a bit, the inverse input of the comparator is lower than the non-inverting input voltage, thus the output voltage immediately turns positive. The threshold voltage V_{th} on the comparator's non-inverting input terminal immediately becomes positive, but the excitation current cannot be reversed in step and it can only gradually change from I_{th}^{-} to I_{th}^{+}, as shown in Fig. 3-10(b) in the time periods of t_1, t_2 and t_3.

During the time interval t_1, the iron core gradually goes out of the reverse depth saturation. At this time, the inductance of the coil, noted as L_s, is small, and the current rapidly decreases to L_s^{-}. During t_2, the core is changing from reversed magnetizaiton to forward unsaturated, and the coil inductance is noted as L_0. Due to $L_0>>L_s$, the excitation current changes slowly during the t_2 segment. When i_{ex} exceeds the forward saturation current I_s^{+}, the inductance changes to L_s again. As shown in the t_3 segment waveform, the core rapidly enters positive depth saturation. At the end of t_3, when the excitation current i_{ex} exceeds I_{th}^{+}, the inverting-input of the comparator will be higher than the non-inverting input voltage, the comparator output voltage is immediately inverted to negative, the threshold voltage V_{th} is

immediately changed to V_{th}^-, and the excitation current i_{ex} gradually decreases to zero and increases in the opposite direction. The time interval t_4 is the process when the iron core gradually exits the positive deep saturation while the time interval t_4 is the process that the core goes from the positive saturation through the non-saturation area to the reverse saturation. At the end of the t_6 period, the output of comparator is turned over again. The t_1, t_2, t_3 time intervals constitute the positive half cycle T_P of the self-oscillation, while t_4, t_5, t_6 constitute the negative half cycle T_N of the self-excited oscillation. Since the symmetrical parameters, the positive half cycle should equals to the negative half cycle when I_P=0(T_P= T_N).Assume that the measured current I_P is positive, which direction is defined by I_P in Fig. 3-9. The core is easier to saturate in the positive direction. The positive saturation excitation current becomes I_{s1}^+= I_s^+-I_P/Ns and the reverse saturation current becomes I_{s1}^- = -(I_s+I_P/N_s) due to the presence of I_P, i.e. the positive half cycle decreases while the negative half cycle increases(T_P<T_N). The duty cycle is less than 50%, and the larger the I_P, the greater the difference between the positive and negative half-cycles. Meanwhile, the excitation current required for forward saturation is less than the excitation current required for reverse saturation. The average value of the excitation current i_{ex} over the entire period is linear related to the measuring current I_p. Similarly, it can be obtained that when I_p is negative, T_P>T_N, the duty cycle is greater than 50%, and the average value of the excitation current i_{ex} is positive during the entire cycle. The average current model has proved that there is a linear relationship between the average value of the excitation current i_{ex} and the measured current I_p. In fact, there is also a linear relationship between the duty cycle D of the excitation square wave and the measured current I_p, which is proved in the next section.

It is worth noting that the maximum excitation current I_{th}^+ or I_{th}^- must be greater than the converted value of the measured current I_p, which is determined by the self-oscillating circuit configuration. The self-oscillating circuit structure is actually a bistable circuit. If the above conditions are not satisfied, the bi-stable state will be destroyed and the circuit will not start to oscillate, i.e. the modulation cannot be realized. This is also an important reason for requiring of deep saturation. Setting the maximum excitation current to deep saturation can increase the range of the measuring current.

A square-wave signal with amplitude A and duty cycle D passes through a low-pass filter whose cut-off frequency is much lower than the square-wave's frequency. The effect is equivalent to taking average of the square-wave, ignoring the phase lag, and the output of the low-pass filter is as following:

$$V_{out} = \frac{ADT - A(1-D)T}{T} = A(2D-1) \tag{3-8}$$

Therefore, when the duty cycle of the square wave D=50%, the average output voltage is zero; when D<50%, the average output voltage is negative; when D>50%, the average output voltage is positive. In the self-excited fluxgate, using the low-pass filter to take square wave signal average, the output can get a DC level related to the duty cycle. From the above

analysis, it can be known that there exists a linear relation between the duty cycle D of the excitation square wave and the measuring current I_p. Because of the linear relationship, the low-pass filter output V_{out} in Fig. 3-9(b) is a DC level that is linearly related to I_p. By measuring V_{out}, the direction and magnitude of I_p can be obtained.

3.2.2 Circuital Proof of linear relationship

In Fig. 3-9, the magnetic core operates in a deep saturation state. The hysteresis effect can be neglected. The magnetization curve is represented by the piecewise linear equation in Fig. 3-10(a). That is, the magnetic core inductance only takes L_0 and L_s. L_0 is the inductance when the core is not saturated, while L_s is the saturation inductance of the core, and $L_s << L_0$. Assuming that the comparator is an ideal device, the input impedance at the inverting input terminal and the non-inverting terminal is infinite, i.e. no current flows into the inputs, and the comparator has no inversion delay time. This section starts from circuit theory and demonstrates the linear mathematical relationship between input and output.

In Fig. 3-10(b), during the time period t_1, the KVL equation of the branch where the magnetic core is located is as following:

$$v_{ex} = i_{ex}(t)R_s + L_s\frac{\mathrm{d}i_{ex}(t)}{\mathrm{d}t} = V_c \tag{3-9}$$

Where V_C is the output voltage which is a known constant value.When t=0， there exists $i_{ex}(0)$=-I_{th}, solve the equation(3-9),we get：

$$i_{ex}(t) = -(I_C + I_{th})e^{-\frac{t}{\tau_1}} + I_C \tag{3-10}$$

Where saturation time constant $\tau_1=L_s/R_s$; $I_{th}=V_{th}/R_s$; $I_C=V_C/R_s$. $V_{th}=kV_C$， $k=R_1/(R_1+R_2)$. When $t=t_1$：

$$i_{ex}(t_1) = -(I_C + I_{th})e^{-\frac{t_1}{\tau_1}} + I_C = -(I_s + I_{ps}) \tag{3-11}$$

Where I_{ps} is the equivalent current of the measuring current in the primary excitation winding, and $I_{ps}=I_p/N_s$. Solve the equation(3-10)：

$$t_1 = \tau_1 \ln(\frac{I_c + I_{th}}{I_c + I_s + I_{ps}}) \tag{3-12}$$

During $t\in[t_1,t_2]$, there exists following relationships：

$$v_{ex} = i_{ex}(t)R_s + L_0\frac{\mathrm{d}i_{ex}(t)}{\mathrm{d}t} = V_s \tag{3-13}$$

$$i_{ex}(t_1) = -(I_s + I_{ps}) \tag{3-14}$$

$$i_{ex}(t_1 + t_2) = (I_s - I_{ps}) \tag{3-15}$$

Jointly solve equation (3-13), (3-14)and(3-15), we obtain：

$$i_{ex}(t) = -(I_C + I_S + I_{ps})e^{-\frac{t-t_1}{\tau_2}} + I_C \tag{3-16}$$

$$t_2 = \tau_2 \ln(\frac{I_c + I_s + I_{ps}}{I_c - I_s + I_{ps}}) \tag{3-17}$$

Where unsaturated time constant $\tau_2=L_0/R_s$, obviously, $\tau_{2>>}\tau_1$. During $t\in[t_2, t_3]$, there exists following relationships：

$$v_{ex} = i_{ex}(t)R_s + L_s\frac{\mathrm{d}i_{ex}(t)}{\mathrm{d}t} = V_s \tag{3-18}$$

$$i_{ex}(t_1 + t_2 + t_3) = I_{th} \tag{3-19}$$

Jointly solve equation (3-15), (3-18) and (3-19), we obtain:

$$i_{ex}(t) = -(I_C - I_S + I_{ps})e^{-\frac{t-t_1-t_2}{\tau_1}} + I_C \tag{3-20}$$

$$t_3 = \tau_1 \ln(\frac{I_C - I_s + I_{ps}}{I_C - I_{th}}) \tag{3-21}$$

Similarly, we can get the expressions of t_4，t_5，t_6 and the excitation current equations in each time intervals. In summary, the current and time in one oscillation cycle can be analytically expressed as:

$$i_{ex}(t) = \begin{cases} -(I_C + I_{th})e^{-\frac{t}{\tau_1}} + I_C (0 < t < t_1) \\ -(I_C + I_S + I_{ps})e^{-\frac{t-t_1}{\tau_2}} + I_C (t_1 < t < t_2) \\ -(I_C - I_S + I_{ps})e^{-\frac{t-t_1-t_2}{\tau_1}} + I_C (t_2 < t < t_3) \\ (I_C + I_{th})e^{-\frac{t-t_1-t_2-t_3}{\tau_1}} - I_C (t_3 < t < t_4) \\ (I_C + I_s - I_{ps})e^{-\frac{t-t_1-t_2-t_3-t_4}{\tau_2}} - I_C (t_4 < t < t_5) \\ -(I_C - I_s - I_{ps})e^{-\frac{t-t_1-t_2-t_3-t_4-t_5}{\tau_1}} - I_C (t_5 < t < t_6) \end{cases} \tag{3-22}$$

$$t_n = \begin{cases} \tau_1 \ln(\frac{I_c + I_{th}}{I_c + I_s + I_{ps}}) \quad (n=1) \\ \tau_2 \ln(\frac{I_c + I_s + I_{ps}}{I_c - I_s + I_{ps}}) \quad (n=2) \\ \tau_1 \ln(\frac{I_C - I_s + I_{ps}}{I_c - I_{th}}) \quad (n=3) \\ \tau_1 \ln(\frac{I_c + I_{th}}{I_c + I_s - I_{ps}}) \quad (n=4) \\ \tau_2 \ln(\frac{I_c + I_s - I_{ps}}{I_c - I_s - I_{ps}}) \quad (n=5) \\ \tau_1 \ln(\frac{I_C - I_s - I_{ps}}{I_c - I_{th}}) \quad (n=6) \end{cases} \tag{3-23}$$

The expression of the positive and negative half-cycles obtained by solving equation (3-23) is:

$$T_{\mathrm{P}} = t_1 + t_2 + t_3 = \tau_1 \ln(1 + \frac{2I_{\mathrm{th}}}{I_{\mathrm{c}} - I_{\mathrm{th}}}) + (\tau_2 - \tau_1)\ln(1 + \frac{2I_{\mathrm{s}}}{I_{\mathrm{c}} - I_{\mathrm{s}} + I_{\mathrm{ps}}}) \tag{3-24}$$

$$T_{\mathrm{N}} = t_4 + t_5 + t_6 = \tau_1 \ln(1 + \frac{2I_{th}}{I_{\mathrm{c}} - I_{th}}) + (\tau_2 - \tau_1)\ln(1 + \frac{2I_{s}}{I_{c} - I_{s} - I_{ps}}) \tag{3-25}$$

Comparing the equations (3-24) and (3-25), when I_{ps} is 0, T_{P} and T_{N} are equal, i.e. when the measuring current is null the duty cycle of excitation square wave is equal to 50%; when I_{ps}> 0(the measured current direction is the same as the direction shown by I_{P} in Fig. 3-9), T_{P}<T_{N}, and the duty ratio is less than 50%; viceversa, when I_{ps}> 0, T_{P}> T_{N}, the duty ratio is greater than 50%. The analytical formula is consistent with the introduction of the previous section, which shows the correctness of the mathematical model. Although the exact expressions for the positive and negative half-periods are given, the expression is complex. In fact, due to $\tau_1 << \tau_2$, the equations (3-23) and (3-24) can be simplified as following:

$$T_{\mathrm{P}} = t_1 + t_2 + t_3 \approx \tau_2 \ln(1 + \frac{2I_{\mathrm{s}}}{I_{\mathrm{c}} - I_{\mathrm{s}} + I_{\mathrm{ps}}}) = t_2 \tag{3-26}$$

$$T_{\mathrm{N}} = t_4 + t_5 + t_6 \approx \tau_2 \ln(1 + \frac{2I_{\mathrm{s}}}{I_{\mathrm{c}} - I_{\mathrm{s}} - I_{\mathrm{ps}}}) = t_5 \tag{3-27}$$

From the above approximation, it can be seen that during the positive and negative half cycles, the velocity of the core through the unsaturated zone is much slower than that of the saturated zone. This is also verified in the following experimental waveforms. For the open loop configuration, if the condition:$I_{\mathrm{C}} >> I_{\mathrm{s}}$, $I_{\mathrm{C}} >> I_{\mathrm{ps}}$ are satisfied, equations(3-26), (3-27) can be further simplified as the following(according to the mathematical approach $ln(1+a) \approx a (a << 1)$):

$$T_{\mathrm{P}} = \tau_2 \ln(1 + \frac{2I_{\mathrm{s}}}{I_{\mathrm{c}} - I_{\mathrm{s}} + I_{\mathrm{ps}}}) \approx \tau_2 \frac{2I_{\mathrm{s}}}{I_{\mathrm{c}} - I_{\mathrm{s}} + I_{\mathrm{ps}}} \tag{3-28}$$

$$T_{\mathrm{N}} = \tau_2 \ln(1 + \frac{2I_{\mathrm{s}}}{I_{\mathrm{c}} - I_{\mathrm{s}} - I_{\mathrm{ps}}}) \approx \tau_2 \frac{2I_{\mathrm{s}}}{I_{\mathrm{c}} - I_{\mathrm{s}} - I_{\mathrm{ps}}} \tag{3-29}$$

So the duty cycle of the excitation square wave is：

$$D = \frac{T_{\mathrm{P}}}{T_{\mathrm{P}} + T_{\mathrm{N}}} = -\frac{1}{2(I_{\mathrm{c}} - I_{\mathrm{s}})} I_{\mathrm{ps}} + \frac{1}{2} \tag{3-30}$$

Referring to equation (3-7), the open-loop output voltage can be obtained:

$$V_{\mathrm{o}} = A(2D - 1) = -\frac{kV_{\mathrm{C}}}{(I_{\mathrm{c}} - I_{\mathrm{s}})} I_{\mathrm{ps}} \tag{3-31}$$

Where k is the ratio of the devider resistance R_1 and resistance R_2 in Fig. 3-9. As $I_C=V_C/R_s$, the equation (3-31) can be expressed as：

$$V_o = -\frac{kR_sV_C}{(V_C - I_sR_s)N_s} I_P \tag{3-32}$$

Equation (3-32) shows a linear relationship between the open-loop output voltage V_o and the measured current I_p. The above has deduced the open-loop linear relationship. For closed-loop configuration, the only difference is that the excitation branch is no longer directly grounded but is connected to a feedback voltage V_f. As shown in Fig. 3-11, the excitation voltage is changed from the symmetrical comparator output voltage $\pm V_C$ to V_C-V_f and -(V_C+V_f), similar to the previous deduce, the time intervals t_1~t_6 for close-loop and their related current expressions can be obtained. In fact, compared with the open-loop expression, the closed-loop only needs to replace the I_C in the positive half cycle with I_C-V_f/R_s and the negative half cycle with I_C+V_f/R_s.

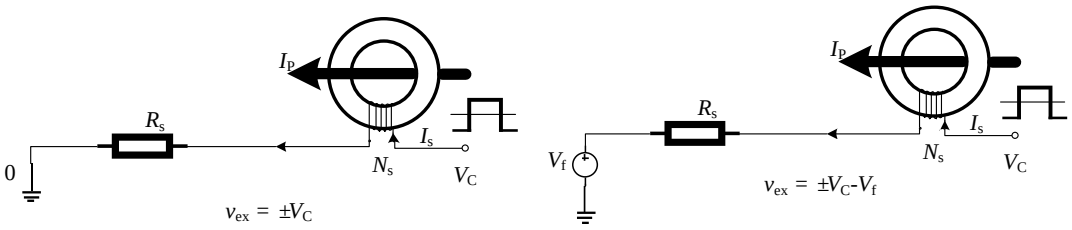

Fig. 3-11 (a) Open-loop excitation branch. (b) Closed-loop excitation branch

For the closed-loop case, the expression of the positive and negative half cycles are as follows:

$$T_P = \tau_2 \ln(1 + \frac{2I_s}{I_c - \frac{V_f}{R_s} - I_s + I_{ps}}) \tag{3-33}$$

$$T_N = \tau_2 \ln(1 + \frac{2I_s}{I_c + \frac{V_f}{R_s} - I_s - I_{ps}}) \tag{3-34}$$

In the above equations, if V_f meets:

$$V_f = R_sI_{ps} = \frac{R_s}{N_s} I_P \tag{3-35}$$

Even in the presence of the measuring current I_p, the positive and negative half cycles of the excitation voltage are still equal. When the duty cycle deviates from 50%, the low-pass filter outputs a DC level shown in the equation (3-31), which is adjusted by the reverse PI controller, and finally reaches the equilibrium state in equation (3-35). Therefore, equation (3-35) is an ideal linear relationship of a self-oscillating fluxgate current sensor.

3.2.3 Analysis of the main static indicators of the sensor

1) Sensitivity and resolution

By taking the derivative of the theoretical linear relationship equation (3-35), the theoretical sensitivity is obtained:

$$S = \frac{\mathrm{d}U_{\mathrm{o}}}{\mathrm{d}I_{\mathrm{p}}} = \frac{R_{\mathrm{s}}}{N_{\mathrm{s}}} \tag{3-36}$$

However, the theoretical sensitivity is actually lower than the actual value. There are two main reasons for this deviation: Firstly, in the theoretical derivation of the theoretical sensitivity, the coil is considered as a nonlinear inductor without resistance. In fact, according to the difference in the number of turns, windings made of copper wire generally have a different winding resistance R_{w} ranging from several ohms to several tens of ohms. When deducing the ideal theoretical sensitivity, R_{w} is neglected. However, when the value of the sampling resistor R_{s} is considerable related to R_{w}, this approximation is equivalent to taking a smaller R_{s} than the true value, thus, it will cause the theoretical sensitivity is lower than the actual sensitivity. And the smaller the value of R_{s}, the larger the deviation due to this approximation. Secondly, the parasitic capacitance shunts a small part of the bypass excitation current. In the derivation above, the comparator's inverting input is used as the ideal op amp with infinite input resistance, i.e. the current can only pass through R_{s}. However, in practice, due to the existence of parasitic capacitance, a small part of the excitation current and compensation current flow into the ground loop through the parasitic capacitance, and due to the blocking effect of the capacitor, the measuring DC equivalent current I_{ps} can not flow into this shunt loop like the excitation current. After considering the above two aspects, Equations (3-33) and (3-34) are revised to:

$$T_{\mathrm{P}} = \tau_2 \ln\left(1 + \frac{2kI_{\mathrm{s}}}{kI_{\mathrm{c}} - k\frac{V_{\mathrm{f}}}{R_{\mathrm{s}}+R_{\mathrm{w}}} - kI_{\mathrm{s}} + I_{\mathrm{ps}}}\right) \tag{3-37}$$

$$T_{\mathrm{N}} = \tau_2 \ln\left(1 + \frac{2kI_{\mathrm{s}}}{kI_{\mathrm{c}} + k\frac{V_{\mathrm{f}}}{R_{\mathrm{s}}+R_{\mathrm{w}}} - kI_{\mathrm{s}} - I_{\mathrm{ps}}}\right) \tag{3-38}$$

Where k is the introduced current correction factor, $k \leqslant 1$, it represents part of the current that is dissipated by parasitic capacitance. If k=1, it means the shunt current is neglected. R_{w} is the resistance of the winding.

From equation (3-37) and equation (3-38), the corrected linear relationship can be derived as follows:

$$V_{\mathrm{f}} = \frac{R_{\mathrm{s}} + R_{\mathrm{w}}}{k} I_{\mathrm{ps}} = \frac{R_{\mathrm{s}} + R_{\mathrm{w}}}{kN_{\mathrm{s}}} I_{\mathrm{p}} \tag{3-39}$$

The corrected proportional coefficient derived from above also shows that the linear

relationship between input and output still holds. In equation(3-39) , the value of the current correction coefficient *k* depends on the specific circuit parameters, and it can be calibrated by the specific experiment. The expression for the actual sensitivity after correction can be obtained by taking derivative of the equation (3-39):

$$S_1 = \frac{dV_f}{dI_P} = \frac{R_s + R_w}{kN_s} \tag{3-40}$$

From equation (3-40), it shows that the larger the number of winding turns N_s and the smaller R_s is, the lower the sensitivity is. Despite increasing R_s and decreasing N_s can improve the sensitivity, but the value of N_s and R_s also affects the linearity and range at the same time, so compromision should be made in the decision of N_s and R_s.

Resolution is the ability of the measurement system to detect and faithfully indicate small changes in the characteristic of the measurement result. Assuming the minimum effective change in sensor output is ΔU, the resolution can be expressed as the ratio of the smallest change in sensor output to the sensitivity:

$$r = \frac{\Delta U}{S} \tag{3-41}$$

From above, it is easy to know that the resolution and the sensitivity are positively correlated. Increasing the sensitivity can improve the resolution. When other factors are not considered, the larger the sampling resistance R_s is, the higher the resolution is.

2) Linearity influencing factors

In fact, the linear relationship between the output voltage U_o and the measured current I_p is based on the simplified assumptions. If there is a nonlinear error in the experiment, it is not only related to the core circuit and measurement method, but also to the rationality of simplifying assumptions. The following section analyzes the simplified conditions and analyzes the influence of the assumptions on linearity.

In the derivation of 3.2.2, there are two important simplification conditions: one is $\tau_{2>>}\tau_1$, and the other is $I_c>>I_s$, $I_c>>I_{ps}$. The first condition requires that the iron core must enter deep saturation. Increasing the value of V_{th} can increase the saturation depth. Unlike conventional self-oscillating fluxgates, in the subsequent experiments, the voltage divider ratio is raised to 1:1 to saturate the core. In order to satisfy the second simplification condition, the main measure is to increase the I_c while reducing the saturation current I_s and the measured equivalent current I_{ps}. Decreasing R_s can increase I_c, however, if R_s is too small, it will deteriorate the sensitivity. Reducing the magnetic circuit length l_e and saturation magnetic induction B_s can reduce the saturation current I_s, which is the reason why the core prototype uses cobalt-based amorphous alloys with B_s=0.55T to construct a small toroidal ring. Increasing the number of turns of the exciting winding N_s can reduce the excitation saturation current I_s and the measuring equivalent current I_{ps}, but the inter-turn capacitance

will increase, which needs to be selected after comprehensive consideration.

In addition, there is another factor that will have a large effect on linearity. In the previous section, the comparator only considered the ideal characteristics. The flip is considered to be completed immediately. In fact, due to the limitation of physical imperfection, a short delay exists. Besides, the forward and backward flip delay times are often not equal. For example, when the reverse voltage $i_{ex}R_s$ rises gradually and approaches the non-inverting voltage V_{th}, it is considered that once there exists $i_{ex}R_s > V_{th}$, the comparator output voltage will be immediately flipped from $-V_C$ to $+V_C$. In fact, due to the non-ideal nature of the device, after the $i_{ex}R_s > V_{th}$ condition is satisfied, the flip will occur after a fixed delay, and the delay of the flip from $-V_C$ to $+V_C$ and from $-V_C$ to $+V_C$ is often not equal, this kind of inequality will influence the duty cycle of the square wave, thus result in the the linearity drop. The solution to this interference factor is to use a high-speed op amp, or to reduce the operating frequency of the self-oscillating circuit.

3) Measurement range

According to the expression of equation (3-23) at different time periods, the value of I_p must ensure that all logarithmic expressions are non-negtive, so the following linear region estimation is obtained:

$$-I_C + I_S < \frac{I_P}{N_S} < I_C - I_S \tag{3-42}$$

Where $I_C=V_C/R_s$, indicates the converted current of the output excitation voltage V_C output; I_S is the saturation current of the core; N_s is the number of turns. From equation (3-41), the following conclusion can be drawn: The proposed self-oscillating fluxgate large current detection sensor's range is related to the current sampling resistance R_s and N_s. The smaller R_s is, the larger N_s is, the larger the range is, and the actual values is a trade-off between sensitivity and linearity.

From the discussion and analysis in this section, it can be seen that the number of N_s and the current sampling resistance R_s have an effect on the sensor sensitivity, linearity, mearing range, and resolution. The impact relationship is listed in Table. 3-1. The selection of N_s and R_s needs to be taking account the performance index requirements.

Table. 3-1 the Influence of number of turns N_s and current sampling resistor R_s on sensor performance

parameters	Sensitivity S	Linearity ε	Measurement Range	Resolution r
$N_s\uparrow$	↓	↑	↑	↑
$R_s\uparrow$	↑	↓	↓	↓

3.2.4 Principle Simulation

Multisim integrates industry-standard SPICE simulation with an interactive schematic environment to instantly visualize and analyze electronic circuit behavior. Its intuitive interface helps educators reinforce circuit theory and improve retention of theory throughout engineering curriculum. Produced by National Instruments (NI), Multisim has refined the complexities of SPICE simulation so that engineers can quickly capture, simulate, and analyze new designs without having to understand in-depth SPICE technology. In this section, firstly build the piecewise linear modeling of magnetic core in the Multisim environment, and then use its model to realize the circuit simulation of self-oscillating fluxgate large current sensor.

In multisim, use two parallel inductors and two voltage-controlled voltage switches(VCVS) to construct the piecewise-linear model of the nonlinear inductor in Fig. 3-10(a). Take the voltage of the segment point on the piecewise-linear as the switching voltage of the VCVS. As shown in Fig. 3-12, L_2 represents the unsaturated inductance, L_1 represents the saturated inductance and $L_1 << L_2$. After the current exceeds the saturation current I_S, a low inductance is exhibited externally, otherwise shows a large inductance.

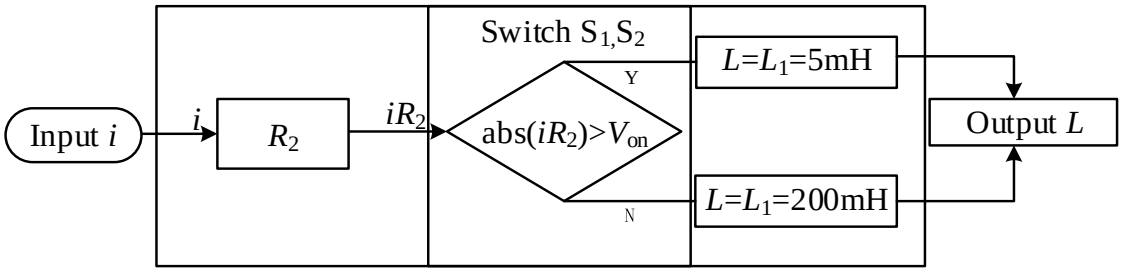

Fig. 3-12 Piecewise linear nonlinear inductor Simulink Schematic

In the simulation circuit of Fig. 3-13, when L_1 is connected to the circuit, L_1 and L_2 are connected in parallel, the inductance value is approximately equal to L_1, it represents the saturation state. When open the L_1 and L_2 acts alone, the large inductance L_2 represents the non-saturation state. The switch S_1 is a voltage-controlled switch, when the control voltage exceeds the on-state voltage V_{on}, the switch is turning on. And the voltage drop across the resistor R_2 is used as the control voltage. In fact, the voltage across resistor R_2 reflects the exciting current i_{ex} of the comparator flowing through the circuit. Therefore, the nonlinear piecewise linear effect is achieved: When i_{ex} exceeds V_{on}/R_2, the inductance decreases from L_2 to L_1. In Fig. 3-13, the control voltage of switch S_2 is opposite to that of S_1. It means that when the amplitude of reverse i_{ex} exceeds V_{on}/R_2, S2 is turning on, L_1 is connected to the circuit, and the inductance is decreased from L_2 to L_1, i.e. the reverse saturation is reached. In the simulation, when the DC measuring current is absent, $I_s^+ = I_s^-$, the positive and negative saturation currents are symmetrical. Set the on-state voltages of S_1 and S_2 all to V_{on}=1.5 V.

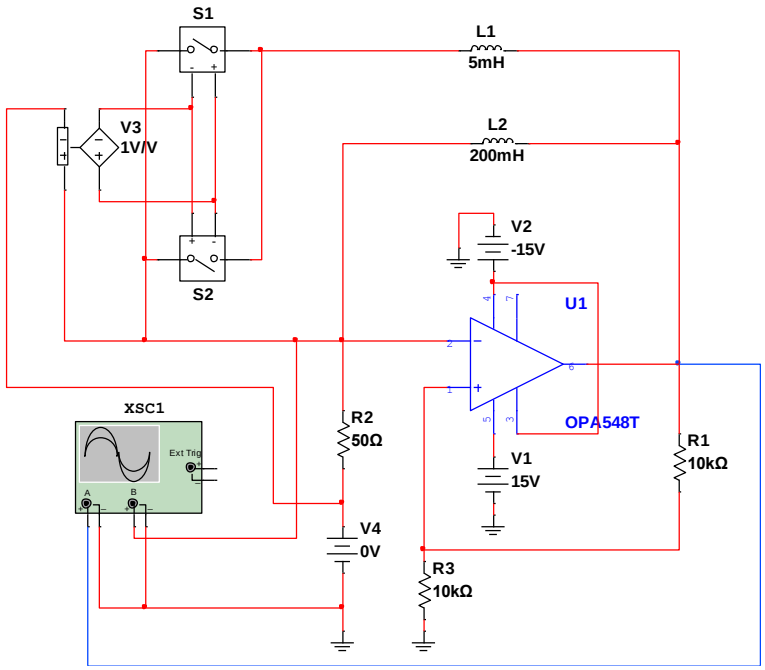

Fig. 3-13 Multisim Simulation circuit

In the simulation, the operational amplifier adopts the Multisim model of the op amp OPA548 used in the actual circuit. The output current of this amp can reach 5A, which can avoid waveform distortion caused by lack of drive capability. The op amp adopts ±15V power supply, and the voltage divider resistors R_1 and R_3 both take the value of 10k which means the ratio of 1:1. According to the simulation circuit parameters, there are: $I_s=V_{on}/R_2$=1.5V/5 Ω =30mA, $I_{th}=V_{th}/R_2$=7.5V/50Ω=150mA, $I_c=2I_{th}$=300mA. Those parameters basically meet the previous $I_c>>I_s$ hypothesis. Observe the voltage on R_2 and the excitation voltage V_c with an oscilloscope. The simulation waveform is shown as Fig. 3-14.

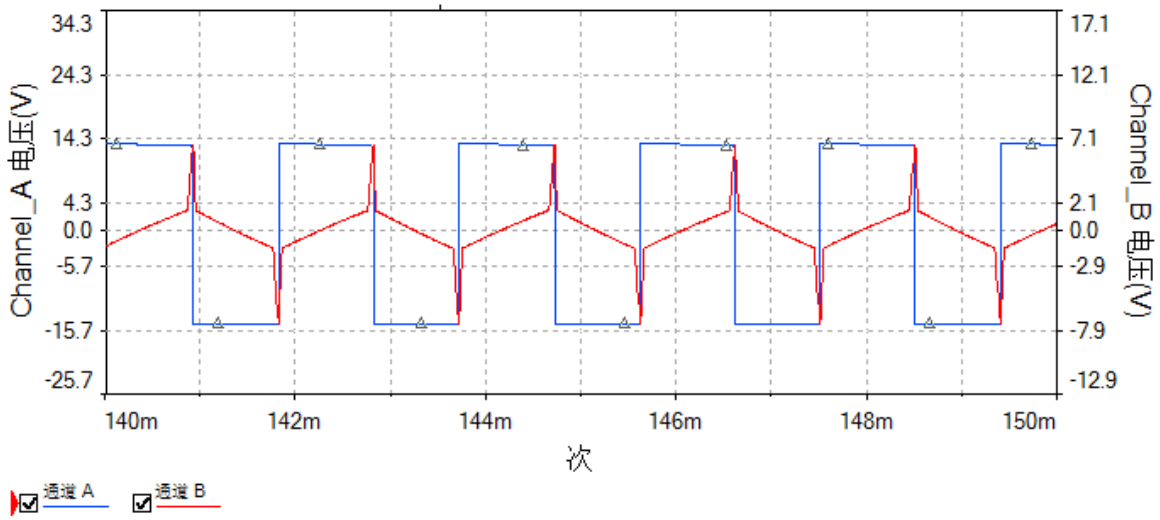

Fig. 3-14 Simulated waveforms when measured current I_p=0

Analyze the waveform, firstly, the simulation waveform in Fig. 3-14 is consistent with the

waveform in the principle analysis in Fig. 3-10(b). When the measured current is null, the current waveform is symmetrical, and the duty cycle of the excitation waveform is 50%. According to formula (3-20), the value of t_1~t_6 can be calculated. The theoretical calculation value and simulation value are shown in Table. 3-2.

Table. 3-2 Comparison of theoretical and simulated values

time(us)	t_1	t_2	t_3	T_P	t_4	t_5	t_6	T_N
theoretical	31	803	59	893	31	803	59	893
simulated	44	820	50	914	44	820	62	926
Related error(%)	41.94%	2%	15.25%	2.3%	41.94%	2%	5.08%	3.70%

It can be seen from Table. 3-2 that for both the calculated value and the simulated value, during the positive and negative half cycles, the unsaturation times t_2 and t_5 are much larger than the saturation times t_1, t_3, t_4 and t_6, which verifies the rationality of the approximation in equation (3- 27) and (3-28); meanwhile, there is a large deviation between simulation and theoretical calculations, especially for saturation times t_1, t_3, t_4 and t_6, where the difference between simulation and calculation reaches 40%. The main cause is the practical imperfection of OPA548 used in the simulation, it is easy to observe from the waveform of Fig. 3-14 that the output of OPA548 does not reach ±15V, the actual excitation voltage V_C is less than 15V.

Consider the measured current I_p is positive(the same direction as the arrow points of I_p in Fig. 3-9). According to the study in Section 3.2.1, the forward saturation excitation current becomes $I_{s1}^+ = I_s^+ - I_p/N_s$, and the reverse saturation current swifts to $I_{s1}^- = -(I_s + I_p/N_s)$. In the simulation circuit in Multisim, it can be realized by setting V_{on} of the switch S_1 and S_2 differently, for example, setting V_{on1} of S_1=0.01V and setting V_{on2} of S_2 to 3 V, which implies the case of I_p=+6A (I_{ps}= +30mA) . The simulation result is shown in Fig. 3-15, the saturation in the positive half cycle is advanced and in the negative half cycle is delayed due to the effect of I_p, so T_P<T_N, the duty cycle is less than 50%. The current waveform is no longer symmetry respect to time axis, the mean value of the current becomes negative, which is consistent with the previous theoretical derivation. According to equation (3-31), when I_{ps}=+30mA, the duty cycle D=44.5%. The simulation result is: D_1=849μs/(849μs+975 μs)=46.57%. The reason for the difference between the simulation results and the calculated values is still that the simulation value of I_c is less than the calculated value. By changing the turn-on voltage V_{on} of S_1 and S_2, it is possible to simulate the influence of the measuring current to the open-loop self-excited fluxgate, thus verifying that the effect of the measuring current will cause the variation of the duty cycle in the excitation square wave.

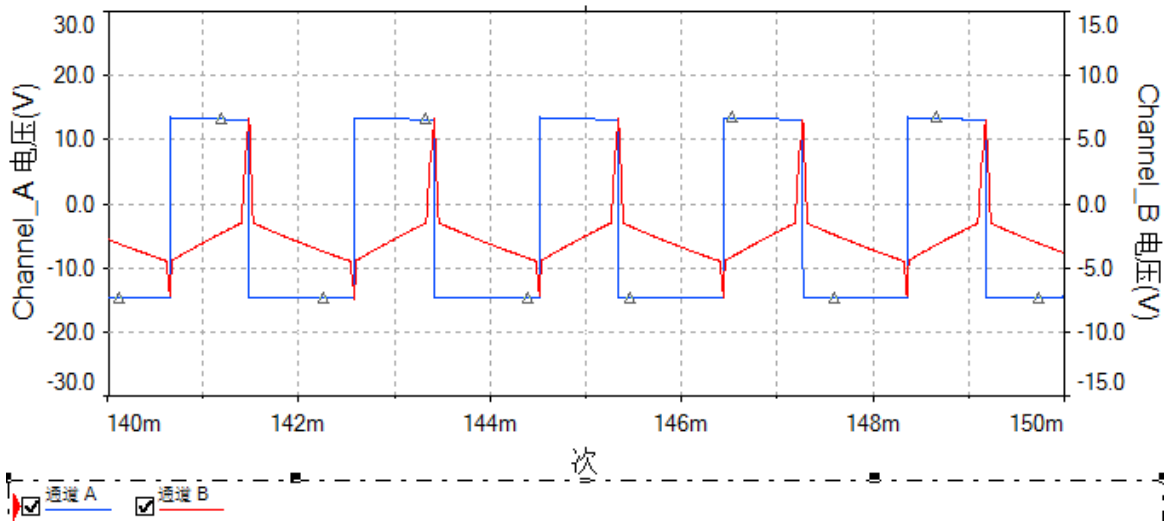

Fig. 3-15 Simulated waveforms when measured current I_p=6A

Then use the simulation to verify the effect of V_f. In the simulation circuit diagram shown in Fig. 3-13, a voltage source V_4 is added to the excitation branch to represent the feedback voltage V_f. According to equations (3-32) and (3-33), when V_f exists, even if the measured current is zero, the asymmetry of the excitation voltage will occur. Set V_f to 1.5V(V_f = 1.5V). The simulation results are shown in Fig. 3-16, the current waveform is shifted upward, and the duty cycle is greater than 50%, which is the same as the waveform when the measuring current I_p is negative. Therefore, when I_p is positive(the duty cycle is less than 50%), by adding a proper positive V_f, the duty cycle can still be maintained at 50% (T_P=T_N). In another word, the change of the duty cycle caused by the measured current I_p can be offset by a reasonable V_f setting.

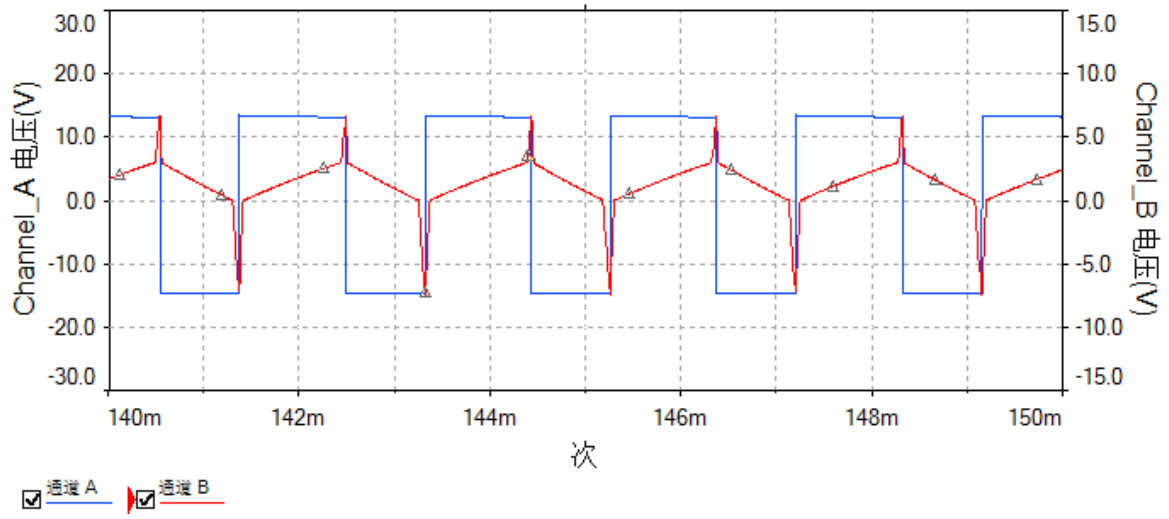

Fig. 3-16 Simulated waveforms when I_p=0， V_f=1.5 V

In Fig. 3-17, it shows the waveforms when I_p and V_f exist at the same time. By manually adjusting I_p and V_f, we find that as long as V_f satisfies: V_f=R_sI_{ps}(V_f=R_sI_p/N_s), the waveform

will become symmetrical again. This is consistent with the equation (3-34) discussed in the previous section, which means that the duty cycle can be kept at 50% by the closed-loop control voltage V_f. Through the above principle simulation, the effectiveness of self-oscillating fluxgate and compensation method is verified.

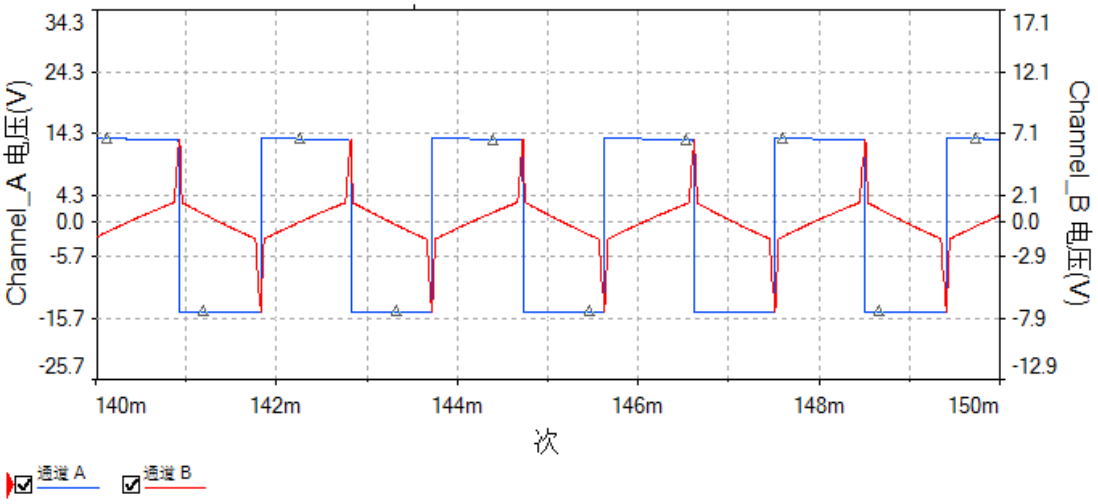

Fig. 3-17 Simulated waveforms whenI_p= + 6A， V_f =1.5 V

3.3 Chapter summary

In this chapter, firstly, based on the Jiles-Atherton magnetic model deduced in the last chapter, the principle of the magnetic controllable valve reactor is described—by adding magnetic controlling bias winding to make the valve reactor work in the saturation region. It can avoid the large magnetic flux density change in the iron core during operation, and then reduce the hysteresis loss and the geometry deformation caused by Magnetostrictive effect. The ultimate goal is to achieve a reduction of the valve reactors's heating and reduce noise and vibration effects. Then, a new scheme of large DC current measurement using magnetic saturation technology was proposed. The principle of detection was analyzed and the linear relationship was deduced in this chapter. Finally, the principle simulation was performed.

4 Experimental performance study

4.1 Controllable valve reactor experimence

The dimension diagram of a 5 kA valve reactor is shown in Fig. 4-1. For the complex structure of the practical reactor and the leakage magnetic field, to verify the validity of the improved scheme proposed in the previous section, no leakage magnetic field research is involved. In the geometric modeling of this reactor, only consider the simple structure of the core and the coil.

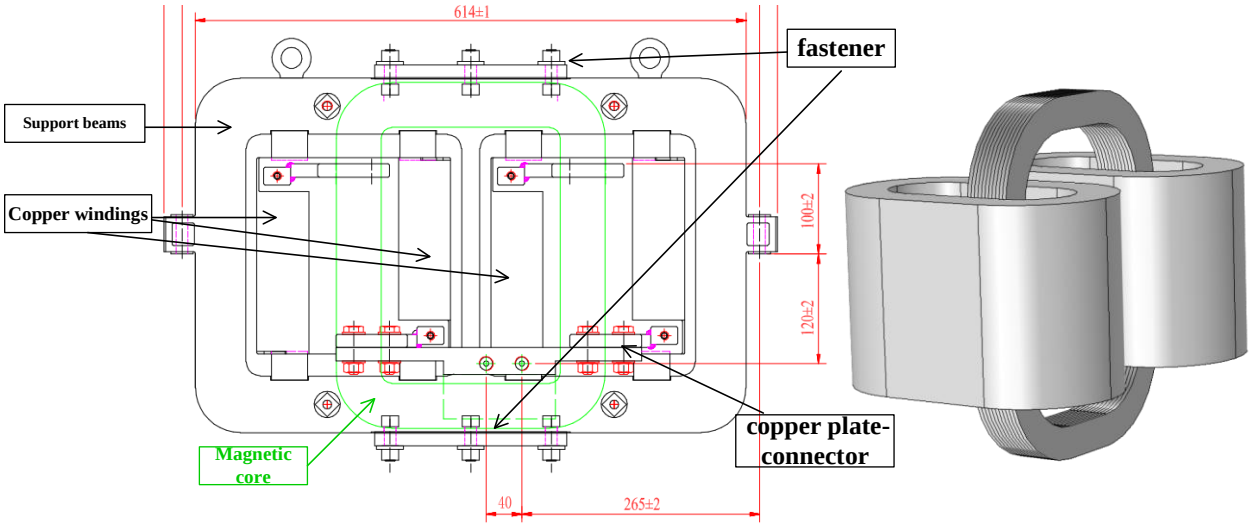

Fig. 4-1 valve reactor schematic and its simplified diagram

Reduce the cores and coils by scale to make a prototype model. As shown in Fig. 4-2, in the reactor prototype, the core still adopts the strip laminated structure, and original reactor windings are replaced by a single winding(the left winding) and the winding on the right is used for magnetic bias control.

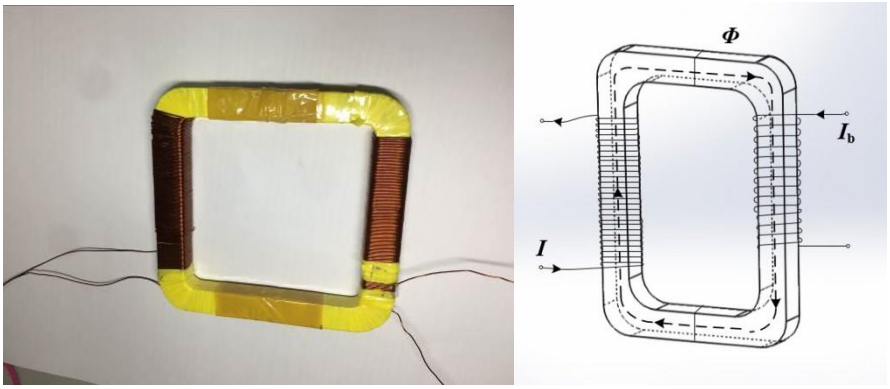

Fig. 4-2 Improved valve reactor prototype and schematic

As shown in Fig. 4-3, the experimental circuit is designed according to the simulation circuit

diagram in Fig. 3-6. The pulse sequence is realized by a DC voltage source plus a MOSFET switch controlled by a square wave generator. R_s is a small sample resistance of 10 ohms, which converts the current into a voltage value and displayed on an oscilloscope. When the MOSFET is switched off, through the freewheeling diode *D*, the operating current *I* decreases from the maximum value to zero. After adding the control winding, the reactor is actually converted into a transformer. To prevent the influence of the primary side on the secondary controlling side's current, the secondary side uses a KA7809 chip to build a constant current source circuit.

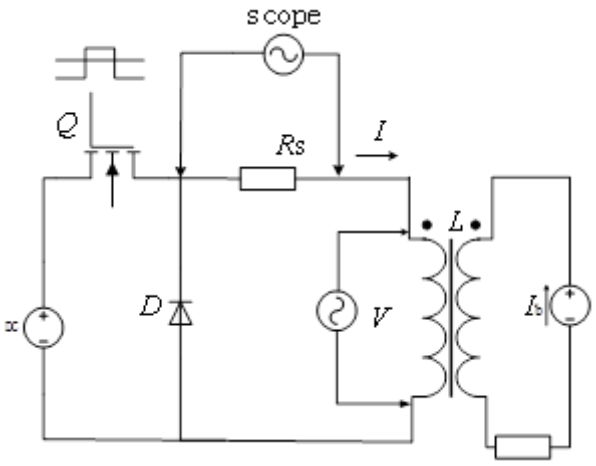

Fig. 4-3 Magnetic saturation valve reactor experimental verification circuit

4.1.1 Switching Rate Comparison

In order to effectively protect the thyristor against inrush current damage, the value of the valve reactor has been left with a large margin in design, but the valve reactor frequently enters and exits the non-saturation zone during operation, so that the actual current rise time is far greater than the design value. Reducing the current rise time of the valve reactor in the safe margin can increase the switching rate of the valve. In the experimental circuit shown in Fig. 4-3, we keep DC at 10 V, change the applied bias current I_b, and study the current rise time of the reactor under different magnetic saturation.

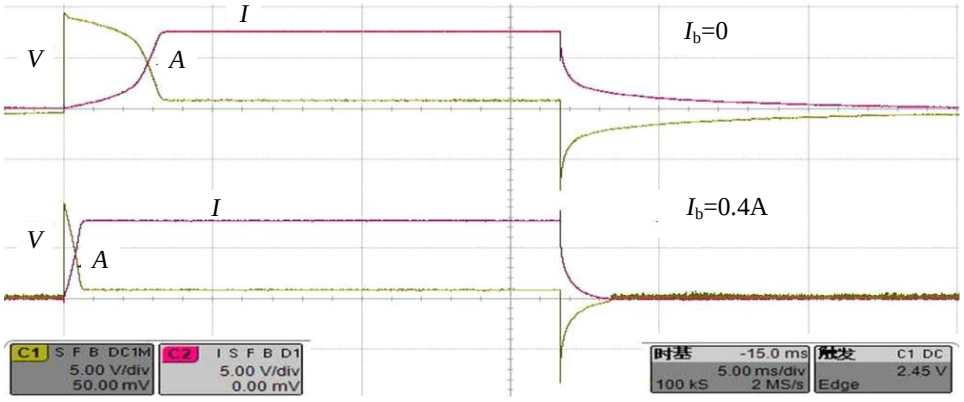

Fig. 4-4 Current rising time waveforms with I_b=0 and I_b=0.4A

Fig. 4-4 shows the comparison in the voltage and current waveforms of the reactor prototype with bias current I_b=0 and I_b=0.4A. From Fig. 4-4, we can find that the current rise time is significantly reduced by DC bias. The point A is the intersection point of voltage and current. It is obvious that the current of point A is exactly 1/2 of the maximum current value. For accurate reading, take the time interval from zero to point A as the rising time. Fig. 4-5 shows the rising time $t_{0.5r}$ under different bias currents. As the applied bias current increases, the current saturation time, as well as its changing rate, becomes smaller; When fully saturated, the current saturation time basically does not change, and the controlling effect of the bias current fails. The results in Fig. 4-5 show that the current saturation time can be controlled by the bias current. In the safe margin of the thyristor's limit, the limitation of the switching rate to the converter valve by the saturator reactor can be reduced by increasing the bias current.

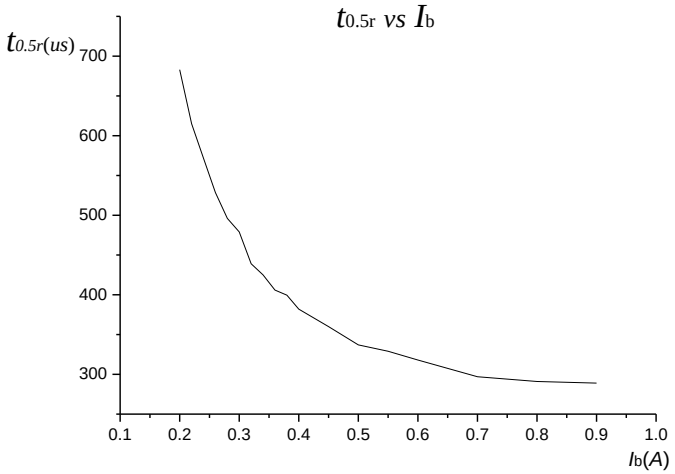

Fig. 4-5 Current rise time *vs* bias current I_b diagram

4.1.2 Working *B-H* curve verification

The current and voltage values measured with an oscilloscope are processed, and the magnetic field strength H is calculated using the current I according to the Ampere loop theorem. According to Faraday's electromagnetic induction theorem:

$$e = -\frac{d\psi}{dt} = -NS\frac{dB}{dt} \tag{4-1}$$

The magnetic induction intensity B can be obtained by integrating the voltage across L, and the integral constant term is determined according to the saturation magnetic induction intensity. The measured working curve without DC bias and with 0.4 A bias current is shown in Fig. 4-6. It is consistent with the conjecture in Fig. 3-3 and the simulation results in Fig. 3-7, the effect of the DC bias current on the working state of the core is as expected.

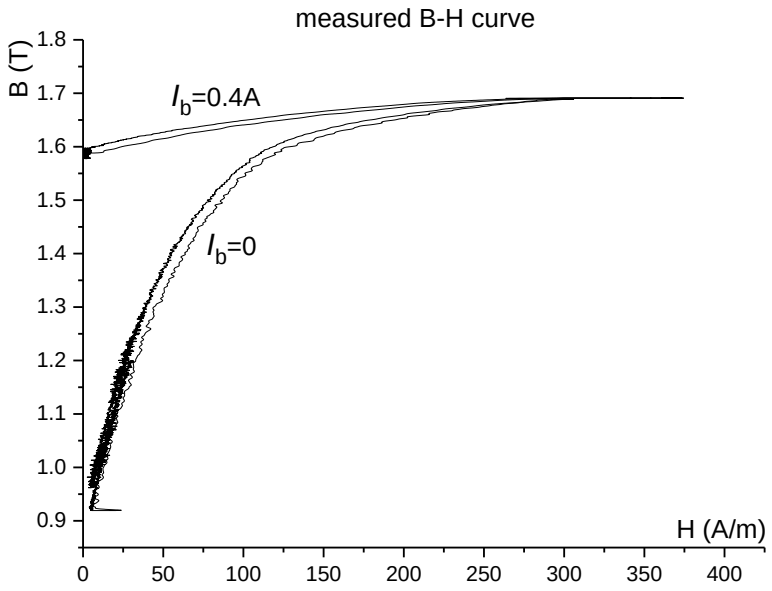

Fig. 4-6 Experimentally measured B-H curve

4.2 Large DC current measurment prototype experiment

4.2.1 Design of the prototype and experimental circuit

1) Nonlinear cores and windings

To complete the desired DC current detection, the magnetic core must work in a deep saturation state. The choice of magnetic core material and structure has a great influence on the detection performance. The design of the magnetic core should meet the following requirements:

(1) The material of the magnetic core should be a soft magnetic material with a high magnetic permeability, since the magnetic permeability is large, the magnetic core can be better magnetized, and it can achive a better magnetic concentrating effect. In the installation, the distance between the core and the windings can be appropriately increased to provide a larger margin for the insulation; on the other hand, the greater the magnetic permeability of the core is, the easier it is to enter saturation under the same external magnetic field strength *H*, thus it can power from the excitation circuit.

(2) The core should have a hysteresis loop that is as narrow as possible to keep hysteresis loop area small and the coercive force low. With a more narrow hysteresis loop, we can achive higher the accuracy of the piecewise linear model and higher linearity of the corresponding sensor.

(3)The core should have low magnetostriction characteristics, high withstanding temperature and low losses. As the magnetic cores work in deep saturation, and magnetostrictive effects can have a detrimental effect on measurement stability.

Table. 4-1 The comparison among the common soft material

material	Cobalt-based amorphous	Ferrite	Permalloy
composion	CoNiFeSiB	$(MnO)_{25}(ZnO)_{22.5}(FeO_3)_{52.5}$	$Ni_{79}Mo_{46}$
Saturation magnetostriction coefficientλs	≈0	$1x10^{-6}$~$2x10^{-6}$	60 ~$100x10^{-6}$
Saturated magnetic flux density Bs(T)	0.55	＜0.48	0.79
Initial permeability μ_i	≥80000	10~10000	37.5~125
Coercivity Hc(A/m)	＜2.2	5~60	0.56
Core loss P(w/kg)	＜35	140	745
Maximum operating temperature (℃)	250	＜120	110

The properties of commonly used soft magnetic materials are given in Table. 4-1. Based on the above principles, amorphous alloys were ultimately selected in this paper. For metal materials, it is usually crystal. However, if the solidification rate of the metal or metal is changed, i.e. the cooling rate from the liquid to the solid is up to one million degrees per second, a glass-like amorphous alloy in which the arrangement of atoms is disordered can be obtained. This amorphous alloy has many unique properties. For example, the cobalt-based amorphous material (Grade No.: CoNiFeSiB 2714A) selected in this paper has high magnetic permeability, low coercive force, extremely low core loss and close to zero magnetostriction coefficient. It is insensitive to mechanical stress, and can be exposed to the extreme environment for long-term. The thickness of the strip is very thin, only 27μm, which is about one-tenth of the thickness of the silicon steel sheet, so it can be curled like paper, which is especially suitable for military product applications. Table. 4-1 gives a comparison of cobalt-based amorphous materials and the commonly used ferrite and permalloy parameters. The null magnetostriction, the extremely low core loss, and the high magnetic permeability are the reasons why we choose the cobalt-based amorphous. The core Uses a cobalt-based amorphous strip with a width of 12.5 mm and a thickness of 30 μm. As shown in Fig. 4-7, the core geometry is given.

Although this design is closed-loop structure, but only one single winding is used, the complexity of the cores and windings is greatly simplified. The volume is compressed, laying the foundation for future miniaturization. For the selection of the number of winding turns N_s, the selection needs to be taken the current measurement range and the stability into account. According to equation (3-30), the larger the N_s, the larger the current measurement range under the same excitation conditions. However, an increase in N_s will cause an increase in the inter-turn distribution capacitance, which will affect the stability of the self-excited circuit. N_s should also satisfy the constrain of excitation saturation current I_s.

According to the equation $I_s = \frac{B_s l_e}{\mu_0 \mu_m N_s}$, the N_{1s} value can be calculated. Considering the constrain: $I_{th} >> I_s$, the value of N_s should be greater than N_{1s}. In this paper, the number of turns is selected as N_s=200, and the enameled wire with a diameter of 0.5 mm is evenly wound on the magnetic core in two layers.

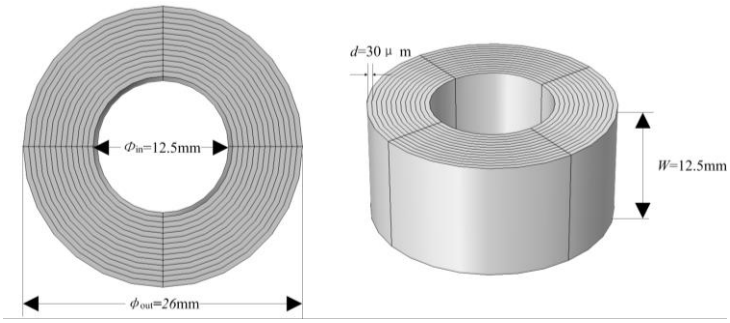

Fig. 4-7 Iron core dimensioning diagram

2) Low-pass filter design

Finally, A low-pass filter is used to demodulate the square wave and get the average value. The average value circuit only needs to output a DC voltage level. Except for the cut-off frequency and delay, there are no more strict requirements for other parameters of the low-pass filter, thus it relax the requirement of the design. As shown in Fig. 4-8, the second-order Sallen-key low pass is used in this paper. The parameters of the filters is listed in Table. 4-2.

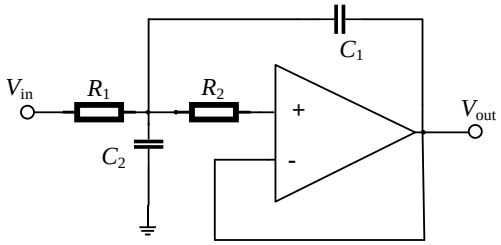

Fig. 4-8 Second-order Sallen-Key low-pass filter circuit diagram

Table. 4-2 Low-pass filter parameters

parameters	values	parameters	values
R1	145k	Transfer FunctionG(s)	$\frac{4921.1872}{s^2+38.4837s+4921.1872}$
R2	637k	Cut-off frequency (fc)	11.2Hz
C1	0.22μF	Quality factorQ	1.823
C2	0.01μF	Attenuation when *f*=1kHz	-80dB

Fig. 4-9 shows the amplitude-frequency and phase-frequency characteristics of the low-pass filter. From Fig. 4-9, it is readily to find the cut-off frequency is approximately 10 Hz, which is in accordance with the calculation parameters in Table. 4-2. At the same time, the low-pass filter has reached an attenuation of -40 dB in the frequency of 100 Hz, which has a good average effect on a square wave with frequency of 1 kHz.

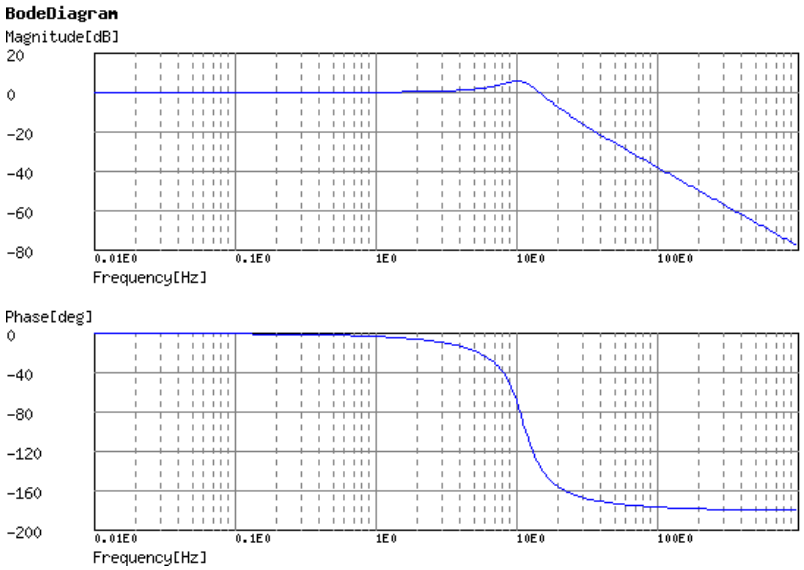

Fig. 4-9 Low-pass amplitude-frequency and phase-frequency characteristic characteristics

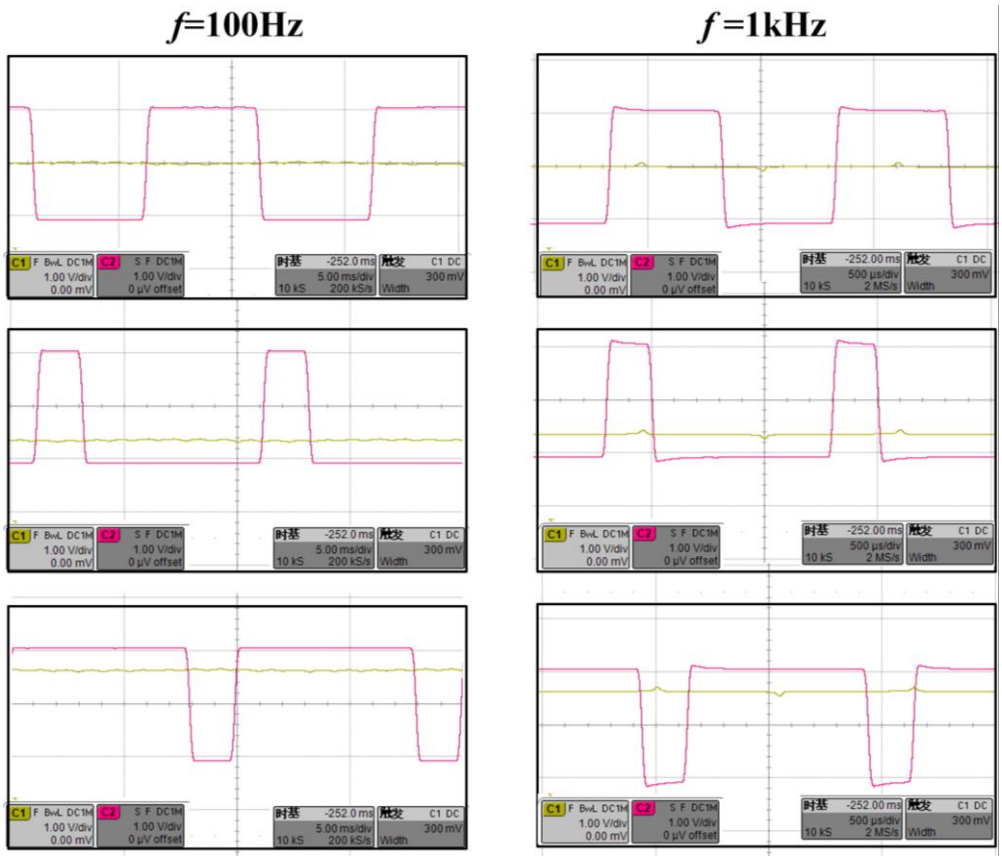

Fig. 4-10 Average circuit output waveforms at different frequencies

In order to cooperate with the voltage supply of the excitation circuit, the operational amplifier of the low-pass filter uses a high-voltage, high-speed op amp TL082. Its maximum supply voltage is ±18 V and the bandwidth gain product is 4 MHz. With a ±15 V supply, Fig. 4-10 shows the 100 Hz and 1 kHz square wave input and output waveforms of the filter at different duty cycles. Generated by GWINSTEK's AFG-2112 signal generator(featured by a 1% ~ 99% adjustable duty cycle for square waveform), the square wave signal passes through a low-pass filter and outputs a DC voltage. When the duty cycle is 50%, the output DC voltage is zero; when the duty cycle is greater than 50%, output is positive, and vice versa; the output voltage is consistent with the theoretical derivation in equation(3-5).

3) Reverse PI controller design

In order to eliminate the static difference error and increase the stability of the system, in the feed-back loop a tuned PI controller is added. The parameters of the PI controller is firstly tuned by Simulink. As shown in Fig. 4-11, considering the transfer function of the low-pass filter, the fluxgate is equivalent by a pure lagging component. By comparing the difference in the step response, the closed-loop PI is tuned.

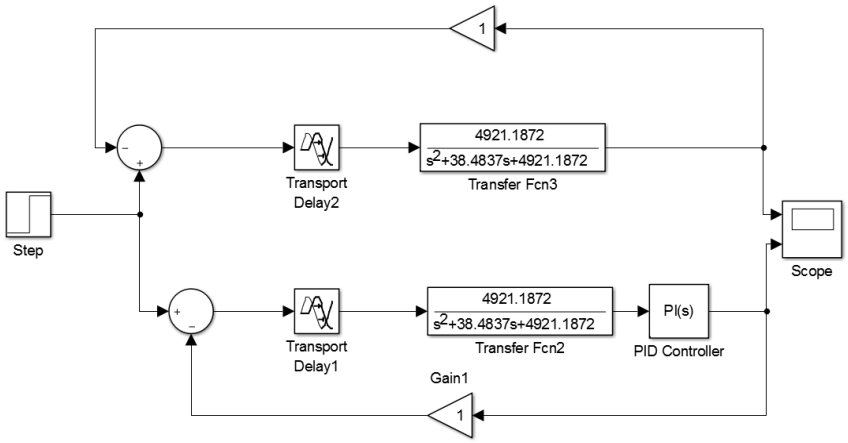

Fig. 4-11 PI parameters tuning block diagram

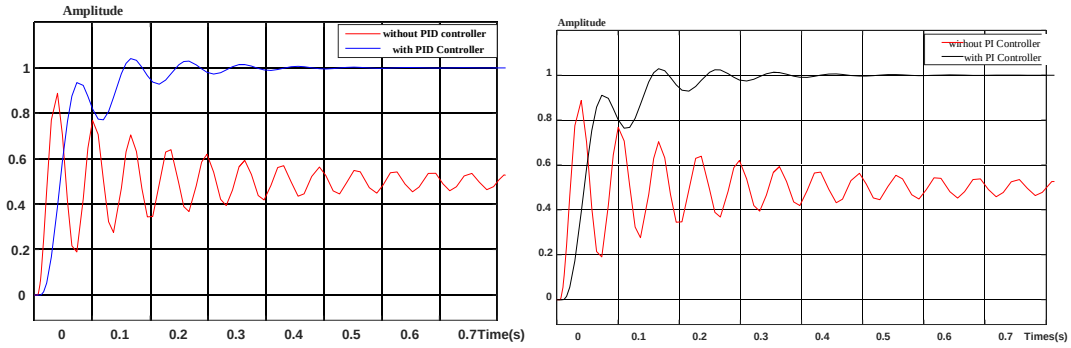

Fig. 4-12 (a) Step response of the simulation PI parameter.(b) Step response of the actual PI parameter

As shown in the red line in Fig. 4-12(a), without the PI controller, overshoot and oscillation occur. The abscissa is time (s), and the ordinate is the step response output, and it cannot always reach 1 at last, which means the input cannot be followed by the output eventually. Besides, overshoot and oscillation are severe. After the PI controller is added to the feedback loop, the system performance is optimized. The tuned PI parameters in simulation are as following: K_p=0.1450 and K_i=17.2802. The system step response after adding the PI controller with the tuned parameters in simulation is shown in blue line in Fig. 4-12(a). From the figure, it can be seen that both the overshoot and the oscillation have significantly improved compared to the original structure.

The circuit realization of the PI controller are shown in Fig. 4-13, where the parameters are determined as follows: $K_p=R_2/R_1$; $K_i=1/(R_1C_1)$. The resistance value of the resistor R_3 is much larger than R_1 and R_2 to prevent oscillation. According to the K_p and K_i values in the simulation to determine the size of each parameter, combined with the actual standard value of the actual capacitance and resistance, the final values are as follows: R_1 =300 kΩ，R_2=45 kΩ，R_3=10 MΩ，C_1=0.2 uF. According to the final actual value of the resistor and capacitor, recalculate K_p =0.15 and K_i =16.667. Reset the PI controller parameter in the simulink by the recalculated K_p and K_i. The step response is shown in Fig. 4-12(b). There was no significant deterioration in the overshoot and rise time compared with the simulated value, and the system was stable and no oscillation occurs.

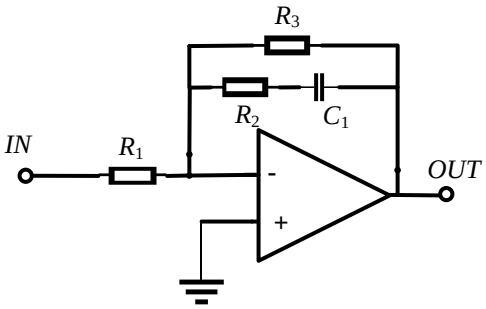

Fig. 4-13　Reverse PI controller circuit

4)　The overall circuit configuration

Construct the experimental circuit in Fig. 3-9(a), the detailed circuit are shown in Fig. 4-14. Since the operating principle has been discussed in detail in Section 3.2, here only list the circuit configuration and not repeat the principle. The voltage divider resistors R_1 and R_2 both takes 10 kΩ and the value of R_s is 50Ω/25Ω. Derivation from Chapter 3 shows that the accuracy of R_s directly affects the linearity factor of the measurement. The resistance accuracy of R_s is 0.1%, different from the other resistors which are all 5% metal diaphragm resistors. Meanwhile, in order to increase the capability for passing over-current, R_s is grouped by using multiple resistors in series and in parallel.

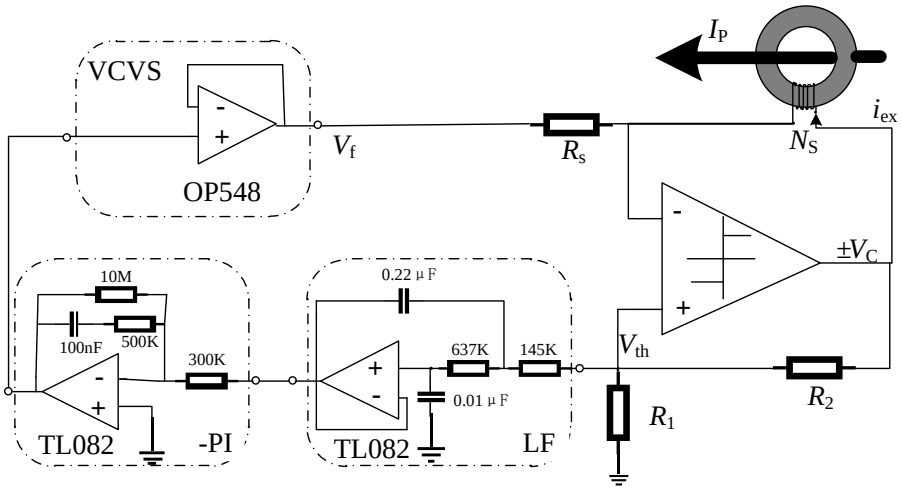

Fig. 4-14 Detailed experimental circuit diagram

In the actual circuit, the operational amplifiers of the low-pass filter and the PI controller all use TL082 as described above. In order to increase the amplitude of the excitation voltage, the comparator uses high voltage power operational amplifier OP548, which can support a supplying voltage of ±30 V and the output current can reach 3 A. Although the bandwidth gain product of the OP548 is only 1 MHz, it is enough for the design requirements. The greatest advantage of choosing this op amp is to meet the rapid comparison, and the op amp can directly provide the excitation current without additional driving stage. Even in the case of seriously biased magnetism, the 3-A output capability can still output the excited current, thereby the self-excited circuit is simpler and more robust compared with the traditional scheme. The power supply for the overall circuit is uniformed to ±15 V DC voltage source.

4.2.2 Experiment waveform verification

The measured current I_p is provided by MOTECH CNC 3A/30V programmable linear DC stabilized power supply. The power supply supports up to ±3A current output. By maintaining the same current and increasing the number of loops or turns of the coil, the strength of the magnetic field increases because each loop or turn of the coil sets up its own magnetic field. The magnetic field unites with the fields of the other loops to produce the field around the entire coil making the total magnetic field stronger. The ampere-turn (At) is the MKS (Metres, Kilograms, Seconds) unit of magnetomotive force (MMF), represented by a direct current of one ampere flowing in a single-turn loop in a vacuum.Using 10 turns for the measuring current winding produces an MMF of ±30 At. However, when a multi-turn winding is used for the measuring current, the transformer effect is remarkable. In order to suppress the transformer effect and prevent the influence of the stray magnetic field out of the iron core, the structure in Fig. 4-15 is adopted. Increasing the winding area and shielding the other wires so that the magnetic field sensored in the iron core is completely generated by the measuring side of the wires. It can help reduce the waveform asymmetry caused by the transformer effect.

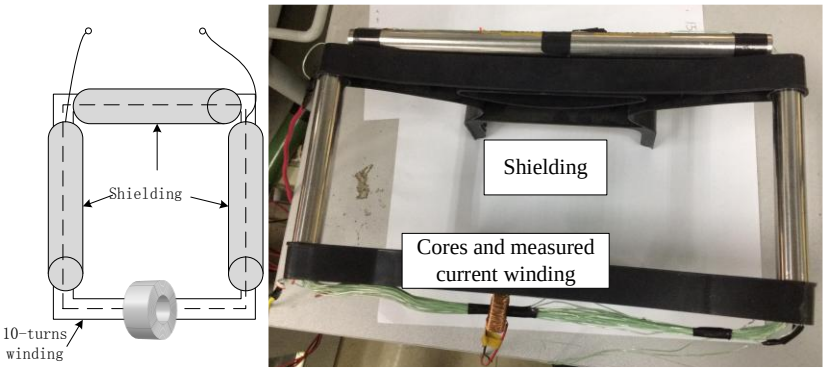

Fig. 4-15 Configuration of the measured current

The experimental circuit is shown in Fig. 4-16. The measuring current winds 10 turns as the configuration in Fig. 4-15. In order to ensure overcurrent capability of the tiny wire, the measuring current winding adopts 0.75-mm silver wire; the experimental circuit and the measuring current both use linear switching power supply. Waveforms were observed with TELEDYNE's HDO4054 four-channel oscilloscope.

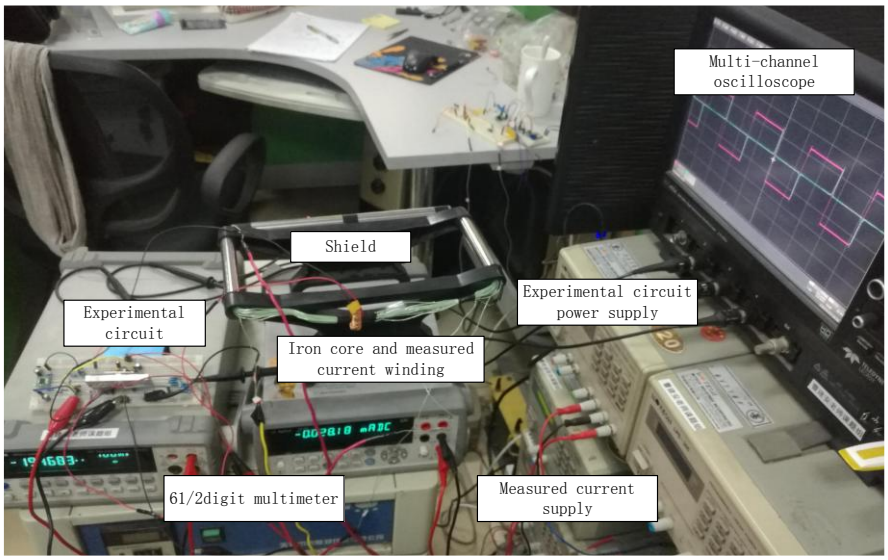

Fig. 4-16 Experimental diagram

As shown in Fig. 4-17, the oscilloscope waveforms for I_p= -5A and I_p= -10A for R_s=25 Ω, the yellow C1 channel is the voltage on R_s representing the excitation current, the red C2 channel is the switching threshold voltage V_{th}, and the green C4 channel represents the output voltage U_o. Analyzing the waveform, the following conclusion can be drawn:

(1) The shape of the current and voltage waveforms are consistent with the analysis in Fig. 3-10(b). The voltage is a square wave, the current is a sharp pulse with positive and negative symmetry. The current changes most slowly in the time interval t_2 and t_5 of the non-saturation period. It is readily seen that: $T_P=t_1+t_2+t_3\approx t_2$, $T_N=t_4+t_5+t_6\approx t_5$, which is consistent with the derivation in the third chapter, i.e. positive half-period T_P can be

approximately equal to t_2, negative half-cycle T_N can be approximately equal to t_5.

(2) The self-oscillating frequency is approximately 2 kHz, and after passing through the low-pass filter designed in the previous section, it becomes a stable DC level. It has validated the effectiveness of the low-pass filter. The observed ripple in the C4 channel is very small, the demodulation method is simple, effective and has high accuracy.

(3) Comparing the waveforms in Fig. 4-17, when the I_p changes, the current waveform can basically maintain positive and negative symmetry(The square wave signal remains basically unchanged at 50% duty cycle). The only change is the output DC level. When the I_p doubles, the amplitude of the DC level has also doubled, and the experimental circuit has achieved the expected feedback effect.

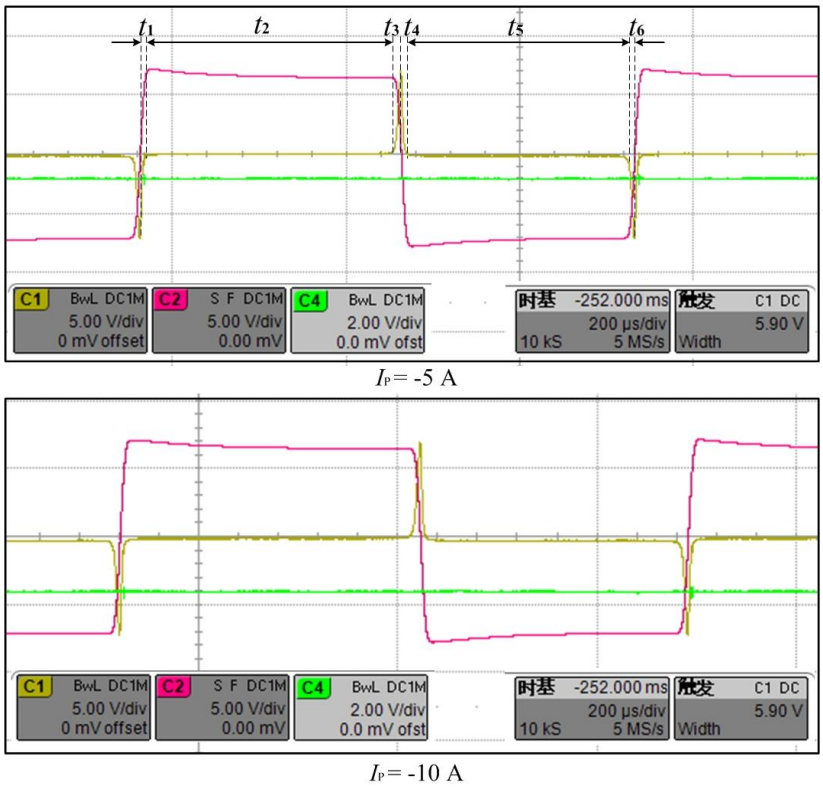

Fig. 4-17 Circuit measured waveform when R_s=25Ω

4.2.3 Main performance specifications

1) Sensitivity

Sensitivity for a typical transducer is the ratio between the small change in electrical output to a small change in physical input signal. In the case of R_s=25Ω and R_s=50Ω, the sensitivity evaluation experiments on the was carried out. The measuring current is supplied by a 3-A current source. To increase the measured current range, a winding of 10 turns is taken. That is, ten times of the output current is taken as the measured current I_p. The output voltage of the experiment is measured with the INSTEK GDM-8261 multimeter. The multimeter has a

6½ digits resolution and 0.0015% DC voltage accuracy. It satisfies the experimental accuracy requirements. In the experiment data recording, the effective number of decimal places is determined according to the multimeter's last stability bit during reading. in order to reduce the error caused by the manual reading as much as possible, each data takes the average of five readings. The measuring current changes within -30~30 A and the data records are shown in Table. 4-3 below.

Table. 4-3 Measured current I_p *vs* output U_o

Measured currentI_p(A)	Output U_o（R_s=25 Ω）	Output U_o（Rs=50 Ω）	I_p(A)	Output U_o（R_s=25 Ω）	Output U_o（Rs=50 Ω）
-30	-4.804	-8.697	0	-0.005	0.015
-28	-4.500	-8.098	0.5	0.070	0.135
-26	-4.146	-7.528	1	0.150	0.280
-24	-3.837	-6.970	1.5	0.231	0.408
-22	-3.529	-6.360	2	0.311	0.567
-20	-3.213	-5.825	3	0.472	0.854
-18	-2.897	-5.290	4	0.632	1.150
-16	-2.598	-4.655	5	0.807	1.450
-14	-2.290	-4.067	7	1.133	2.000
-12	-1.969	-3.485	9	1.452	2.610
-10	-1.647	-2.908	10	1.613	2.898
-9	-1.489	-2.630	12	1.940	3.486
-7	-1.167	-2.060	14	2.254	4.008
-5	-0.846	-1.440	16	2.560	4.650
-4	-0.685	-1.224	18	2.910	5.240
-3	-0.521	-0.922	20	3.223	5.793
-2	-0.357	-0.619	22	3.530	6.364
-1.5	-0.275	-0.453	24	3.835	6.932
-1	-0.193	-0.300	26	4.137	7.500
-0.5	-0.110	-0.165	28	4.460	8.047
0	-0.036	-0.079	30	4.782	8.587

The data in Table. 4-3 is fitted by least-squares method. The relationship between the actual measured output voltage and the measured current is shown in Fig. 4-18, in the range of ±30 A, the output exhibits a first-order linear relationship with the measured value; after the first-order fitting, the fitting function is obtained:

$$\begin{cases} U_o = 0.156 I_P - 0.012 & (R_s = 25\ \Omega) \\ U_o = 0.289 I_P - 0.019 & (R_s = 50\ \Omega) \end{cases} \tag{4-2}$$

The goodness of fit R^2 (statistical model describes how well it fits a set of observations) in the curves shown in Fig. 4-18 reaches 0.999 and 1 respectively, indicating that the straight line has a very good fit to the measured values. From equation (4-2), it can be found that when R_s is 25 Ω and 50 Ω, the actual sensitivity is 0.156 and 0.289, which is higher than the

0.125 and 0.25 calculated according to formula (3-36). This proves that the the necessity of correction for linear relationship derived in chapter 3. Take the experimental sensitivity S_1 = 0.156 and S_2 = 0.289 into equation (3-40). The current correction factor k = 0.536 and the winding resistance R_w = 2.466 can be obtained.

There is still a very small intercept at the 25 Ω and 50 Ω in the equation (4-2)(0.012 and 0.019, respectively). During the actual measurement experiment, we also found that when the measured current is zero, the output voltage is still a null-zero value. Actually, the cause is that the output level of the comparator is not completely symmetrical, i.e. the +15V and -15V amplitudes of the comparator output cannot be completely symmetric. This asymmetry due to the non-ideal characteristics of the device can be observed from both the experimental waveforms in Fig. 4-17 and the simulated waveforms in Fig. 3-14.

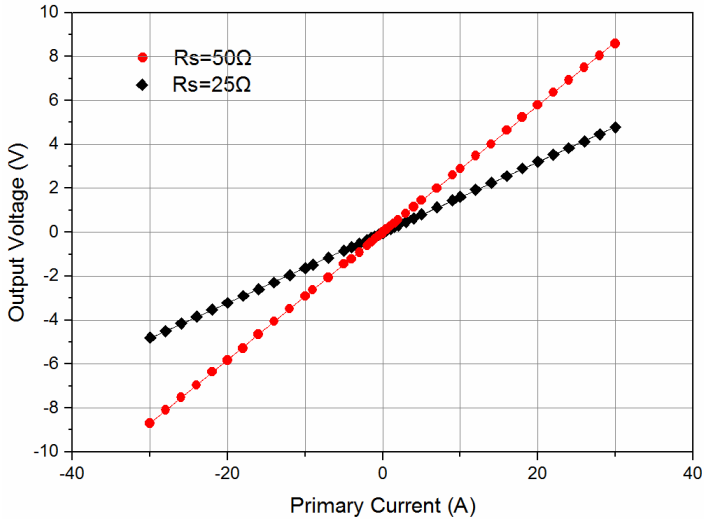

Fig. 4-18 the output voltage *Uo vs* measured current I_P

2) Linearity

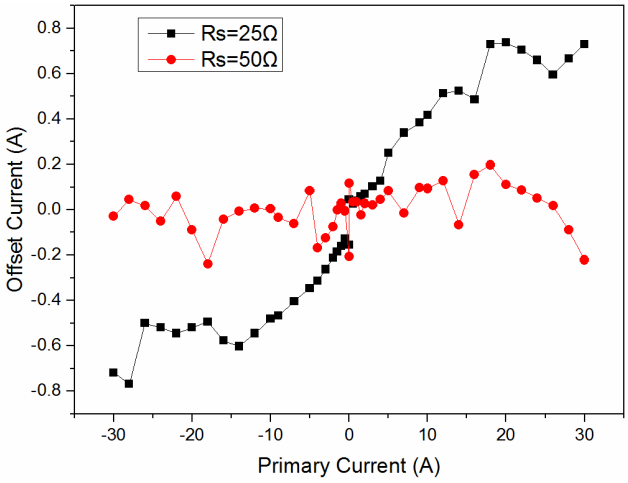

Fig. 4-19 Relative deviations of measured and fitted values when R_s=25 Ω and R_s=50 Ω

As shown in Fig. 4-19，the deviations of measured and fitted values is randomly distributed

in the range of -30A~30A. According to the linearity formula, the linearity at Rs=25Ω and Rs=50Ω can be obtained as 0.48% and 0.36%, respectively. The maximum value is less than five thousandths, indicating that the measurement result has a good linearity.. According to the linearity formula: $\varepsilon = \frac{|\Delta_{max}|}{y_{max}} \times 100\%$ when R_s=25 Ω and R_s=50 Ω, the linearity respectively : $\varepsilon_{25\Omega}$=0.48%, $\varepsilon_{50\Omega}$= 0.36%.

3) Measurement range and resolution

In the experimental circuit, the following core parameters: I_s ≈40mA, N_s =200， V_c ≈14 V are known, when R_s =50 Ω, the linear measurement range I_P～[-48 A， 48 A] can be obtained according to the equation (3-41). Likewise, when R_s =25 Ω, the linear measurement range is I_P～[-104 A，104 A]. To consider a safe margin, take the effective measurement range as 0.85 times the linear interval, that is, [-40.8A, 40.8A] for R_s =25 Ω and [-88.4A, 88.4A] for R_s =50 Ω. For R_s = 50Ω, polynomial fitting is also performed in the range of [-60A, 60A]. In Fig. 4-20, a sixth-order polynomial is used. The coefficients of high-order terms are small, and the first-order coefficients agree with the sensitivity S_1. At the same time, it also further validates the correctness of the linear fitting above.

In Fig. 4-20, the output characteristics of the experimental circuit with Rs = 25 Ω and Rs = 50 Ω is given, while the measuring current range is ±60 A. When the measuring current I_P is in the range of -40~40A, both curve show good linear relationships. When the measuring current amplitude exceeds 40A, the nonlinearity in the Rs = 50Ω circuit gradually increases, while the Rs = 25Ω circuit still remains in the linear region, which is consistent with the analysis, thus the sensor range can be estimated using (3-42).

Using INSTEK's 6½ digit multimeter GDM-8261 to measure the experimental output voltage, it was found that the voltage is stable at mV, i.e. the minimum effective change of the sensor output is ΔU=1 mV. According to the experimental data in the previous section, the sensitivity is 0.1598 V/A and 0.2894 V/A for R_s=25 Ω and R_s=50 Ω respectively, combined with the formula (4-9), we get the resolutions: $r_{25\Omega}$=6mA; $r_{50\Omega}$ =3 mA.

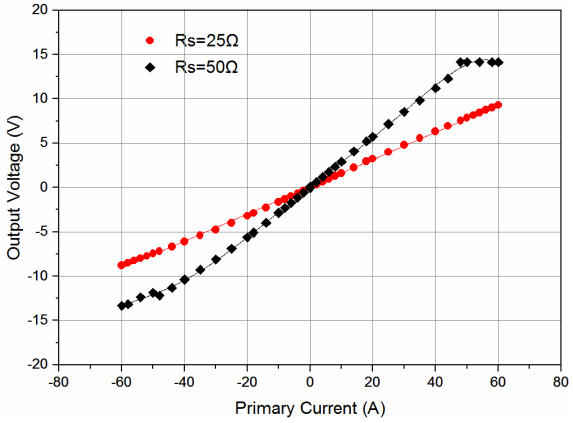

Fig. 4-20 Linear range experiment from -60~60A

4) Temperature characteristics and repeatability

The temperature rise effect of the large DC current is obvious. For the magnetic core, the magnetic permeability will change greatly with the change of temperature. This is also the reason why many open-loop fluxgate solutions have thermal drift. In this paper, the closed-loop scheme uses voltage compensation to maintain the self-excited oscillation duty cycle of 50%. In the measurement process, the influence of the temperature change caused by the core magnetic permeability on the measurement result is suppressed. The temperature characteristics test in this paper is just to verify the effectiveness of the closed-loop compensation scheme on temperature drift suppression. The temperature test is shown in Fig. 4-21, and the measuring system is placed in the incubator. The main deterioration is caused by high temperature. In this experiment, the temperature range of the thermostatic chamber is 25 ℃~65 ℃, and the temperature fluctuation is 0.5 ℃. During the experiment, the control temperature step is 10 ℃, and the sensor is tested in the range of 25 ℃~65 ℃.

The larger the resistance value, the greater the heating power, the higher the temperature rise, and the more severe the temperature drift. Therefore, under the same conditions, the temperature characteristic of R_s =50 Ω is worse than that of R_s =25 Ω. Based on testing the maximum deviation, Rs use the 50 Ω resistor. According to the measurement range analysis in section 3.2.3, the maximum measured current I_m is about 40 A when R_s=50 Ω, set I_p to ±100% I_m, ±50% I_m, ±25% I_m and zero respectively. The experimental results are shown inTable. 4-4. Similar to the data recorded above, each data point in the table is the average of 5 readings.

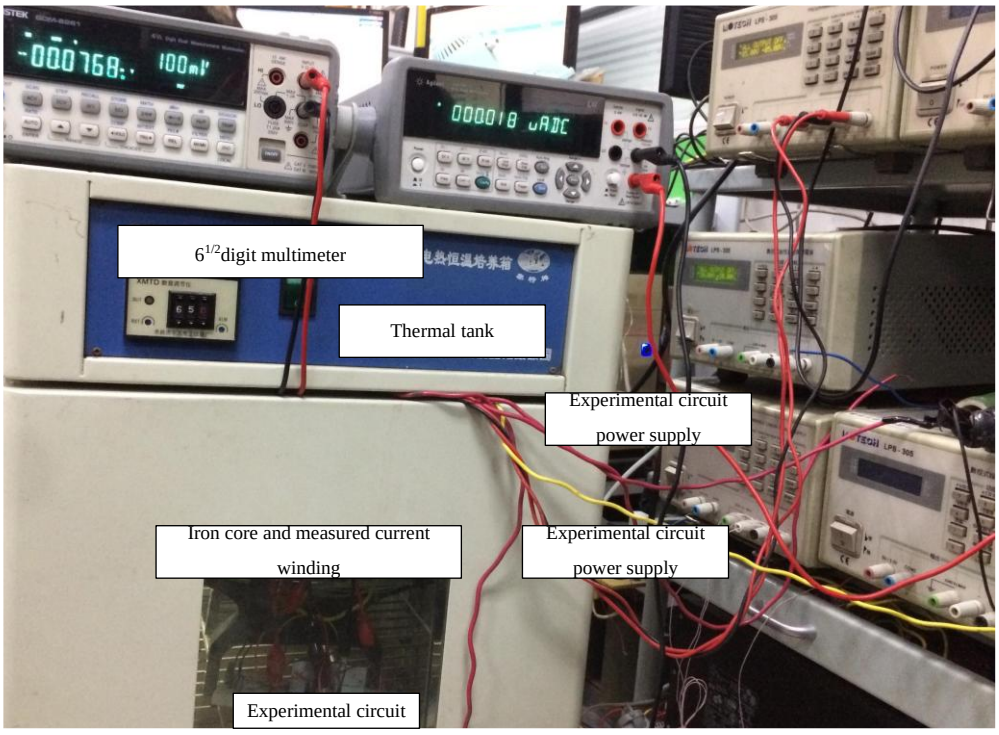

Fig. 4-21 Temperature experiment diagram

Table. 4-4 Temperature experimental data(R_s=50Ω)

I_P	U_o(V),T=25℃	U_o(V),T=35℃	U_o(V),T=45℃	U_o(V),T=55℃	U_o(V),T=65℃
100%I_m	11.194	11.082	11.200	11.190	11.204
50%I_m	5.638	5.589	5.631	5.686	5.672
25%I_m	2.847	2.799	2.798	2.828	2.824
0	-0.019	-0.018	-0.017	-0.017	-0.019
-25%I_m	-2.846	-2.830	-2.835	-2.876	-2.866
-50%I_m	-5.685	-5.590	-5.580	-5.650	-5.637
-100%I_m	-11.350	-11.390	-11.344	-11.352	-11.346

Note：I_m is the maximum measured current，when R_s=50 Ω，I_m=40 A

According to the data measured in Table. 4-4 and the relationship in (4-1), the measured values in the prototype are calculated at each temperature. Plot the results in Fig. 4.22, the data in Table. 4-4 is divided into four groups according to different measuring current values: ±100% I_m, ±50% I_m, ±25% I_m, and zero. It can be seen from the plot that when I_p= -50% I_m(-20A), the measured value changes the most with temperatures, the variation is about 368 mA in 40℃ , and the corresponding temperature drift is 9.2 mA/℃. Consider a full-scale range of approximately 80A at R_s=50Ω, so the temperature drift expressed in ppm/℃ is approximately 115 ppm/℃.

Analysis of the temperature-drift test results shows that the proposed solution does not exhibit significantly superior temperature characteristics compared to other open-loop solutions that rely on magnetic permeability. The main causes are not the foundational principle but are the following two aspects: Firstly, the performance of integrated electronic components affected by temperature; secondly, the temperature coefficient of discrete components. The integrated components are mainly comparators and operational amplifiers: the temperature change causes the comparator's switching time to change, and the comparator switches have different delays resulting in a zero input when the duty cycle deviates by 50%. Different temperature deviations are different. As the proposed method adopts closed-loop structure, the duty cycle is always compensated to 50% , so that even if the same input in different temperature has a different compensation value, i.e. the output value is different. In addition, the operational amplifiers used in the PI controller and LF will also result in reduced measurement accuracy due to the effect of temperature on the bias current and offset voltage. Discrete components are mainly resistance R_s and voltage divider resistors R_1, R_2: the output results in fact should be a compensation current value originally, it is converted into voltage through the resistor R_s, the changes of resistance R_s will cause a voltage variation; the changes of voltage divider resistors R_1, R_2 will cause the comparator flip voltage threshold changes whose effect is similar to the delay of the comparator switching time, which directly affects the duty cycle. Because the experimental circuit is in the constant temperature box, the temperature change will directly cause the resistance change. In the experiment, Risym metal diaphragm precision resistor with 0.1% accuracy is used. The resistance temperature drift is ±100 ppm/℃, so there is a certain level of thermal

drift. When the measuring current is zero, the effect of the circuit on the temperature drift can be reduced. As can be seen from Fig. 4, in the range of 25 ℃ to 65 ℃, the zero point deviation variation caused by the temperature change is up to about 8 mA. The corresponding zero thermal drift is about 0.2 mA/ ℃, which is about 2.5 ppm/ ℃ relative to the rated range of 80A. To a certain extent, the effectiveness of the suppression of thermal drift after the closed-loop compensation scheme is verified.

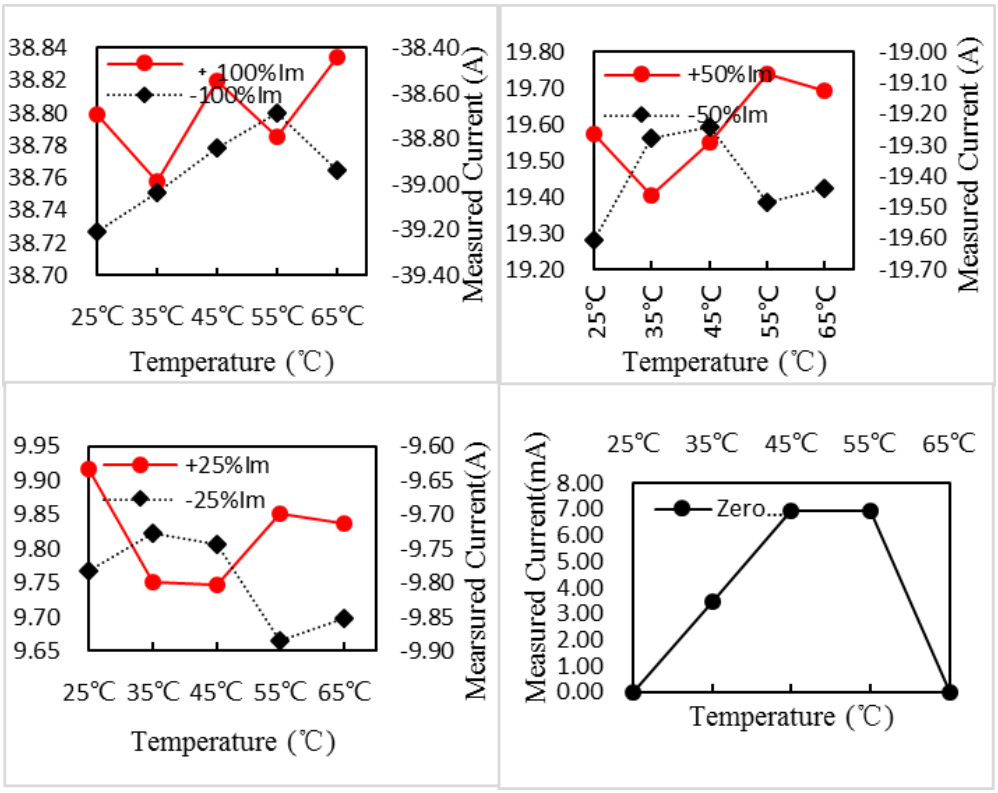

Fig. 4-22 Temperature experiment results of different measured current I_p

Reproducibility is the closeness of the agreement between the results of successive measurements of the same measurand carried out under the same conditions of measurement,i.e. the measurements are taken by a single person or instrument on the same item, under the same conditions, and in a short period of time. Due to the presence of hysteresis loops, the traditional open-loop fluxgate current sensors have some differences in the forward and reverse stroke. The following repetitive experiments are performed to verify that the closed loop can overcome the hysteresis loop's influence on the input and output characteristics. The test temperature is fixed at 25 ℃. Take R_s=50 Ω, and carry out multiple positive and negative stroke tests and record in the range of -30A to +30A. Record that the I_P changes monotonously from -30A to +30A as the positive stroke, from +30 A to -30 A as the reverse stroke. In Fig. 4-23, the results of two positive and negative strikes are plotted, on the one hand, the positive and negative strokes are basically identical, and there is no obvious hysteresis in the input and output transfer curves. This is because the closed-loop sensor in this paper essentially adopts the compensation principle so that self-oscillation always

maintains 50% duty cycle. The asymmetry caused by the measured current is offset by the compensation level. On the other hand, the positive stroke① and the positive stroke②are also very consistent, so the repeatability error is small.

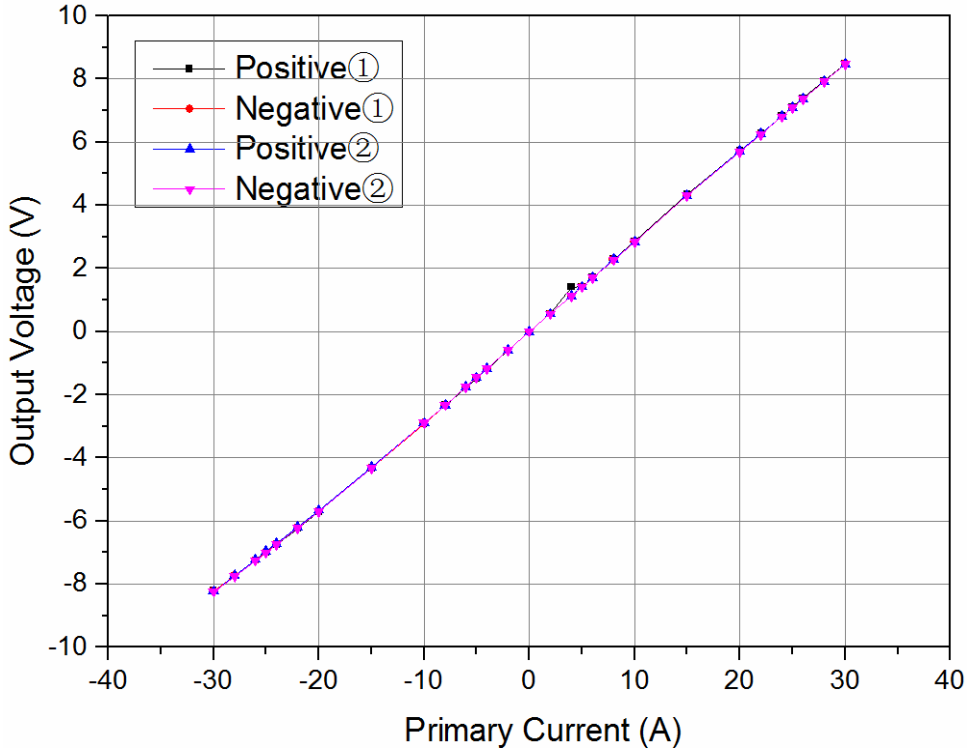

Fig. 4-23 Positive and negative stroke measurement results

In the repetitive experimental data, when the measured current is changed from -30 A to +30 A, the output voltage fluctuation is found to be the greatest when *I*p=20A. The measuring data when *I*p=20A is listed in Table. 4-5. The maximum measurement uncertainty is obtained from Table. 4-5 . According to Class A assessment of measurement uncertainty evaluation, *R*s=50Ω, according to the equation(4-2) we can get the linear relationship: $I_P = 3.460U_o + 0.066$. Firstly, use the Bessel formula to calculate the standard deviation of U_o :

$$S_R = \sqrt{\frac{\sum_{n=1}^{N}(U_o - u_o)^2}{N-1}} \tag{4-3}$$

Where N=12 and it stands for the independent measurement numbers;U_o represents the output of the n-th measurement; u_o is the average of the measured results. The measurement uncertainty is often taken as the standard deviation of a state-of-knowledge probability distribution over the possible values that could be attributed to a measured quantity. Relative uncertainty is the measurement uncertainty relative to the magnitude of a particular single choice for the value for the measured quantity, when this choice is nonzero.

Taking S_R as the uncertainty of U_o, according to the uncertainty transmission formula, the absolute value of the maximum relative percentage error of the instrument is calculated as: ε = 0.47%. According to China's industrial instrument accuracy grade, the accuracy level is 0.5

Table. 4-5 Repetitive experimental data when I_p=20A

Measured times n	ReadingsU_o(V)	Measured times n	ReadingsU_o(V)	Measured times n	ReadingsU_o(V)
1	5.746	5	5.754	9	5.743
2	5.745	6	5.752	10	5.745
3	5.751	7	5.752	11	5.744
4	5.754	8	5.753	12	5.743

The results show that the maximum uncertainty is no more than five thousandths, which also verifies that the closed-loop scheme can overcome the effect of hysteresis loop on the measurement transfer curve. This paper mainly validates that the closed-loop can overcome the hysteresis and keep consistency on the input and output curves, so it only estimates the maximum deviation on the repeatability index, but does not perform large sample repeatability experiments.

4.2.4 Comparison with existing similar measuring method

Using core magnetic saturation technology, the single-core single-winding measurement scheme used in this paper is compared with the existing single-core single-winding self-oscillating magnetic flux principle shown in Fig. 4-24.

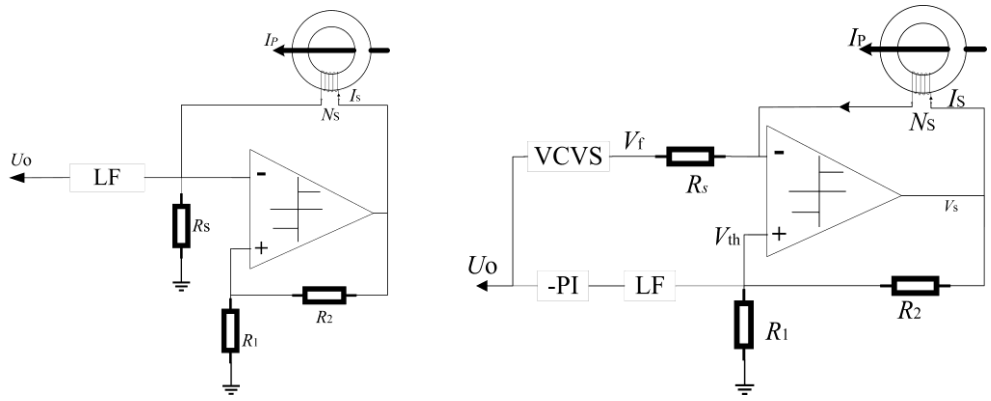

Fig. 4-24 (a)Single-core single-winding measurement of existing solutions. (b) the proposed solution

For the self-excited flux gate current measurement scheme by a single core single winding, the existing solutions can only achieve the open-loop average current model, as shown in Fig. 4-24(a), the measuring current causes the average value of the excitation current to change. As an open-loop system cannot correct any errors that it makes or correct for outside

disturbances, the linearity is poor, moreover, the hysterisis loop will also have a reflection in the input and output transfer characteristic. Closed-loop systems are designed to automatically achieve and maintain the desired output condition by comparing it with the actual condition, in our case, we use the feedback to keep the duty cycle always in 50%, the measuring current is treated as the disturbance introduced, thus it is proportional to the quantity of the feedback. The most prominent characteristic is that the closed-loop structure is realized under the extremely simplified circuit structure. By feedback, the proposed scheme has the advantages of large linear range, high linearity, good consistency, and low thermal drift. The comparison between the existing scheme and the proposed method is shown in Table. 4-6.

Apart from the difference in feedback, the linear characteristics used are also different. The existing scheme mostly are based on the relationship between the average value of the excitation current and the measuring current while the proposed scheme is based on the linearty of duty cycle and the measuring current. From the foregoing analysis, it can be known that the output waveform on the sampling resistor has a very high spike, the signal demodulation on the sampling resistor R_s is much complex than taking average of the square wave.As the complexity increase, it may also bring about instability; Compared to the excitation current, the excitation square wave voltage output amplitude is stable, and the oscillation frequency is basically fixed, the use of low-order low-pass analog filter can fulfill the demodulation, for example, a second-order low-pass filter used above has achieved a good result. In addition, if the input and output of the closed-loop feedback are both the voltage across the sampling resistor R_s, it will easily cause closed-loop oscillation. In this paper, the input of the feedback is from the comparison branch, the output is in the excitation branch, and a PI controller is added to eliminate the static difference and ensure the output is more stable.

Table. 4-6 Single core single winding measurement scheme comparison

Indicators	existing solutions	the proposed solution
Structure	Open-loop	Close-loop
Measurement model	The average	Duty cycle
The filter order	≥4	2
Linearity	1.2%	0.48%，0.32%
Anti-interference	weak	Strong
Maximum measured range	±250A	±40.8A，±88.4A
Zero-input thermal drift	＞100ppm/℃	2.5ppm/℃

4.3 Chapter summary

The content of this chapter is the experimental verification of Chapter 3. For the improved controllable valve reactor, this chapter validated the effectiveness through the prototype model experiment. For the large DC current detection scheme, this paper first introduced the design of the prototype and the experimental circuit in detail, and then verified the derivation and conjecture in the third chapter through experiments. Main performance indicators (linearity, sensitivity, range, resolution, temperature characteristics and repeatability) of the experimental circuit have been studied, and finally the advantages of the new scheme is presented by comparison with existing similar schemes.

5 Conclusions

In this paper, the magnetic saturation is studied. Based on the magnetic saturation characteristics, two practical problems in HVDC, namely the improvement of the valve reactor and the measurement of the large DC current, are proposed. After the detailed principle demonstration, the varification is performed both from the aspects of simulations and experiments. For the large DC current measurement, a prototype of the current sensor was developed based on the new scheme, and the measurement performance indicators such as sensitivity, linearity, and temperature characteristics were tested by experiments. The conclusion and future research topics are as follows:

5.1 Conclusion

（1）In this paper, we have reviewed the current research state of magnetic saturation research and studied several mathematical models commonly used to describe magnetic saturation and their cons and pros, combined with the engineering field application of converter valve reactors and DC high current measurements, the following conclusions are drawn: the Preisach model of hysteresis generalizes magnetic hysteresis as relationship between magnetic field and magnetization of a magnetic material as the parallel connection of independent relay hysterons, the model has become widely accepted as a general mathematical tool for the description of hysteresis phenomena of different kinds but it is unable to describe magnetic saturation phenomena and lack of physical meaning support; the Jiles-Atherton theoretical model is based on the principle of internal energy balance of ferromagnetic materials, and is characterized by the use of five physical parameters, the merits are stability, convenience, and has clear physical meaning. In the practical engeering application, in order to simplify the model, the hysteresis loop is generally treated as a piecewise linear curve.

（2） Based on Jiles-Atherton model, an improved scheme of valve reactor is proposed. A bias magnetic control winding is added on the basis of the existing valve reactor. The bias magnetic current I_b is used to control the saturation of the magnetic core. By reducing the magnetic flux density variation, the purpose is to suppress the vibration and noise caused by magnetostriction, to reduce the heat generation caused by iron loss, and to reduce the current saturation time of the reactor. The effectiveness of controllable magnetic saturation has been verified by Simulink simulation and prototype experiments.

（3）Based on modulation effect of the deep saturation, a novel closed-loop self-oscillation fluxgate large current detection scheme is proposed. By modifying the circuit structure of the self-excited fluxgate, we have realized the close-loop by a single winding on single core. The linear relationship of the closed-loop scheme is deduced in detail, then the working principle is thoroughly explained and varified by simulation, later the main measurement performance

indicators of the proposed sensor is tested. In the prototype, the design of the sensor core and the experimental circuit are given. The measurement performance indicators includes: linearity, sensitivity, measurment range, resolution, temperature characteristics, and repeatability. The test results show that the linearity reaches 0.48% and 0.36% when the R_s values are 50Ω and 25Ω, and the resolutions of 0.3mA and 0.6mA are achieved within the range of ±40A and ±90A. At the zero input. The temperature drift is about 2.5 ppm/℃ and the repeatability error is less than 5 ‰. Although performance is not superoir to the current products on the market, the compact single-core single-winding structure and simple demodulation method are unique, which can offer the guidance for reducing the volume for further miniaturization.

5.2 future research topics

The research in this paper basically achieves the intended purpose, but the following problems still need to be further studied:

（1） By the controlling winding of the valve reactors, the saturation can be controlled, thus to suppress the vibration and noise caused by magnetostriction and to reduce the over-heating. But when it comes to real HVDC converter with large current up to hundreds even thousands amperes, the source to provide the controlling bias current, i.e. the issue of energizing bias currents are to be discussed.

（2） For the newly proposed DC large current sensor, the prototype experimental current is less than 100A. Under the closed-loop scheme, the sensor power consumption increases with the increase of the measured current. When the current level needs to be increased, power consumption and heat dissipation need to be further studied.

（3） The dynamic characteristics of the proposed DC large current sensor scheme, such as the response rates, bandwidth, etc. are to be studied.

Reference

[1] Bakshi U A, Bakshi V U. Basic Electrical Engineering[M].*Basic electrical engineering*, McGraw-Hill, 2009:161-162.

[2] Chen Zhenhu, Liang Jiyong, Huang Xiangwei. Design and Application of Dynamic Reactive Power Compensation Device Based on Magnetic Reactor for Power System[J]. *Power System Technology*, 2005, 29(7): 82-84

[3] Chen Peng, Cao Junzheng, Wei Xiaoguang, et al. Transient Circuit Simulation Model of Saturable Reactor for HVDC Converter Valve[J]. *High Voltage Technology*, 2014, 40(1): 288-293.

[4] Zhang Jianguo, Fu Xingzhen. Design of Saturated Reactor for Thyristor Valves of HVDC Power Transmission[J]. *Journal of Xi'an Aeronautical Institute*, 2010, 28(3): 30-33.

[5] He Zhiyuan. Analysis of Controllable Magnetic Saturation Reactor[D]. Jinan: Shandong University, 2015.

[6] Fu Yang, Lan Zhida, Chen Yu. Transient Time Domain Simulation of Current Transformer[J]. *Power System Automation*, 1995(3): 25-31.

[7] Qi Weiguo. Electromagnetic dynamic process of current transformer and its simulation calculation [J]. Automation of Electric Power System, 1985(4): 27-42.

[8] XU Jing, WANG Haitao, HOU Denglu. Preisach Modeling of Polycrystalline Sr0.6Ca0.4RuO3 Magnetics[J]. *Rare Metals*, 2007, 31(6): 762-765.

[9] Shi Hong, Song Daojun, Liu Xi. Iron core magnetization model based on J-A theory and its improvement[J]. *Electrical Measurement & Instrumentation*, 2013(6): 4-7.

[10] Zhang Yanli, Wang Yangyang, Zhang Dianhai, et al. Vector Magnetostrictive Properties of Electrical Steel Sheets under Alternating Magnetization [J]. *Proceeding of the CSEE*, 2016, 36(4): 1156-1162.

[11] Gu Wenjuan, Pan Jing, Du Wei, et al. Magnetic anisotropy measured by ferromagnetic resonance method[J]. *Acta Phys. Sin.*, 2011, 60 (5): 702-707.

[12] Yang LiXia, Ge DeXi, Wang Gang, et al. Electromagnetic scattering recursive convolution-time-domain finite difference method for magnetized ferrite materials [J]. *Acta Phys. Sin*., 2007, 56(12): 6937-6944.

[13] Zhang Guanhan. Method for Measuring High-frequency Complex Magnetic Permeability of Soft Ferrite[J]. Magnetic Materials and Devices, 2000, 31 (3): 54-56.

[14] Liu Yuding, Liu Jihu. Resonance Measurement of Complex Permeability [J]. *Physical Testing*, 1989(3): 29-31.

[15] Chen Jiquan, Wang Rumei. Simulation of Dynamic Magnetization Characteristics[J]. *Transformer*, 2001, 38 (5): 6-8.

[16] Han Zandong, Li Xiaoyang. Measurement of magnetic permeability and electromagnetic loss of structural steels based on dynamic magnetization[J]. *Journal of Tsinghua University(Science Edition)*, 2014(11): 1471-1474.

[17] Gu Wei, Geng Jianxin. Study on the Principle of Single-Width Flux Gate Based on Piecewise Linearity of Permeability [J]. *Chinese Journal of Scientific Instrument*, 2001, 22(z1): 9-10.

[18] Yan Huiping. Research on magnetic field demagnetization theory [D]. Xi'an: Xi'an University of Architecture and Technology, 2008.

[19] Sazonov SV, Trifonov EV. On a (3+1)-dimensional solution of the Landau-Lifshitz equation[J]. *Russian Physics Journal*, 1994, 37 (6): 571-573.

[20] Song Hongzhang, Zeng Huarong, Li Guorong, et al. Observation Methods of Magnetic Domains[J]. *Materials Review*, 2010, 24 (17): 106-111.

[21] Huang Li, Yang Weixing, Zhang Xuesong. Modeling and simulation of air-gap current transformer based on PSCAD/EMTDC[J]. *Power System Protection and Control*, 2010, 38(18): 178-182.

[22] Xie Yu. Hysteresis Nonlinear Modeling and Experimental Research of Capacitance Load Cells[J]. *Electric Measurement & Instrumentation*, 2011, 48(10): 69-72.

[23] Mou Xianmin, Wang Jianyu, Ji Yanchao, et al. Current status and development of controllable reactors [J]. *Electrical Applications*, 2006, 25(4): 1-4.

[24] Ding Dongdong. Numerical calculation and performance study of leakage inductance of magnetron saturable reactor[D]. Harbin: Harbin University of Science and Technology, 2011.

[25] Ge Liang, Xing Peng, Ma Yu, et al. Research on Insulation Resistance Test of DC Transmission Valve Reactor [J]. *Power Capacitor and Reactive Power Compensation*, 2014, 35(6): 62-67.

[26] Tian Xingwang, Tang Xiaoling, Lu Jiasheng. Application of Infrared Diagnosis in Fault Analysis of Valve Reactor Heat Dissipation in HVDC Transmission System [J]. *High Voltage Apparatus*, 2008, 44(5): 469-471.

[27] Yang Zhenyu, Yu Chengyi. Failure Analysis of Valve Cooling System in UHVDC Converter Station[J]. *East China Electric Power*, 2010, 38 (3): 369-372.

[28] Yan Xiaoqin. Causes of transformer noise and measures to reduce noise [J]. *East China Electric Power*, 2012(4): 687-688.

[29] Moses AJ, Anderson PI, Somkun S. Modeling 2-D Magnetostriction in Nonoriented Electrical Steels Using a Simple Magnetic Domain Model[J]. *IEEE Transactions on Magnetics*, 2015, 51 (5): 1-7.

[30] Somkun S, Moses AJ, Anderson PI. Measurement and Modeling of 2-D Magnetostriction of Nonoriented Electrical Steel[J]. *IEEE Transactions on Magnetics*, 2012, 48(2): 711-714.

[31] Zhou Bing, Song Qian, Ni Yuan, et al. Noise Characteristics and Control of High Voltage Shunt Reactor [J]. *High Voltage Technology*, 2016, 42(6): 1819-1826.

[32] Kitagawa W, Ishihara Y, Todaka T, et al. Analysis of Structural Deformation and Vibration of a Transformer Core by Using Magnetic Property of Magnetostriction[J]. *Electrical Engineering in Japan*, 2010, 172(1): 19-26.

[33] Li Fang. Design and research of fluxgate magnetometer [D]. Changchun: Jilin University, 2014.

[34] Wang J. Sensor principle and detection technology [M]. Changchun: Jilin University Press, 2003.

[35] Li Jifan. Precision Electrical Measurement [M]. Beijing: China Measurement Press, 1984.

[36] Ripka P. Electric current sensors: a review[J]. *Measurement Science & Technology*, 2010, 21 (11): 112001.
[37] Ziegler S, Woodward RC, Iu HC, et al. Current Sensing Techniques: A Review[J]. IEEE Sensors Journal, 2009, 9(4): 354-376.
[38] Zhang Zhenggang. Research on DC High Current Measurement Technology [D]. Beijing: North China Electric Power University, 2014.
[39] Filanovsky IM, Piskarev VA. Sensing and measurement of DC current using a transformer and RL -multivibrator[J]. *IEEE Transactions on Circuits & Systems*, 1991, 38 (11): 1366-1370.
[40] Filanovsky IM, Piskarev VA. Circuit with nonlinear transformer provides isolation for DC measurements[J]. *IEEE Circuits & Devices Magazine*, 1991, 7(5): 36.
[41] Filanovsky IM, Taylor L. Circuit with nonlinear transformer allowing DC current measurements via an isolation gap[C], 1992(311): 318-323.
[42] Pejovic P. A simple circuit for direct current measurement using a transformer[J]. *IEEE Transactions on Circuits & Systems I Fundamental Theory & Applications*, 2002, 45(8): 830-837.
[43] Ripka P, Draxler K, Styblikova R. AC/DC Current Transformer With Single Winding[J]. *IEEE Transactions on Magnetics*, 2014, 50(4): 1-4.
[44] Velasco-Quesada G, Roman-Lumbreras M, Conesa-Roca A, et al. Design of a Low-Consumption Fluxgate Transducer for High-Current Measurement Applications[J]. *IEEE Sensors Journal*, 2011, 11(2): 280-287.
[45] Yang X, Li Y, Guo W, et al. A New Compact Fluxgate Current Sensor for AC and DC Application[J]. *Magnetics IEEE Transactions on*, 2014, 50(11): 1-4.
[46] Yang X, Guo W, Li C, et al. Design Optimization of a Fluxgate Current Sensor With Low Interference[J]. *IEEE Transactions on Applied Superconductivity*, 2016, 26(4): 1-5.
[47] Yang X, Yang X, Guo W, et al. A fluxgate current sensor with a U-shaped magnetic gathering shell[J]. *IEEE Transactions on Magnetics*, 2015, 51(11): 1-4.
[48] Wang Lu, Li Kui, Ren Bofei, et al. Magnetic-AC Modulation AC and DC Leakage Current Detection Method Based on All-phase Fourier Transform[J]. *Acta Power Technology*, 2015, 30(18): 254-260.
[49] Wang N, Zhang Z, Li Z, et al. Design and Characterization of a Low-Cost Self-Oscillating Fluxgate Transducer for Precision Measurement of High-Current[J]. *IEEE Sensors Journal*, 2016, 16(9): 2971-2981.
[50] Wang Nong. Research on self-oscillating fluxgate method for accurate measurement of large DC current[D]. Harbin: Harbin Institute of Technology, 2016.
[51] Li Fuhua, Liu Dezhi, Chen Junquan, et al. Preisach Hysteresis Model Identification and Verification Based on Lorentzian Function[J]. *Transactions of China Electrotechnical Society*, 2011, 26(2): 1-7.
[52] Bernard Y, Mendes E, Bouillault F. Dynamic hysteresis modeling based on Preisach model[J]. *IEEE Transactions on Magnetics*, 2002, 38(2): 885-888.
[53] Liu Shuo. Research on material model problem in magnetic field numerical calculation [D]. Tianjin: Hebei University of Technology, 2000.
[54] Mayergoyz ID. Vector Preisach Models of Hysteresis - Mathematical Models of Hysteresis and Their Applications[J]. *Mathematical Models of Hysteresis & Their Applications*, 2003: 149–223.
[55] Garikepati P, Chang T T, Jiles D C. Theory of ferromagnetic hysteresis: evaluation of stress from hysteresis curves[J]. *IEEE Transactions on Magnetics*, 1988, 24(6): 2922-2924.
[56] Jiles DC, Thoelke JB. Theory of ferromagnetic hysteresis: determination of model parameters from

experimental hysteresis loops[J]. *Magnetics IEEE Transactions on Magnetics*, 1989, 25(5): 3928-3930.

[57] Jiles DC, Thoelke JB, Devine MK. Numerical determination of hysteresis parameters for the modeling of magnetic properties using the theory of ferromagnetic hysteresis[J]. *IEEE Transactions on Magnetics*, 1992, 28 (1): 27-35.

[58] Zhang Yanli, Peng Zhihua, Xie Dexin, et al. Influence of Different Magnetization Curves on Transformer Core Loss Simulation under DC Bias Magnetism[J]. *Transactions of China Electrotechnical Society*, 2014, 29(5): 43-48.

[59] Ponjavic MM, Duric RM. Nonlinear Modeling of the Self-Oscillating Fluxgate Current Sensor[J]. *IEEE Sensors Journal*, 2007, 7(11): 1546-1553.

[60] Ji Feng, Chen Peng, Wei Xiaoguang, et al. Modeling and Simulation of Saturated Reactor for HVDC Converter Valve[J]. *Smart Grid*, 2013, 1 (2): 65-69.

[61] Yang X, Zhang B, Wang Y, et al. The optimization of dual-core closed-loop fluxgate technology in precision current sensor[J]. *Journal of Applied Physics*, 2012, 111(7): 1303.